HydroSoil

Ground based SAR experiment for soil moisture measurements

ESA Contract No. 4000132509/20/NL/FF/ab

Final Report

November, 2021

Abstract

This document contains a full description of the HydroSoil Campaign, based on Ground Based Synthetic Aperture Radar continuous monitoring experiments on a controlled agricultural field with focus on soil moisture and water cycle observations.

The report describes the campaign objectives, instrumentation used, complementary ancillary data, the programme of work and related activities. The main results achieved to date are presented and interpreted, including the analysis tools and algorithms that have been used.

Contents

1 DOCUMENT REVISION LIST

Revision history and approval record

Revision	Date	Purpose
0	23/6/2021	Document creation
1	29/7/2021	Document revision
2	14/10/2021	Final revision
3	25/11/2021	Final revision including Barley Phase results

Written by:		Reviewed and approved by:	
Date		Date	
Name	Albert Aguasca Solé Jordi Biscamps Dalmau Xavier Fàbregas Cànovas Jordi Llop Casamada Jordi J. Mallorquí Franquet Mireia Mas Hector Palacio	Name	Antoni Broquetas Ibars Emilio Gil Moya
Position	Project Author	Position	Project Supervisor
Signature		Signature	

2 APPLICABLE DOCUMENTS

[SoW] Statement of Work. HYDROSOIL – Ground based SAR experiment for soil moisture measurements. ESA Doc. Ref: ESA-EOPSM-CAMP-SOW-3719. 29 pages. Issued on 04/05/2020.

[CIP] HydroSoil. Campaign Implementation Plan - Ground based SAR experiment for soil moisture measurements.

[D2a] HydroSoil. Preliminary Data Acquisition Report (Barley Campaign D2a). Feb. 2021

[D2b] HydroSoil. Preliminary Data Acquisition Report of Corn Campaign (D2b). March 2021

[TN] HydroSoil. Technical Note. May 2021

3 REFERENCES

[1] "G-CLASS:H20". Hobbs S. Et al. G-CLAA:H20-Geosynchronous- Continental Land-Atmosphere Sensing System. EE10 Mission Proposal, ESA Ref: CE10/008.

[2] ECC/DEC/(04)08. ECC Decision of 09 July 2004 on the harmonised use of the 5 GHz frequency bands for the implementation of Wireless Access Systems including Radio Local Area Networks (WAS/RLANs)

[3] J. van Zyl, Y. Kim, "Synthetic Aperture Radar Polarimetry", Jet Propulsion Laboratory, December 2010. Available on line from: https://descanso.jpl.nasa.gov/SciTechBook/st_series2_chapter.html#. Accessed on 5 May 2021.

[4] K. Sarabandi, F.T. Ulaby, M.A. Tassouji, "Calibration of Polarimetric Radar System with Good Polarization Isolation," Transactions on Geoscience and Remote Sensing, Vol. 28, No. 1, January 1990.

[5] The radio refractive index: its formula and refractivity data, Recommendation ITU-R P.453-14 (08/2019), P Series Radiowave propagation, International Telecomunication Union. Available at https://www.itu.int/dms_pubrec/itu-r/rec/p/R-REC-P.453-14-201908-I!!PDF-E.pdf . Accessed on January 2021.

[6] Dept. Primary Industries and Regional Development, Agriculture and Food, Government of Western Australia. "Zadoks Growth Scale". Available at:

https://www.agric.wa.gov.au/grains/zadoks-growth-scale. Accessed on June 2021.

[7] P. Bongard, E. Oelke, S. Simmons, "Spring barley growth and development guide", available at

https://extension.umn.edu/growing-small-grains/spring-barley-growth-and-development-guide#sources-792910. Accessed on June 2021.

[8] N.E.C. Verhoest, et al. "On the Soil Roughness Parameterization Problem in Soil Moisture Retrieval of Bare Surfaces from Synthetic Aperture Radar". Sensors 2008, 8(7), 4213-4248; https: //doi.org/10.3390/s8074213

[9] Davidson, M.W.J. et al (2000). On the Characterization of Agricultural Soil Roughness for Radar Remote Sensing Studies. IEEE Transactions on Geoscience. Remote Sens. 2000, 38, 630 – 640 https://doi.org/10.1109/36.841993

[10] F. De Zan, A. Parizzi, P. Prats-Iraola, P. López-Dekker, "A SAR Interferometric Model for Soil Moisture", IEEE Transactions on Geoscience and Remote Sensing, vol. 52, no. 1, pp. 418-425, 2014

[11] Ulaby, F. and Long, D. G. (2014). Chapter 10: Surface-Scattering Models and Land Observations. In *Microwave Radar and Radiometric Remote Sensing*, pages 422-428. The University of Michigan Press., ISBN 978-0-472-11935-6.

[12] G.S.Campbell, "Calibration and evaluation of the low-cost EC-5 soil moisture sensor", available at: https://www.metergroup.com/environment/articles/calibration-evaluation-ec-5-soil-moisture-sensor/. Accessed on June 2021.

[13] A. Chanzy, J.C. Gaudu, O. Marloie, Correcting the Temperature Influence on Soil Capacitance Sensors Using Diurnal Temperature and Water Content Cycles. Sensors 2012, 12(7), 9773-9790; https://doi.org/10.3390/s120709773

[14] Mehdi Hosseini et al. "Soil Moisture and Vegetation Measurement Guideline". Joint experiment for Crop Assessment and monitoring (JECAM), March 22, 2018.http://jecam.org/wp-content/uploads/2018/07/Ground_Measurement_Guideline_AAFC_2018.pdf

[15] D. Or, J M. Wraith, Temperature effects on soil bulk dielectric permittivity measured by time domain reflectometry: A physical model. WATER RESOURCES RESEARCH, VOL. 35, NO. 2, PAGES 371-383, February 1999. https://doi.org/10.1029/1998WR900008

[16] Stevens Water, "Hydraprobe Reliable Soil Insigh", Available at: https://stevenswater.com/resources/datasheets/HydraProbe%202020_draft3.pdf. Accessed on June 2021.

[17] W. Skierucha. Time Domain Reflectometry: Temperature-dependent Measurements of Soil Dielectric Permittivity, Electromagnetic Waves, Vitaliy Zhurbenko. June 21st 2011. IntechOpen, DOI: 10.5772/17162

[18] M. S. Seyfried, L. E. Grant, Temperature Effects on Soil Dielectric Properties Measured at 50 MHz. Vadose Zone Journal. Available at : https://www.stevenswater.com/resources/documentation/hydraprobe/Seyfried3.pdf , accessed on June 2021.

[19] NIH, "ImageJ" application, available at: https://imagej.nih.gov/ij/index.html. Accessed on June 2021.

[20] R. Iglesias, X. Fabregas, A. Aguasca, JJ. Mallorquí, et al., "Atmospheric phase screen compensation in ground-based SAR with a multiple-regression model over mountainous regions" Transactions on Geoscience and Remote Sensing, Vol. 52, No. 5, pp. 2436-2449, May 2014.

[21] Ulaby, F. and Long, D. G. (2014). Chapter 11-11: Effects of Dew, Wind and Other Environmental Factors. In *Microwave Radar and Radiometric Remote Sensing*, pages 507-508. The University of Michigan Press., ISBN 978-0-472-11935-6.

[22] Juan M. Lopez-Sanchez, Shane R. Cloude, J. David Ballester-Berman, "Rice Phenology Monitoring by Means of SAR Polarimetry at X-Band" Transactions on Geoscience and Remote Sensing, Vol. 50, No. 7, pp. 2695-2709, July 2012.

[23] Alexander W. Jacob, et al., "Sentinel-1 InSAR Coherence for Land Cover Mapping: A Comparison of Multiple Feature-Based Classifiers" IEEE Journal of Selected Topics in Applied Earth Observations and Remote Sensing, Vol. 13, pp. 535-552, 2020

[24] Alejandro Mestre-Quereda, et al., "Time-Series of Sentinel-1 Interferometric Coherence and Backscatter for Crop-Type Mapping " IEEE Journal of Selected Topics in Applied Earth Observations and Remote Sensing, Vol. 13, pp. 4070-4083, 2020.

[25] Ritchie, S.W., J.J. Hanway, G.O. Benson, and J.C. Herman. 1993. "How a corn plant develops", Special Report . No. 48, Iowa State University.

[26] Riedel, T., Pathe, C., Thiel, C., Herold, M., and Schmullius, C. (2001): Systematic investigations on the effect of dew and interception on multifrequency and multipolarimetric radar backscatter signals. Proceedings Third International Symposium on Retrieval of Bio- and Geophysical Parameters from SAR Data for Land Applications published by ESA, 11 – 14 September 2001, Sheffield, UK, pp. 99 – 104.

[27] C. Schmullius, T. Riedel, "TerraDew Research Project – Overview" (2004). Available at http://www.terradew.uni-jena.de/sites/overview.html. Last accessed on 20 May 2021.

[28] J.D. Ballester-Berman, "Reviewing the role of the extinction coefficient in radar remote sensing", 2020. arXiv.org/physics/arXiv:2012.02609v1. Available at

https://arxiv.org/abs/2012.02609v1. Accessed on 20th May 2021.

4 GENERAL CAMPAIGN DESCRIPTION

HYDROTERRA, proposed as G-CLASS [1 (or Geosynchronous – Continental Land-Atmosphere Sensing System), is an exciting mission concept which offers a remarkable range of capabilities and which could have a significant impact on the sciences of weather forecasting, hydrology, and the mountain cryosphere, as well as providing direct benefits to society. The mission focuses on observing and understanding rapid processes of the water cycle over land. Science drivers call for persistent observations of the water cycle, which require using geosynchronous orbits (GEO) and microwave sensors.

The primary science focus is on the diurnal water cycle: the atmosphere, integrated water vapour that affects the refractive index, and surface, the backscatter phase and amplitude. The overall mission takes advantage of established measurement techniques, like soil moisture from backscatter, atmospheric phase delay, wet/dry snow contrast, but with a dramatically improved temporal sampling. The higher temporal sampling of the data has allowed to measure rates of change and separate processes like intercepted precipitation, evaporation, soil drying and plant moisture content. Interferometric SAR phase changes can also be used to estimate soil and vegetation phase centres and how they evolve along the day and under the environmental conditions.

Among the different societal benefits of HYDROTERRA, the water resource management and agriculture monitoring are probably the ones that can have a greater impact. In the mission analysis, it is necessary to do preliminary studies and validation campaigns in controlled scenarios. These studies, using ad-hoc radar systems, will allow to validate the potentialities of the mission for agricultural monitoring, evaluate the decorrelation effects of the long integration times over agricultural fields, monitor the effects of the plant growth and irrigation on the images and evaluate the potentialities of polarimetry in HYDROTERRA. A key point is obviously the test agricultural field in which the key parameters, including weather information, soil moisture and plant characteristics are perfectly recorded with the required temporal sampling.

The main objective of the HYDROSOIL project is to demonstrate the retrieval of soil moisture and vegetation parameters in an agricultural field under controlled conditions using a ground based fully-polarimetric SAR instrument (GB-PolSAR). The instrument simulates the frequent acquisitions of the HYDROTERRA mission. The data will be used to investigate HYDROTERRA's capability to retrieve soil moisture and to measure vegetation parameters. The campaigns have used a GB-PolSAR instrument, designed and built by members of UPC's CommSensLab Research Centre. The incidence angles have been similar to those of geosynchronous satellite observations over Europe.

Two measurement campaigns, barley from March 2020 to June 2020 and corn from July 2020 to November 2020 have been carried out. Despite the constraints and limitations imposed by the COVID-19 pandemic, a continuous monitoring of an agricultural field with a temporal resolution of 10 minutes and a spatial resolution in the order of a square meter have been completed. This operation has resulted into a huge data set of more than 31,000 polarimetric acquisitions with 150 GByte of raw radar data which are complemented with additional ancillary data. The campaigns have provided calibrated dual-pol (for barley) and quad-pol (for corn) Single Look Complex (SLC) images with a large number of resolution cells.

In the first campaign season in spring 2020, barley, a typical cereal cultivated in southern Europe, has been sown and monitored until the beginning of summer. Immediately after barley harvest, the

field has been ploughed and corn has been sown. Due to the water requirements of corn, an irrigation system has been deployed. The corn crop has been monitored through its life cycle until harvesting in November 2020.

The assessment has required intensive procurement of ground truth ancillary data, encompassing continuous acquisition of relevant meteorological parameters like air humidity, temperature, precipitation wind speed and direction, pressure and solar irradiation. Soil roughness has been characterised after crop sowing. Several calibrated soil moisture sensors have been installed at different depths at different field locations to provide continuous monitoring of soil moisture. Frequent vegetation sampling and processing have also been performed, to obtain data on plant density, size, row direction, leaf area index (LAI), height and orientation of main elements, water cycle and water content.

Special operation modes of the radar have been used in order to satisfy complementary objectives such as determining the Doppler spectrum of agricultural scenes induced by wind or assessing the defocusing due to phase decorrelation using the long synthetic aperture integration times foreseen for HYDROTERRA (from several minutes to hours).

The different densities, sizes and water content of both crops and all data generated will allow to assess HYDROTERRA's and other future missions' capabilities to provide soil moisture and crop water content data.

This Final Report includes, in section 5, the detailed description of the whole experiment, including the experimental field, the radar and the different instruments used in the two campaigns, together with the data processing and calibration techniques.

The following sections, 6 and 7, include the description of the data acquisition procedures for the barley and corn crop campaigns. The measured backscattering magnitude changes for barley and corn crops are presented including a preliminary analysis of results. Detailed subsections analyse and discuss the impacts of rain, soil moisture, diurnal cycles attributed to dew and a study on possible radar sensing of diurnal water content dynamics. In addition, the HH-VV decorrelation dependence on surface parameters is analysed. A study on interferometric phase and coherence of both barley and corn crops is presented. The coherence evolution with time has been studied with detail in multiple time scales and compared with crops height, environmental conditions and field operations. A slow aperture assessment, useful for Geosynchronous SAR (GEOSAR) missions validation such as Hydroterra, is shown. A preliminary Doppler Spectral Density study has been carried out on corn for different values of average wind speed.

Section 8 is a detailed assessment of the proposed short-term calibration methodology and the achieved results considering the intrinsic stabilities of the radar system and the deployed trihedral and dihedral reflectors.

Section 9 includes a description of the data repository. Finally, the main conclusions of this study are presented in section 10.

5 HYDROSOIL SITE

5.1 FIELD DESCRIPTION

The test site is the experimental agricultural field of the Barcelona School of Agri-Food and Biosystems Engineering EEABB, UPC, 41° 16' 36'' N - 1° 59' 11'' E. The field is in front of the North North-West facade of the EEABB building (Figure 5.1). The cultivated area is 25 m far from the

façade, its depth is approx. 22 m, and its width is around 60 m (Figure 5.2). The GB-SAR is mounted on the roof of the building, centred respect the cultivated area in order to minimize the squint angles. The height above the field is 23 m. The incidence angles of the radar in the test field are from 55˚at near range to 67˚ at far range (Figure 5.3).

Figure 5.1 EEABB Test Field during the barley crop campaign. The location of the radar can be seen on the roof of the building

Two years before the beginning of the campaign, a 50 cm thick layer of soil was added over the original field surface. Due to its origin, the field shows different soil characteristics, as texture and structure. The heterogeneity origin of the soil is reflected in a highly dispersive value of soil moisture together with a non-uniform growth of the crops.

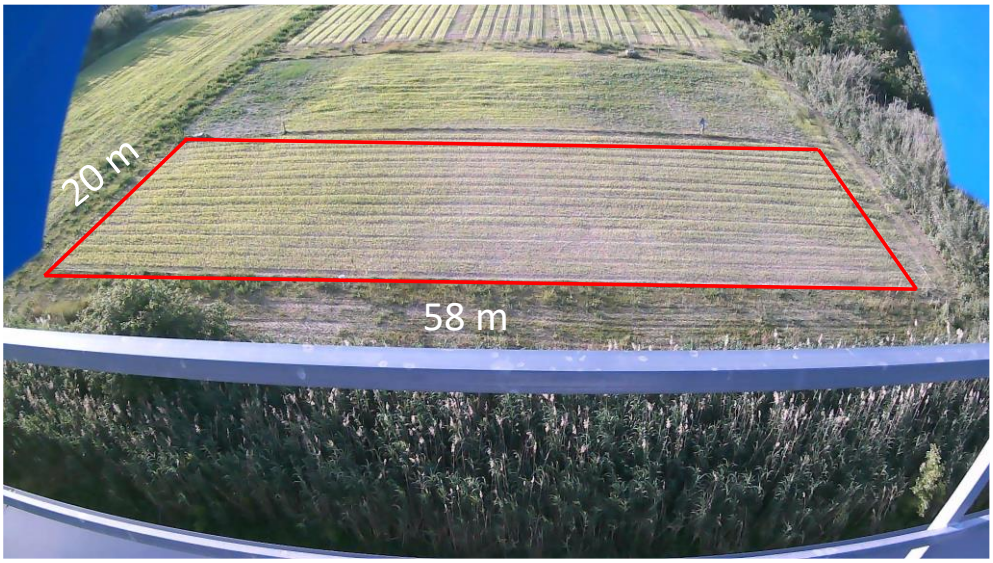

Figure 5.2 Photograph of the test area from the radar installation point.

In Table 5.1 the analysis of two samples obtained from the field is shown, where significant differences in main parameters can be observed, as variation in organic matter (variation of 46%), total carbonates (variation of 46%), electrical conductivity (variation of 60%) or soil classification

clay loam and loam. Under a productive point of view, these variations can affect the development of the crop.

The same Table 5.1 underlines the variation of the characteristics of the soil. The soil texture indicates the ability to retain water. The contents of organic matter (< 1%) is below the recommended limits of 2% for agriculture. This soil is classified as sodic soil non-saline. It has enough content of Sodium to affect crop production.

Parameter	**Results Zone A**	**Results Zone B**	**Units**
Analytic determination of the soil			
pH H_2O (1:2.5)	8.46	8.31	
pH KCL (1:25)	7.91	7.78	
Organic matter	0.81	1.74	%
Total nitrogen	0.057	0.113	%
Organic carbon	0.47	1.01	%
Relation C/N	8.25	8.94	
Total carbonates	19.1	11.7	%
Active calcareous	70.29	25.5	‰
Phosphor assimilable	8	25	mg/kg
Electrical Conductivity (EC)	0.147	0.245	mmhos/cm
Calcium assimilable	55.06	59.94	cmolc/kg
Magnesium assimilable	1.90	2.19	cmolc/kg
Sodium assimilable	0.26	0.31	cmolc/kg
Potassium assimilable	0.39	0.39	cmolc/kg
Potassium assimilable	151	151	mg/kg
Soluble salts	57.61	53.83	cmolc/kg
Cation exchange capacity	12.63	14.75	cmolc/kg
Saturation percentage	100	100	%
Granulometry			
Parameter	Results Zone A	Results Zone B	Units
Sand thick (2 a 0.5 mm diameter)	12.71	29.07	%
Sand slim (0.5 a 0.05 mm diametre)	12.50	9.93	%
Silt thick (0.05 a 0.02 mm diameter)	19.21	9.67	%

Silt slim (0.02 a 0.002 mm diameter)	27.83	27.33	%
Clay (<0.002 mm diameter)	27.75	24.00	%
Texture (USDA)	Loam – Clay loam	Loam	

Table 5.1 Soil analysis of the field of two separated zones (Source: Project ICEGAP-EEABB 2021).

The water table is really high, being at a depth of less than 1 m from the ground surface. This causes high content of humidity at relatively low depth.

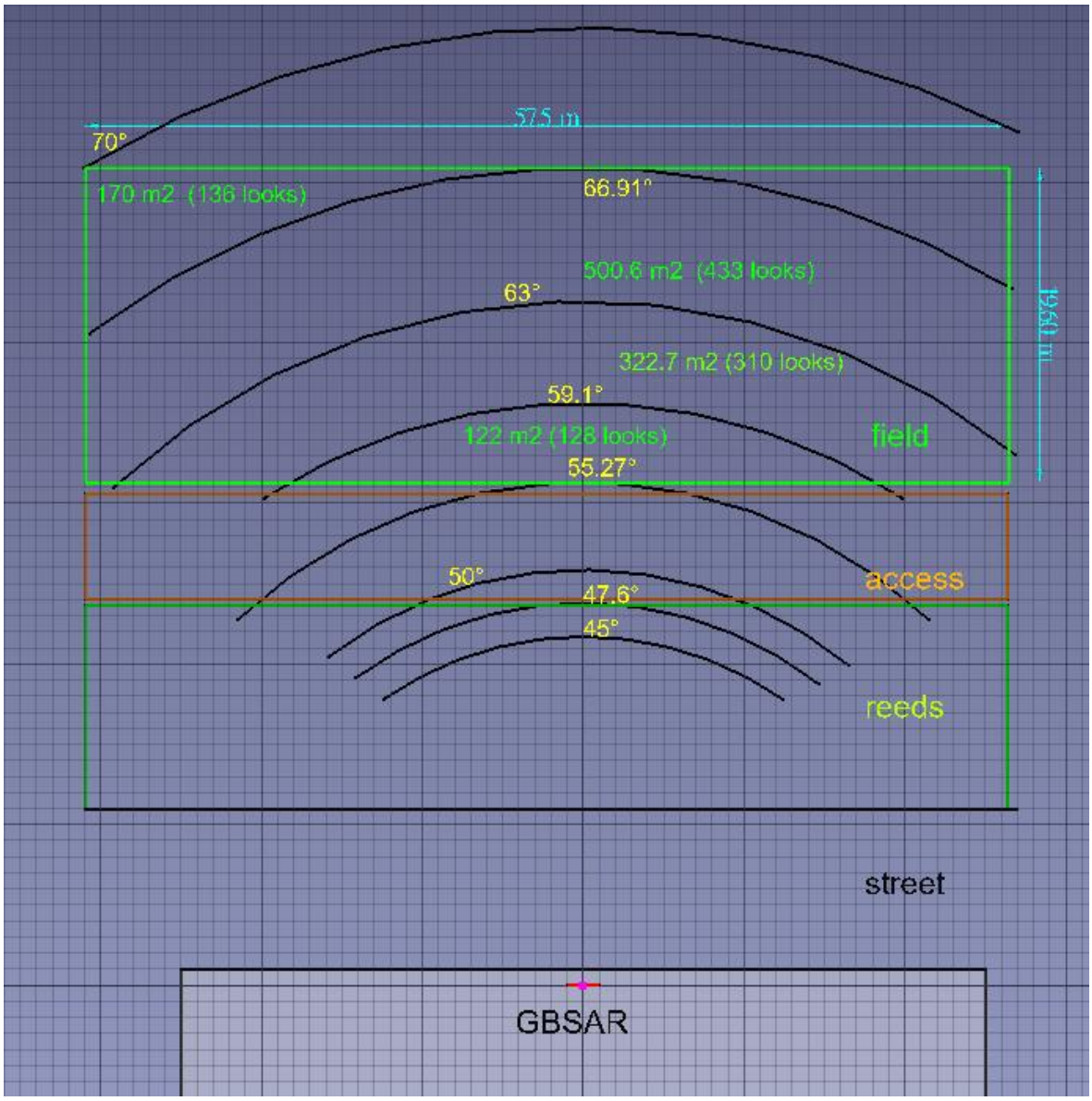

Figure 5.3. Top view geometry and number of looks of EEABB Test Field for different incident angle ranges, indicated in yellow. The light green rectangle is the crop area. Radar location is labelled with GBSAR on the roof of EEABB building. Black arcs are iso-range/iso-incidence angle lines. The small grid spacing is 1 m.

5.2 GBSAR

The main instrument is a C-band, Full-Polarimetric Ground Based Synthetic Aperture Radar (Figure 5.4, Figure 5.5), with two independent Zero-IF receivers and one transmitter chain. A Solid-State Microwave Switch is connected among the transmitter and two orthogonal polarized antennas. Each of the two receiver chains is connected respectively to one of the two orthogonally polarized receiving antennas.

The frequency generation unit is a Direct Digital Synthesis (DDS) that generates a stepped linear frequency modulated continuous wave (SLFM-CW) chirp signal from a thermally stabilized (±2ppm in the 0°C - 70°C temperature range) frequency reference (Temperature Compensated Quartz Crystal Oscillator).

The radiation elements consist of four units of 10 dB Gain pyramidal horn antennas with an azimuth beamwidth of 60˚ and an elevation beamwidth of 40˚ (Figure 5.6). The decision to use pyramidal horn antennas was done based on different aspects, such as beamwidth, polarimetric response, total weight, physical dimensions, etc. The beamwidth had to be wide enough to illuminate the whole field while ensuring a polarimetric purity of, at least, 25dB. The set of four antennas had to be stiff enough to withstand the repetitive mechanical movement of the rail and the outdoor conditions. With horn antennas, the wide beamwidth can only be reached with electrically small antenna apertures which limits their polarimetric purity performance. Thus, a compromise between beamwidth and polarization purity had to be assumed.

The system Equivalent Isotropic Radiated Power (EIRP) accomplishes the limit of the Spanish Regulation *UN-128 5 GHz RLAN* and *CEPT ECC/DEC/(04)08* [2], nonetheless the transmitted power is switched off while the system is not measuring.

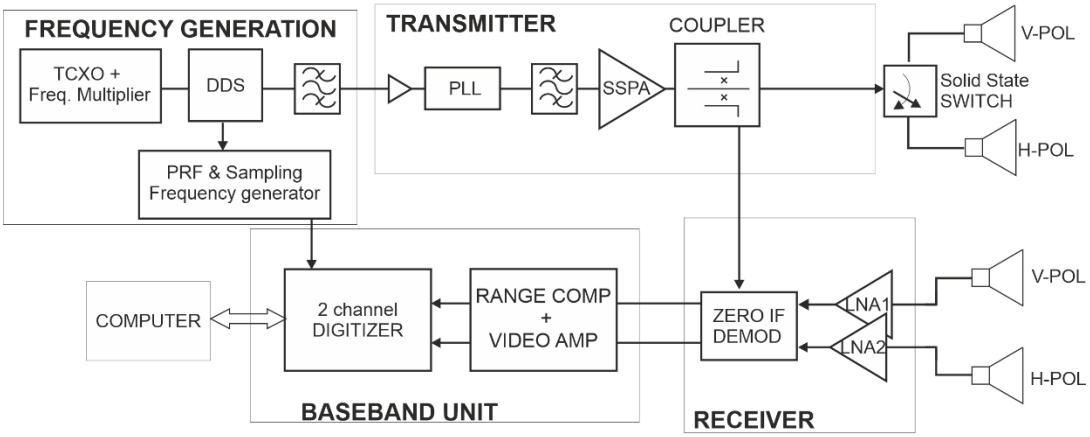

Figure 5.4 Block diagram of the RADAR electronics

Received signals are down-converted by means of a sample of the transmitted signal as the Local Oscillator. A pair of range compensation filters and amplifiers are inserted to adjust the dynamic range to the digitizer unit.

The base-band signals are digitized by a commercial 14 bit, 2 channels, high speed digitizer controlled by the main computer. Both V and H polarization echo signals are synchronously digitized using trigger and clock references that are coherently generated by the DDS clock. The synchronized digitizing process ensures repeatability in the acquisition of the four polarization channels.

The radar electronics is in a splash-proof box. This box includes a thermal stabilization system to minimise gain, phase and frequency variations due to external temperature changes.

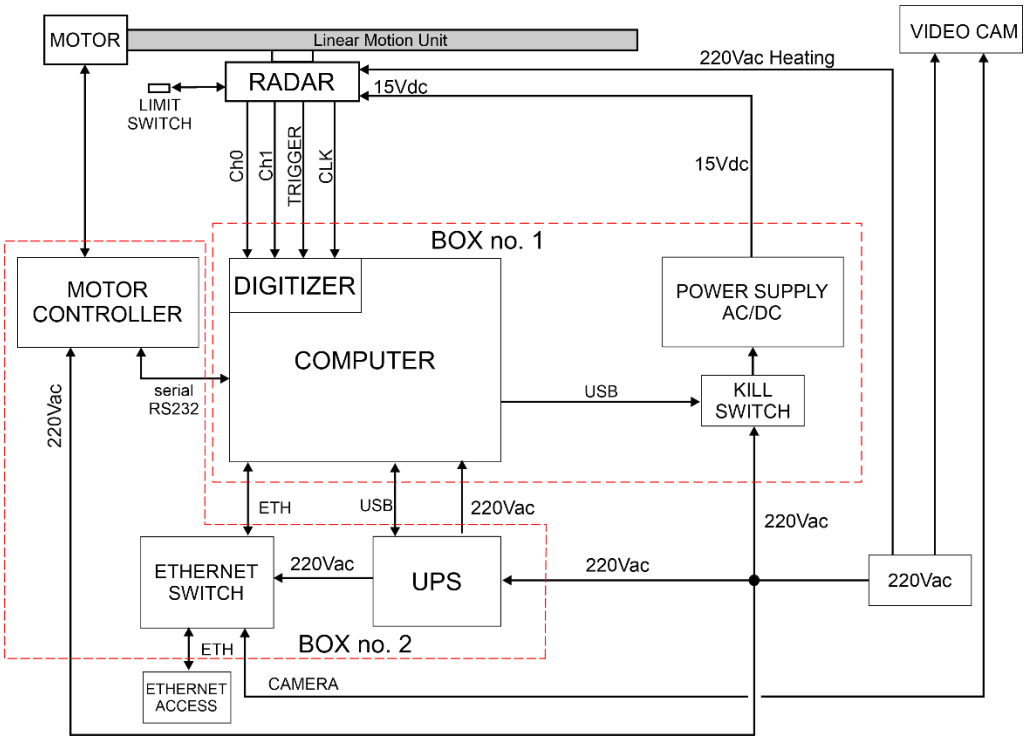

Figure 5.5 System Architecture

The RADAR is mounted on a linear motion unit, capable of performing up to 2 m long apertures. The rail includes a magnetic sensor in a fixed position that determines the origin of the aperture, repeatable FM transmitted waveform generation and echo digitization. The aperture length and rail speed are fully controllable, with a speed limit of 1 m/s. The linear motion unit is attached to a rigidized steel frame (Figure 5.7).

Figure 5.6. The radar is suspended from the rail. The four pyramidal horn antennas can be seen pointing to the field with a tilt angle.

The ground-based SAR system has been operated in a 24/7 service, taking a 1.47 m long, 1 m/s aperture measurement every 10 minutes.

Figure 5.7. The Metallic structure that holds the rail is attached to the building and uses struts to reduce any swing (left). Supplementary electronics are installed in two weatherproof cabinets (right).

The following table summarizes the main parameters of the RADAR (Table 5.2).

Parameter	Value
Central Freq. (Barley/Corn)	5.5/5.6 GHz
Freq. Bandwidth (Barley/Corn)	196.2/200 MHz
Mode of Operation	Full-Polarimetric
Modulation	Saw-Tooth FM-CW
Peak Transmitted Power	28.7 dBm EIRP
Chirp PRF	338.5 Hz
Ramp duration	1.47 ms
Platform velocity	1 m/s
Synthetic aperture length	1.477 m

Receiver Gain	40 dB
Receiver Noise Figure	2 dB
Antenna Gain	9.7 dB
3dB Antenna Beamwidth	60˚ (Azi), 40˚ (Elev)
Base Band Beat Frequency (Barley/Corn)	885.6/902.8 Hz/m
ADC resolution	14 bits
No. of samples/ramp sweep	2048

Table 5.2 Main RADAR parameters.

5.3 Data Processing

5.3.1 SAR Processing: Time Domain Reconstruction-Time Domain Correlation (Start-Stop Approximation)

A Back-Projection Algorithm (BPA) has been used in spite of its high computational cost. The BPA offers a high degree of flexibility in focusing extended images from arbitrary synthetic apertures limited either by antenna beam, linear track or data acquisition capacity. After range compression, the BPA essentially performs a coherent addition for each SAR image pixel of the back propagated data acquired along the synthetic aperture. The focusing process can be analysed in a simplified way as follows,

The transmitted chirp signal for the radar is

$$p(t) = a(t)e^{j\left(\omega_0 t+\frac{\alpha}{2}t^2\right)} \tag{5-1}$$

Where $\mathrm{a(t)}$ is the envelope, ω_0 the angular frequency of the carrier and α the chirp rate. The baseband received signal, after de-ramping and low pass filtering, can be expressed as

$$s_d(t,u) = \int_{R'} \Psi(\vec{r}')\, G(\vec{r}',t,u)\mathrm{a}(\vec{r}';\mathrm{t}-\mathrm{t_n})\, e^{j\Phi(\vec{r}';t,u)} d\vec{r}' \tag{5-2}$$

where $\Psi(\vec{r}')$ is the field reflectivity, R' the illuminated area, $G(\vec{r}',t,u)$ models the transmitter and receiver antenna patterns, u the radar position, $\mathrm{t_n}$ the round trip-trip delay for the echo signal and $\Phi(\vec{r}';t,u)$ is given by

$$\Phi(\vec{r}';t,u) = -\omega_0 \mathrm{t_n}(\vec{r}',t,u) + \frac{\alpha}{2}\mathrm{t_n^2}(\vec{r}',t,u) - \alpha \mathrm{t}\mathrm{t_n}(\vec{r}',t,u) \tag{5-3}$$

The reflectivity image can be reconstructed convolving $s_d(t,u)$ with an inverse Green's function

$\zeta^{-1}(t,u;\vec{r}')$

$$\Psi(\vec{r}') = \int_{-\infty}^{\infty}\int_{-\infty}^{\infty} W(t,u;\vec{r}')s_d(t,u)\zeta^{-1}(t,u;\vec{r}')\ \ dudt \tag{5-4}$$

where $W(t,u;\vec{r}')$ is a windowing function for sidelobes reduction and the focusing operator $\zeta^{-1}(t,u;\vec{r}')$ can be expressed as

$$\zeta^{-1}(t,u;\vec{r}') = \frac{e^{-j\Phi(\vec{r}';t,u)}}{G(\vec{r}',t,u)} \tag{5-5}$$

The computational cost of the Time Domain Correlation (TDC) algorithm is too high and some approximations can be done to reduce the cost. Assuming the start-stop approximation is valid $\mathrm{t_n}(\vec{r}',t,u) = \mathrm{t_n}(\vec{r}',u)$ and the window function is separable in two terms

$$W(t,u;\vec{r}') = W_a(u)W_r(t) \tag{5-6}$$

and $G(\vec{r}',t,u) \approx G(\vec{r}')$

The expression for the reflectivity can be simplified as,

$$\Psi(\vec{r}') = \frac{1}{G(\vec{r}')}\int_{-\infty}^{\infty} W_a(u)e^{j\omega_0 \mathrm{t_n}(\vec{r}',u)}e^{-j\frac{\alpha}{2}\mathrm{t_n}^2(\vec{r}',u)}\left(\int_{-\infty}^{\infty} W_r(t)s_d(t,u)\ e^{\mathrm{j}\alpha t\mathrm{t_n}(\vec{r}',u)}\ dt\right) \tag{5-7}$$

$$\Psi(\vec{r}') = \frac{1}{G(\vec{r}')}\int_{-\infty}^{\infty} W_a(u)e^{j\omega_0 \mathrm{t_n}(\vec{r}',u)}e^{-j\frac{\alpha}{2}\mathrm{t_n}^2(\vec{r}',u)}S(\omega+\alpha\mathrm{t_n},\mathrm{u};\vec{r}')\,du \tag{5-8}$$

where $S(\omega+\alpha\mathrm{t_n},\mathrm{u};\vec{r}')$ is the Fourier transform of $s_d(t,u)$ (range compression).

From equation (5-8) it can be seen that the reflectivity image is obtained from two steps: a range compression of raw data and a following Back Projection focusing process.

5.3.2 SLC images

The SLC images have been generated from equation (5-8) in polar coordinates (R_0,ψ) (Figure 5.8). A Tukey (tapered cosine) window with α=0.5 has been used in both range and cross-range. This window presents a highest side lobe level of -15 dB and a 3dB Bandwidth (bins) of $f_{window-3dB}$ =1.15. The area of the resolution cell on the ground can be calculated as:

$$A_{cell} = f_{window-3dB}^2\,\delta_r\delta_a \tag{5-9}$$

Where $\delta_r\ and\ \delta_a$ are the ground range and azimuth pixel resolution, respectively.

$$\delta_r = \frac{c}{2Bsin(\theta)} \tag{5-10}$$

$$\delta_a = \frac{R_0 \lambda}{2Lcos(\psi)} \tag{5-11}$$

Where L is the aperture length. These resolutions would degrade in case of using tapering windows in SAR processing to reduce sidelobes.

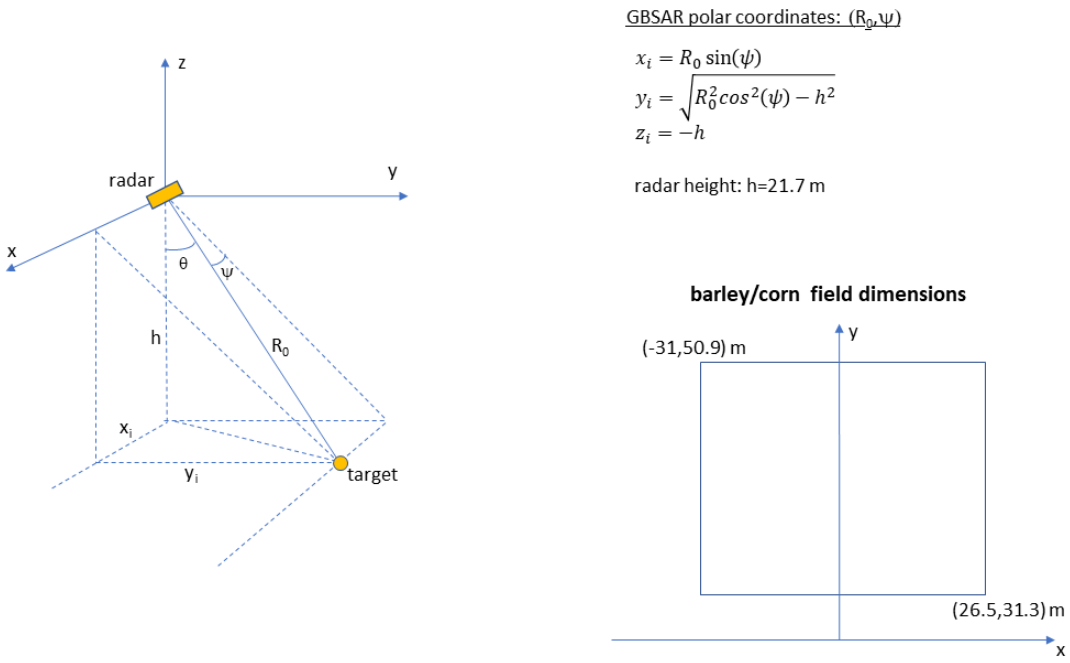

Figure 5.8 GBSAR polar coordinates and field dimensions

Once the calibration has been carried out, the pixels corresponding to each of the three angular sectors with 55.2° - 59.1°, 59.1° - 63° and 63° - 66.9° incidence angles have been selected. The backscattering coefficient (σ_0) corresponding to each sector has been obtained by averaging these pixels. The estimated number of looks in each sector are 138, 336 and 483 respectively.

5.4 Radar Calibration

Calibration is an accuracy enhancement procedure that tries to remove the systematic errors that cause uncertainty in the measures. In order to do that, an error model of the system to calibrate is defined that will determine the number of unknown parameters required for correcting the measures. These unknown parameters are calculated with the measurement of standards whose response is well known. The number of unknowns sets the minimum number of independent measures over these standards. On the contrary, random errors are unpredictable since they vary randomly with time. As they do not have a model, they cannot be removed by calibration.

The calibration only compensates systematic errors, those related to signal leakage, signal reflections, frequency response of the circuitry, antenna radiation patterns, etc. Some systematic errors may present a temporal drift and, as a consequence, would require a re-calibration of the

system. Temperature variations of the circuitry is a usual cause of temporal drifts. The main contributors to random errors are caused by the noise generated in the instrument circuitry.

Figure 5.9 shows the different parts of the RADAR instrument that can introduce uncertainties to be compensated in the calibration process.

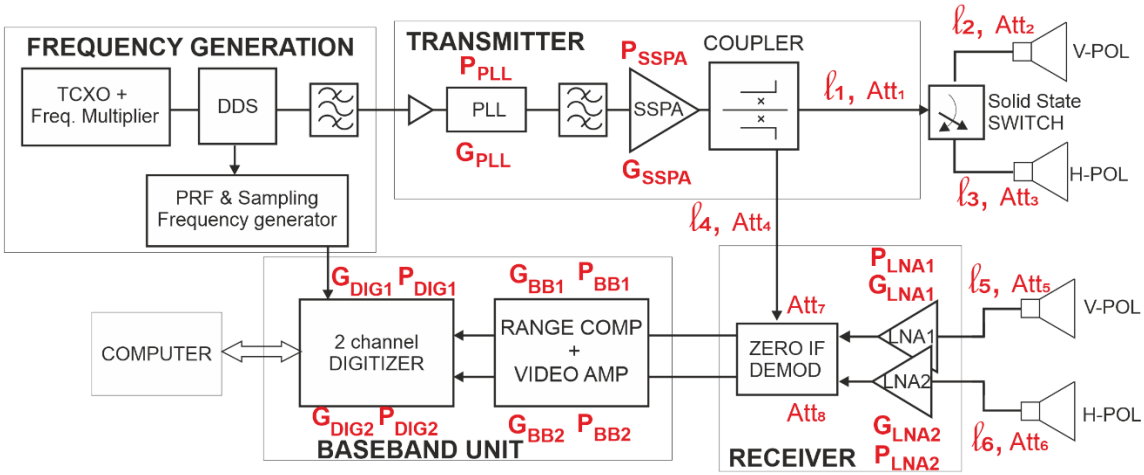

Figure 5.9 Internal structure of the RADAR. Different uncertainties can be found that affect the system calibration. G stands for the Gain, Att for Attenuation, P for Phase and ℓ for electrical length (an equivalent effect of change in Phase).

The frequency generation unit could drift in frequency with impact on image phase and ranging accuracy. The rest of elements can introduce a change in gain and/or phase, as a function of the internal temperature or due to aging. Gain variation over temperature of different elements usually is a negative factor on the order of -0.01 dB/°C while Phase variation is negligible. Laboratory measurements showed a total Gain variation over temperature for both receiving channels on the order of -0.1 dB/°C, while in situ internal temperature drift measurement of the radar has been estimated with a standard deviation of 0.3 °C and a total deviation of 1.5 °C.

For the particular case of a radar, in addition to the inaccuracies due to the instrument, the two-way path changes between the radar and the elements of the scene have to be considered as well. For example, the changes in the speed of propagation of the electromagnetic waves induced by the variant atmospheric conditions.

The traditional calibration of polarimetric radar systems use both external calibrators with a controlled polarization signature, like corner reflectors, spheres or dihedrals, and natural elements of the scene. The quality of the calibration depends on the quality of the calibrator.

The complete error model can be defined with the following equation (5.12) [3],

$$\begin{bmatrix} S_{HH} & S_{HV} \\ S_{VH} & S_{VV} \end{bmatrix}_{meas} = K(\gamma) \begin{bmatrix} f_R(\gamma) & \delta_1^R \\ \delta_2^R & 1 \end{bmatrix} \begin{bmatrix} S_{HH} & S_{HV} \\ S_{VH} & S_{VV} \end{bmatrix}_{real} \begin{bmatrix} f_T(\gamma) & \delta_1^T \\ \delta_2^T & 1 \end{bmatrix} \quad (5.12)$$

$$[R] = \begin{bmatrix} f_R(\gamma) & \delta_1^R \\ \delta_2^R & 1 \end{bmatrix} \qquad [T] = \begin{bmatrix} f_T(\gamma) & \delta_1^T \\ \delta_2^T & 1 \end{bmatrix}$$

γ is either the look angle or the local incidence angle, $[T]$ and $[R]$ are the transmit and receive system distortion matrices that include not only the differences in the antenna patterns for each polarization but also patterns and path length differences in the two receiver chains. f_T and f_R represent the ratio between the co-polar channels in transmission and reception respectively while δ_1^T, δ_2^T, δ_1^R and δ_2^R the cross-talk between cross-polar channels, H to V and vice versa, in both transmission and reception.

The calibration of all parameters is not straightforward and it would require the deployment of a large set of calibrators along the scene. Assuming that the instrument presents a good polarization isolation the cross-talk terms can be ignored and the model can be simplified,

$$\begin{bmatrix} S_{HH} & S_{HV} \\ S_{VH} & S_{VV} \end{bmatrix}_{meas} = K(\gamma) \begin{bmatrix} f_R(\gamma) & 0 \\ 0 & 1 \end{bmatrix} \begin{bmatrix} S_{HH} & S_{HV} \\ S_{VH} & S_{VV} \end{bmatrix}_{real} \begin{bmatrix} f_T(\gamma) & 0 \\ 0 & 1 \end{bmatrix} \quad (5.13)$$

The system of equations can thus be rewritten as,

$$\begin{aligned} S_{HH}^m &= K \cdot f_R \cdot f_T \cdot S_{HH} & S_{VV}^m &= K \cdot S_{VV} \\ S_{HV}^m &= K \cdot f_R \cdot S_{HV} & S_{VH}^m &= K \cdot f_T \cdot S_{VH} \end{aligned} \quad (5.14)$$

In monostatic systems it is fulfilled that $S_{VH} = S_{HV}$ and so an additional equation can be derived,

$$S_{HV}^m = {f_R}/{f_T} \cdot S_{VH}^m \quad (5.15)$$

After a correction of the range response (in phase and amplitude) of the two receiver chains and the antenna pattern for each point of the image, the error terms of the radar system can be removed using the polarimetric calibration proposed by Kamal Sarabandi [4]. This calibration method, under the assumption of good antennas polarisation isolation, requires a reference target of known scattering matrix, like a trihedral, and a target with a strong cross-polarized RCS.

Some of the errors included in the above equations had been previously characterized and, thus, they are corrected at a first stage:

- The radiation patterns of all the antennas involved in the measurement have been characterized in the CommSensLab anechoic chamber, allowing correcting the antenna pattern on backscattering images to be carried out in a separate step.
- The receiver amplifiers for each polarization present a gain that changes with range that was characterized at CommSensLab facilities. The proper correction is directly applied to the measured data for each polarization channel. Due to the internal structure of the receiving amplifier chains, a slight global drift in gain and phase due to aging or thermal residual changes can be expected.
- The main impact of atmospheric changes, given the short operating distance of HydroSoil campaign, is a range dependent phase drift caused by alterations in the speed of propagation of the radar signals. This can be effectively compensated based on a refractive index model using in-situ meteorological station measurements of air humidity, pressure and temperature (data level 1c).

In order to properly calibrate the images produced by the GB-SAR, two elements of the instrument have to be independently characterized: the frequency response of the receiver channels and the

radiation performance of the antennas. The gathered information is used in the polarimetric-radiometric calibration process.

Frequency response variation in the receiver channels translates to an error function that is range dependant in the SLC images. This error function (Figure 5.10) is characterized at the laboratory and compensated in the SLC image formation.

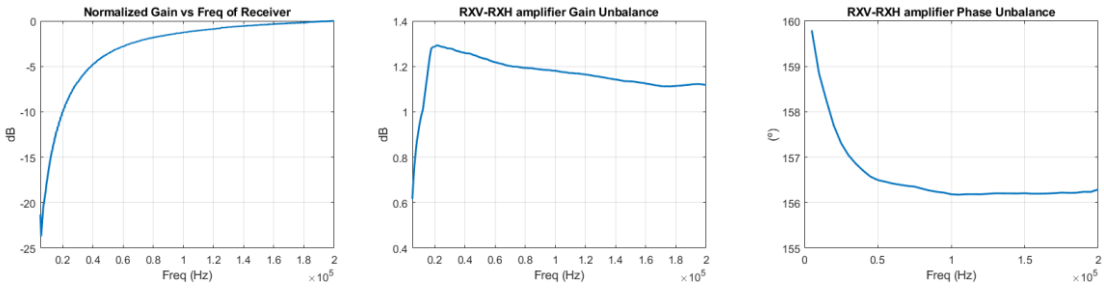

Figure 5.10. Power Gain (left), Gain and Phase unbalance (center and right) of the equivalent downconverter receiver amplifiers for the barley campaign.

The antenna pattern along the scene (Figure 5.11) for the different polarization combinations induces the alteration of the true SLC's reflectivity. The SLC maps can be compensated if all antennas involved in the measure have perfectly characterized radiation patterns. The set of antennas has been fully characterized at the anechoic chamber of CommSensLab (Figure 5.12).

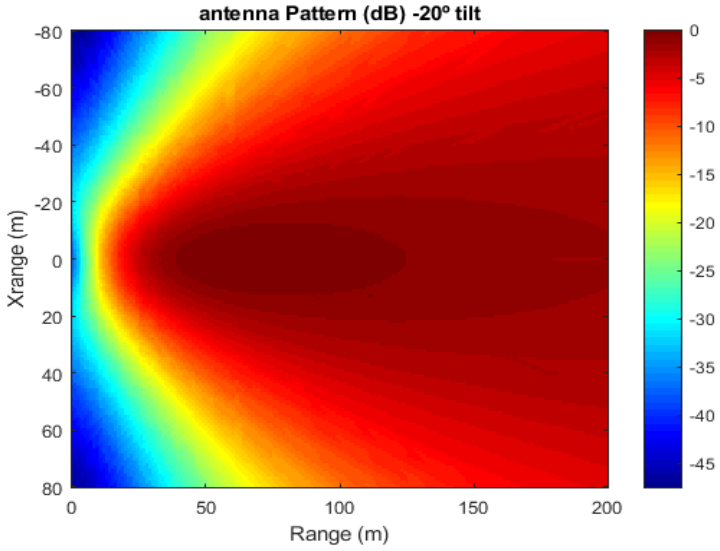

Figure 5.11.Example of the VV-channel antenna pattern map for a -20° antenna tilt

Originally, in the preparation of the barley campaign the four pyramidal horn antennas were 3D printed with PLA plastic and metalized just to validate their design. It was planned to replace them by brass based radiating elements during the first part of the campaign, but due to COVID-19 outbreak they had to be maintained until the end of the campaign. The plastic material (PLA) used in the additive fabrication process of the antennas is sensitive to solar radiation, temperature and

humidity. In the first revision of the radar (5 May 2020) a significant deformation of the geometry of the antennas was detected. This deformation could have affected the polarimetric performance of the system. After the barley campaign, the antennas were measured to check the degradation of their polarimetric responses (Figure 5.13, Figure 5.14).

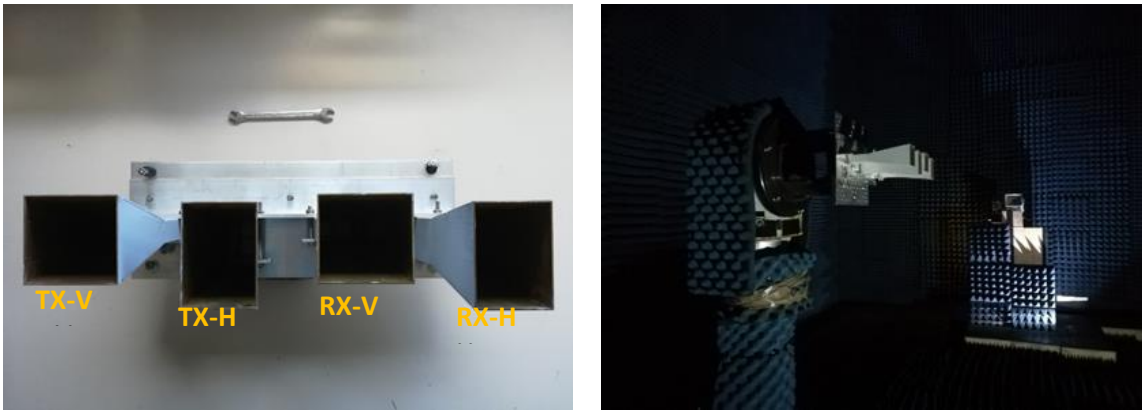

Figure 5.12 (Left) The set of four pyramidal horn antennas of the radar. (Right) The antenna diagram and polarization performance were measured in the CommSensLab anechoic chamber.

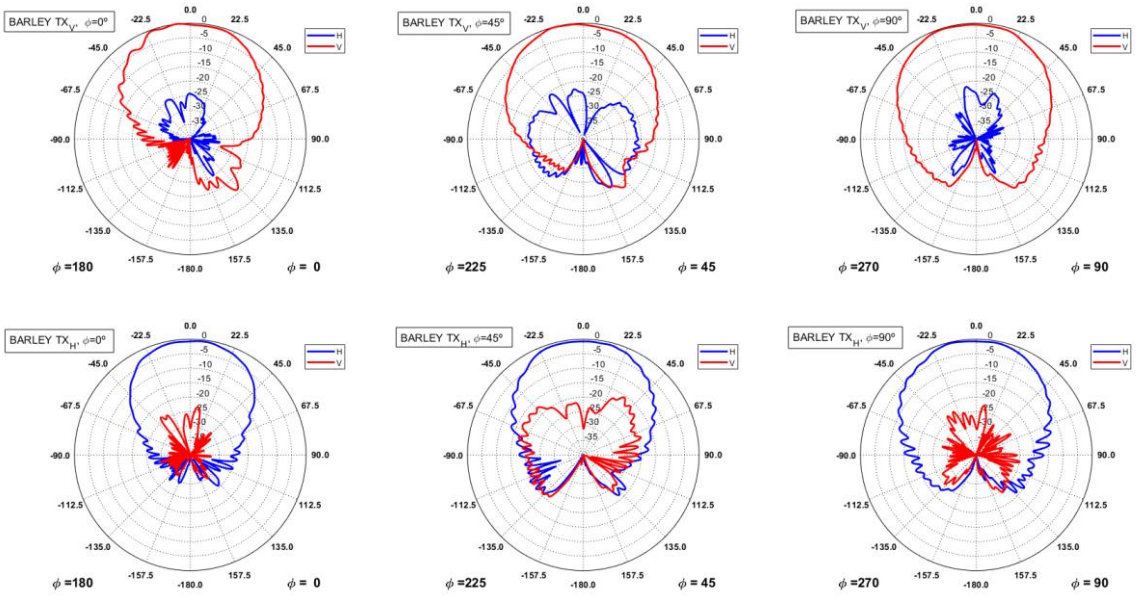

Figure 5.13. V and H cuts in θ of the Vertical (Top) and Horizontal (Bottom) Transmitter Horn Antennas for different ϕ angles for the barley campaign. These measurements were done after the end of the barley campaign.

Before the corn campaign, a new set of identical pyramidal horn antennas was built using brass plates. The co-polar and cross-polar radiation patterns were measured before installation, which are shown in Figure 5.14

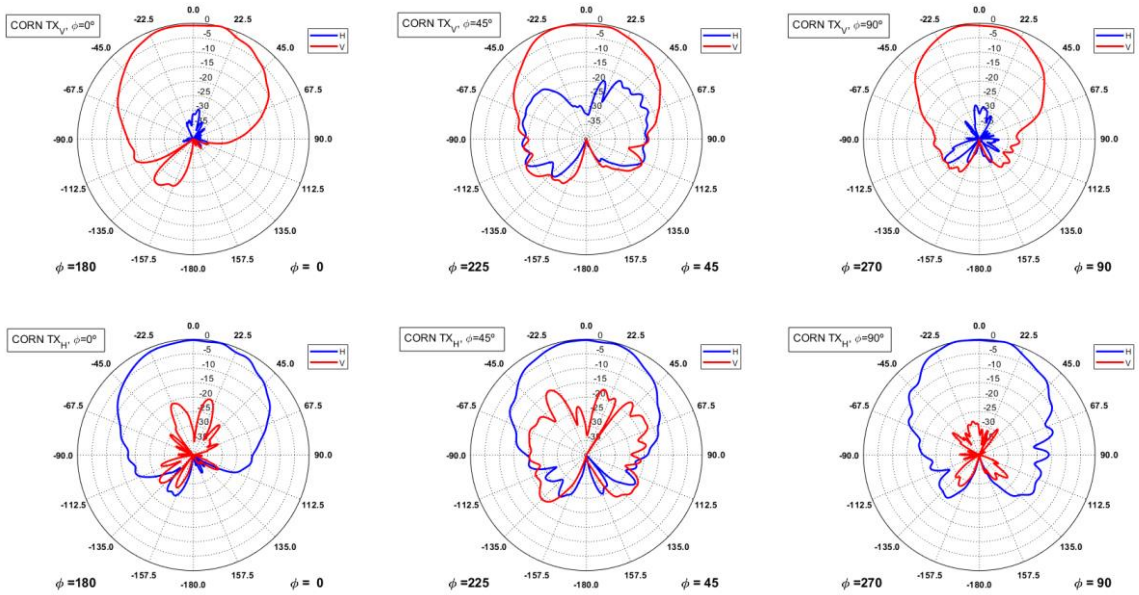

Figure 5.14. Corn Campaign. V and H cuts of the Vertical (Top) and Horizontal (Bottom) Transmitter Horn Antennas for different ϕ angles for the corn campaign.

5.5 SAR Data Products

Ground Based SAR data with incidence angles between 55◦ and 67◦ with a temporal resolution of 10 minutes are provided. Two Single Look Complex (SLC) products have been generated:

- Calibrated data (level 1b). Complex data in SLC images have the following information: $\sqrt{\sigma^0}e^{j\emptyset_{scattering}}e^{-j2kr}$ where σ^0 is the backscattering coefficient.

- Calibrated data with atmospheric refraction index changes correction (level 1c). Atmospheric phase screen compensation has been generated with the information collected by the Local Weather Station. Considering the size of the test site, refractive index changes have been evaluated and compensated from the atmospheric ancillary data provided by the local Weather Station installed at the test field [5] as described in Section 7.4.6.5. To generate this product, atmospheric phase screen compensation has been applied to the entire data set level 1b.

Owing to the COVID-19 lockdown access restrictions to the field, only one Corner reflector was deployed during the main part of the barley campaign. A second radar calibrator, a 45° rotated dihedral in a squint angle, was installed just after the lockdown. Owing to these circumstances in this campaign, only the SLC co-polar (HH,VV) components have been obtained and dual-pol files are provided. In the corn campaign, a corner reflector and a 45° rotated dihedral were already available from the beginning, which has allowed the generation of full-pol data (HH,HV/VH,VV).

The SLC images have been generated in polar coordinates (R_0, ψ) (*Figure 5.8*). The size of the images is: ψ from -40° to 40° and R_0 from 30m to 65 m for the barley campaign and R_0 from 30 m to 90 m for the corn campaign. The slant range, ground range and azimuth pixel resolution, corresponding to a point in the middle of the crop field with R_0 = 44.75 m, $\psi = 0°$ and $\theta = 61°$, are δ_{sr} = 70 cm, δ_{gr} =

86 cm and δ_{az} = 82 cm respectively.

5.6 Special Radar Observation Modes

5.6.1 Real aperture Doppler spectrum mode

The system can be configured as a 1D Real Aperture Radar (RAR), in order to evaluate the influence of wind and crop stage in the radar response. In this operation mode, the instrument can be used to determine the Doppler spectrum spreading due to vegetation swinging.

Doppler Spectrum spreading forced by the crop is evaluated as follows: The radar is placed in a fixed position of the rail. Radar takes a measurement for a period of 6 seconds. Radar signal is range compressed and the time evolution of the different range cells are converted in frequency spreading. Radar measurements were taken when the crop was stable in height but for different wind conditions. The Doppler spectrum of the range cells from Near Range to Far Range of the field are averaged.

5.6.2 Slow GEOSAR aperture mode

A set of SAR apertures, slowing the rail speed, or combining the raw data from consecutive apertures to generate an equivalent ultra-slow aperture, as the ones generated by GeoSAR Systems, have been conducted in order to assess the impact of scene temporal decorrelation in GeoSAR imagery.

Slow Synthetic Apertures, can be formed by appropriate combination of sub-apertures obtained from consecutive fast apertures (Figure 5.15).

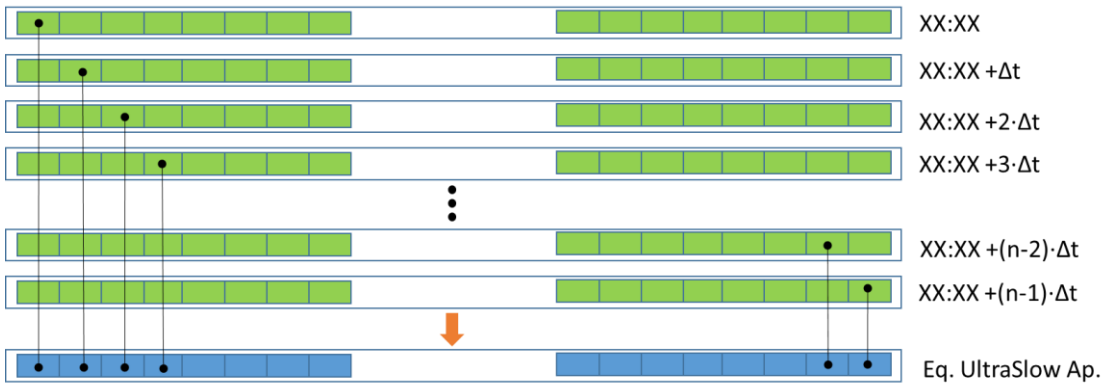

Figure 5.15 Different segments of the raw-data of consecutive fast sub-apertures are combined in order to generate an equivalent Slow aperture, with integration times comparable to GeoSAR Systems.

5.7 Ancillary data

A complete set of ancillary data have been collected along the barley and corn campaigns in order to provide the necessary ground truth for radar data interpretation, modelling and eventual radar data exploitation for sensing parameters of interest. The basic ancillary data collection provided by ground-based measurements are:

- Soil moisture: volumetric soil moisture using both electronic probes with continuous monitoring and periodic gravimetric measurements
- Soil roughness: representative roughness transects using laser profilers complemented by photogrammetric measurements after sowing barley and corn. Statistical information: roughness standard deviation, correlation length, electrical parameters (defined in 6.3.1): ks, kl, s/l.
- Vegetation sampling: plant density, planting row direction, size and orientation of main plant elements, biomass and crop phenology, Leaf Area Index (LAI), crop height and vegetation water content.
- Meteorological parameters: barometric pressure, precipitation, temperature, humidity, wind speed and direction, solar irradiation.
- Detailed irrigation information for corn crop.

Additional details are provided in the barley and corn campaign descriptions (Sections 6.3 and 7.3).

6 BARLEY CAMPAIGN

Shortly after the start of the barley campaign, COVID-19 outbreak resulted in a complete closure of UPC facilities from 16 March 2020 until 8 June 2020. In the whole country, people not working on essential activities were confined at home. Access to UPC facilities was granted under request only for extremely justified reasons (like critical activities on active projects) and very limited in time. Since the radar was designed to operate autonomously with automatic acquisition routines and remote-control capabilities, this closure had a little impact on the data takes nor the barley crop growth under monitoring.

6.1 Barley crop description

Barley (*Hordeum vulgare L.*) is an annual grass in the family *Poaceae* of 20-120 cm high which tolerates low temperatures and resists drought well, although it needs water at the beginning of its development. It has a wide range tolerance to soil acidity and salinity but it does not tolerate waterlogged (which occurred in 19 April) and clay soils. It can be established in stony and shallow soils.

Barley is a widely adaptable cereal grain crop. Barley can be sown as a winter crop or as spring crop. It requires minimum temperatures of 1–2 °C for successful germination. Spring barley varieties usually reach maturity in 60 to 80 days while winter barley in 60 days.

The plant variety seeded was: *Hordeum vulgare L.* SOLIST. This variety was obtained by Saatzucht Streng-Engelen (Germany) on December 2012. It is a two-rowed type cereal characterized by premature ear rising and maturity.

The water content of the ground has a great effect on the growth of the crop. Low content of water, especially during germination lead to a low production. In addition, an adequate amount of Nitrogen component present on the ground has positive effects on tillering, turning into an increase from 1 to 3 tillers on each plant.

The productivity of the crop, expressed as dry matter increase, is consequence of the accumulated photosynthesis. In this sense, at the beginning of the crop, the low leaf surface allows a slow photosynthetic accumulation. As new leaves appear, the photosynthetic capacity has an exponential increase and, in consequence, the dry matter increases as well.

According to Zadoks two-digit code system for growth staging in barley [6], 10 stages are described (Figure 6.1,Table 6.1). Some of this growth stages were observed during field monitoring.

Zadoks code: Principal stage	Description	Date of observation
0	Germination	
1	Seeding development	
2	Tillering	5 May 2020
3	Stem elongation	
4	Boot	21 May 2020
5	Head emergence	
6	Flowering (not readily visible in barley)	4 June 2020
7	Milk development in kernel	
8	Dough development in kernel	12 June 2020
9	Ripening	

Table 6.1. Stages of the barley crop campaign

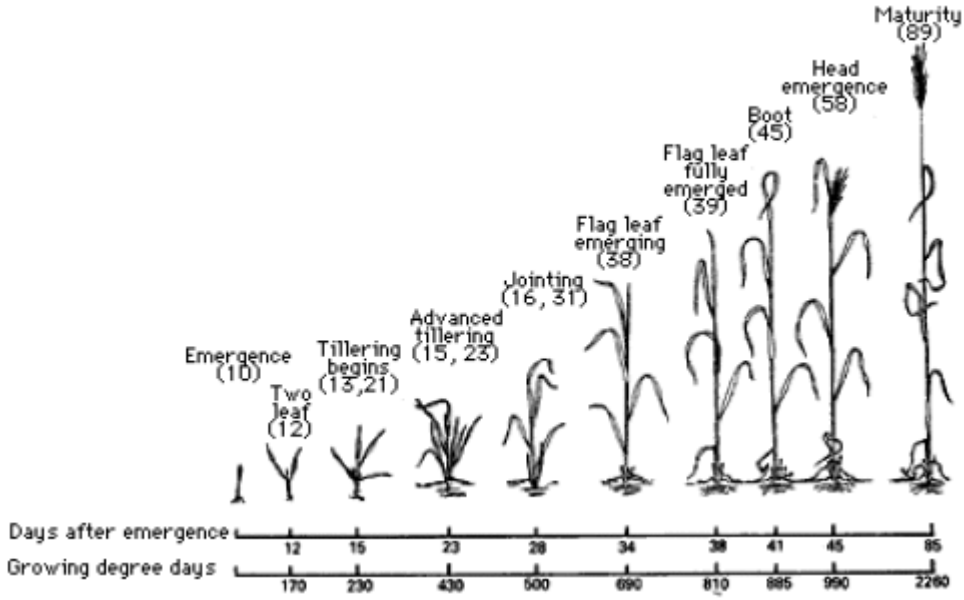

Figure 6.1. Evolution of the growth stage of the barley [6].

6.2 Chronology

The following table describes the main events of the barley campaign.

28 Feb – 2 March 2020	Radar installation
2 March – 6 June 2020	Radar operated in 24/7 mode, performing a measurement every 10 minutes
4 March 2020	Barley is sown
6 March 2020	Soil Roughness is measured with the Laser Ranger
12 March 2020	A Corner Reflector is installed at Far Range Right
14 March 2020	COVID-19 State of Alarm is declared in Spain. Mobility restrictions are applied and UPC facilities are fully closed
20 March 2020	2 EC5 Soil moisture + Weather Station (BME280) data logger is installed. Photogrammetric photos are taken for Soil Roughness determination.
1 April 2020	Non-programmed radar halt. From 9:46 - 13:25 Local Time
19-22 April 2020	190 l/m^2 intense rain period
29 April 2020	Non-programmed radar halt. From 8:30 - 13:00 Local Time
5 May 2020	Radar maintenance. Internal thermal Temperature is set to 40°. Mobility

	restrictions are lifted and UPC facilities are partially open
7 May 2020	Local Weather Station is installed. Samples for height, LAI, Plant Water Content, gravimetric soil moisture are taken.
13 May 2020	Human activity. The crop is manually fertilized. A disease affecting the crop is detected (Puccinia Hordei)
14 May 2020	Samples for height, LAI, Plant Water Content, gravimetric soil moisture are taken.
18 May 2020	Height is measured. Samples for LAI determination are collected
21 May 2020	Samples for height, LAI, Plant Water Content, gravimetric soil moisture are taken.
25 May 2020	Height is measured. Samples for LAI determination were collected. Radar did not operate from 9 to 16H.
28 May 2020	1-day Water Cycle Campaign. Samples for height, LAI, Plant Water Content, gravimetric soil moisture are taken.
1 June 2020	Height is measured. Samples for LAI determination are collected
4 June 2020	Samples for height, LAI, Plant Water Content, gravimetric soil moisture are taken. Radar is operated in Slow Aperture mode. Field extension is determined placing a Corner Reflector in different points of the field
5 June 2020	Radar is operated in Slow Aperture and RAR mode
6 June 2020	An anomalous performance of the radar is detected. Measurements from this date are not valid
12 June 2020	Barley harvesting

Table 6.2 Main events of the barley crop campaign

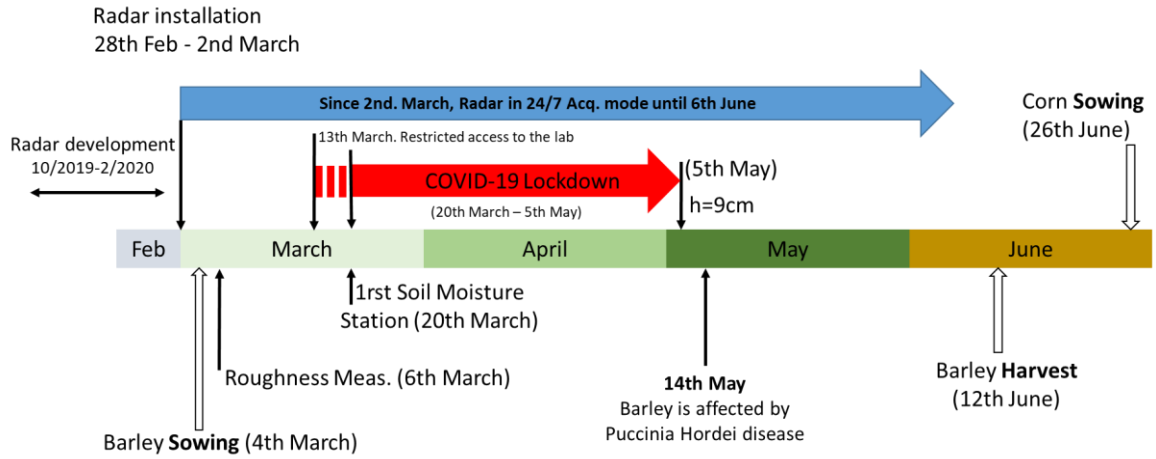

Figure 6.2. TimeLine and main events of the barley crop campaign.

6.3 Ancillary data

The ground measurement campaign has been planned considering ESA requirements and the suggestions proposed by the Mission Advisory Group (MAG). In order to ensure that the in-situ information is representative for the area covered by the radar beam, the different parameters are extracted from different points of the scenario.

6.3.1 Soil roughness

SAR measurements are very sensitive to soil roughness, which in agricultural fields is affected by the characteristics of tillage [8]. The parameterization of surface roughness and its spatial variability can pose major problems for soil moisture retrieval.

Soil Roughness was measured at the beginning of the crop campaign (6 March 2020), just after seeding (4 March 2020). The measuring instrument was based on a laser ranger (*LEICA Disto Pro*) on a linear motion unit of 2 m length (Figure 6.3, Figure 7.2). The soil roughness profile has been sampled every 2mm for the length of the rail. Different roughness profiles were taken from different places and orientations on the field. Due to limitations of COVID-19 outbreak, and after detecting anomalies in the registration with the laser profiler, photogrammetry profiles were used as a supplementary method. To characterize the surface roughness, the standard deviation of the surface height variation (or RMS height) and the surface correlation length are used [9]. The RMS height describes the vertical surface roughness while the correlation length, l, describes the horizontal distance over which the surface profile is autocorrelated with a value larger than *1/e*.

The values s (RMS height), l (Correlation length), $k \cdot s$ (the RMS height normalised to the wavelength), $k \cdot l$ (the correlation length normalized to the wavelength) and s/l (RMS height to correlation length ratio) are useful to characterize the roughness in terms of the wavelength by means of different criteria such as Rayleigh criterion, Fraunhofer criterion or scattering models such as small perturbation or Kirchhoff scattering model [9] [10]. Table 6.3, Figure 6.4 and Figure 6.5 show the retrieved parameters.

Figure 6.3. On 6 March 2020 soil Roughness was measured by means of a Laser ranger on a rail. Profile Samples were taken every 2 mm, at different positions of the field

PHOTOGRAMMETRY PROFILES	*s* (mm)	*l* (mm)	*k·s*	*k·l*	*s/l*
Near Range, Centre, (Cross Range)	9.83	11.13	1.15	1.31	0.88
Near Range, Centre, (Cross Range)	5.69	16.11	0.67	1.89	0.35
Mid Range, Right (Range)	5.72	36.32	0.67	4.26	0.16
Far Range, Right (Range)	11.03	40	1.29	4.69	0.28
Average value	**8.07**	**25.89**			
Std. Dev	**2.40**	**12.46**			
LASER PROFILES					
Mid Range, left (Range)	7.03	88	0.82	10.32	0.08
Far Range, Left (Range)	11.76	102	1.38	11.96	0.12
Near Range, centre (Cross Range)	11.59	32	1.36	3.75	0.36
Far Range, right (Range)	18.81	54	2.21	6.33	0.35
Average value	**12.30**	**69**			
Std. Dev	**4.21**	**27.59**			

Table 6.3. Soil Roughness parameters extracted from Laser Ranger and Photogrammetric profiles. Names for laser profiles correspond to the different positions of the field. The orientation of the cut respect to the radar is indicated (in parentheses).

Different values of RMS height and correlation length can be associated to different types of soil tillage. For the test field, the values tend to be associated to a rolled tillage type with a profile length of 1 m [9].

It is important to notice that the values for $\boldsymbol{s}$ and $\boldsymbol{l}$ obtained by photogrammetry are significantly different to the ones from the laser profiler. The photogrammetric process is based on inserting a white board in the field, taking a photo and processing the image. In our case the process underestimates the soil roughness because of a non-perfect insertion of the white board.

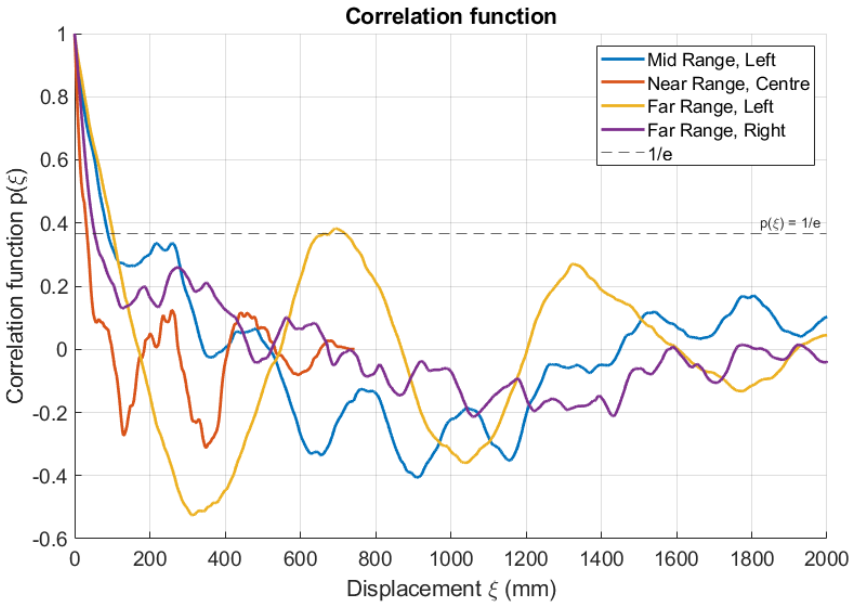

Figure 6.4 Correlation function of the different roughness profiles taken by laser ranger

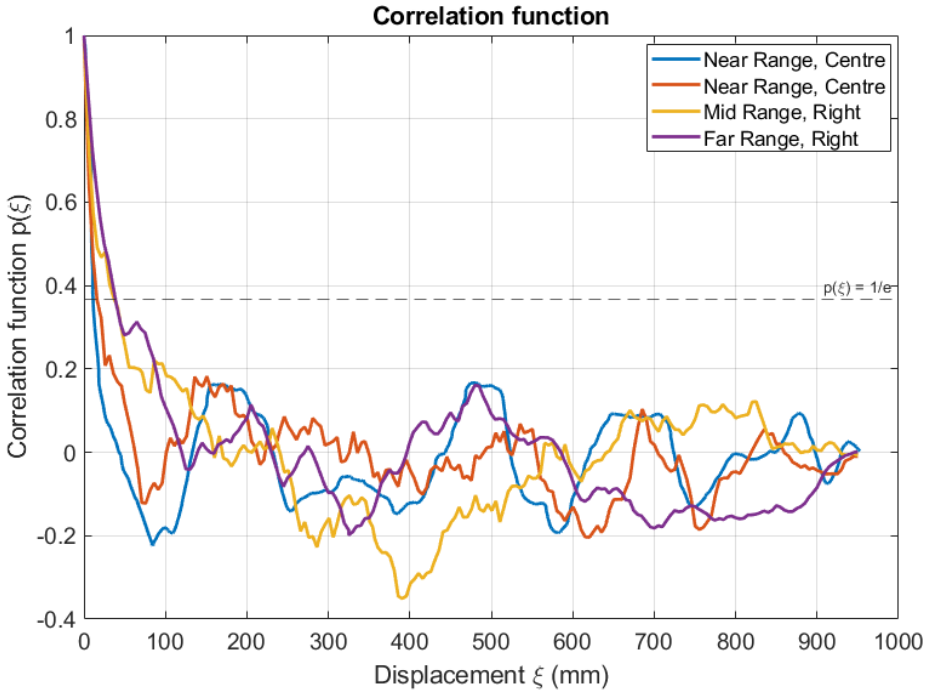

Figure 6.5 Correlation function of the different roughness profiles taken by photogrammetry

6.3.2 Soil moisture

Radar data and ancillary ground-truth synchronised measurements provide the necessary data to assess the radar continuous monitoring of water dynamic processes, such as surface soil moisture evolution especially in the events of rain, run-off, dew and evaporation. The experiment will improve the understanding of the sensitivity of active microwave sensors with respect to soil moisture, particularly the dynamic changes that have been unobservable up to now due to lack of frequent sampling. In the aim of estimating soil moisture from backscatter data [10], a set of Soil Moisture sensors has been deployed as a ground-truth data provider.

The original plan was the installation of two main sets of sensors, placed on each side of the test field, but due to the restrictions imposed by the COVID-19 lockdown the soil moisture during the barley crop campaign has been measured with only a pair of sensors, *Meter Environment ECH$_2$O EC-5* (Figure 6.6, Table 6.4), at a 15cm depth, connected to a Data Logger (Figure 6.7 and Figure 6.8). The data logger included a Temperature/Humidity/Pressure sensor (*Bosch Sensortec* BME280) and a Real Time Clock. Samples were taken every 2 minutes (Figure 6.9).

Figure 6.6 ECH$_2$O EC-5 Volumetric Water Content sensor from METER Group

Figure 6.7 Photographs of the soil moisture and weather parameter Logger installed in Far Range

Despite the topic is out of the expertise area of the research group, few words have to be said about the Soil Moisture sensors, in particular the EC-5. The EC-5 sensor determines volumetric water content (VWC) by measuring the dielectric constant of the media using a capacitance/frequency domain technology. Dielectric sensors do not sense water content directly, they sense the bulk dielectric permittivity of the soil. Two elements are therefore involved in determining accuracy: the accuracy with which the sensor is able to determine the bulk dielectric constant and the accuracy of the relationship between the bulk dielectric constant and soil water content [12].

The soil dielectric permittivity measured by Capacitive Probes (CP), as the EC5 used in the barley campaign, is not only influenced by the water content, but also by other factors, such as soil mineralogy, density, conductivity and temperature. Near the surface, the soil temperature varies significantly over time and therefore can affect the diurnal patterns of CP measurements. In deeper layers, long-term temperature variations lead to an additional trend in the measurements. There is a clear consensus that the temperature has a significant effect on the soil dielectric permittivity. The magnitude of such variations is equivalent to a variation of soil water content that can be greater than 0.04 m^3/m^3, when a standard range of soil temperature variations (10-20 °C) is considered [13]. Tests show the EC5 probes have a maximum temperature sensitivity of ~ 0.003 m^3/m^3 per °C.

Temperature variation during a day cycle could be on the order of 10-20 °C as observed along the corn campaign in summer (Figure 6.10), that implies a daily fluctuation of the Soil Moisture volumetric water content on the order of 3-6% due to temperature dependence.

Volumetric Water content	
Range	0-100 %
Resolution	0.001 m^3/m^3 in mineral soils
Accuracy	± 0.03 m^3/m^3 typical in mineral soils that have solution EC <8 dS/m
Output	
Voltage	10-50 % of excitation voltage (250 – 1.250 mV at 2.500 mV excitation)
Physical dimensions	
Length	8.9 cm
Width	1.8 cm
Height	0.7 cm
Probe length	5 cm
Temperature range	
Min	-40 °C
Max	+60 °C
Connector type	
3.5-mm stereo plug connector or stripped and tinned wires	
Supply voltage (VIN to GND)	
Min	2.5 VDC at 10 mA
Max	3.6 VDC at 10 mA
Measurement duration	
Max	10 ms

Table 6.4 Main specifications of ECH$_2$O EC-5 soil moisture sensor

Figure 6.8 Position of the EC-5 sensors (red circle). Sensors were placed 4 meters from the contour of the field, on the right, in Far Range.

The complete set of soil moisture values from the EC-5 sensors are available in the format of an *Excel* table.

Since 7 May (after the strict lockdown) and until June, gravimetric samples were taken weekly in different areas of the field. Samples were manually taken by means of a T-Style Soil Sampler (Figure 6.11) at different depths, as 0-15 cm and 15-30 cm. Six different positions of the field were selected, three at Near Range (right, centre and left) and other three at Far Range.

EC5 dielectric probes have been a-posteriori calibrated, using gravimetric soil core samples with controlled moisture content at the lab. The samples were taken from the test field and, after drying, water content was progressively increased in several steps until saturation (Figure 6.12). Sensor readings for different soil moisture levels were comparted with manually determined volumetric moisture content. The first soil moisture level is the one associated to dry soil (the soil sample was allowed to air dry for several weeks). The last moisture level should be at or very near at saturation. In this case, the soil saturation is reached at around 40 %.

The increment of moisture level was in steps of between 5-10 %. After pouring the water, the system rested at least for 6 to 8 hours to allow the water to be distributed homogenously, especially in the first measurements. The voltage measured in each step was associated with its corresponding volumetric moisture content. In this way, an accurate relationship between probe measurements and soil moisture from dry stage to saturation has been established. Nonetheless, the EC5 sensor showed changes in voltage according to the soil density, which can induce errors in the calibration process, in particular if it is considered that the soil sample extraction disaggregated and altered the original soil compactness.

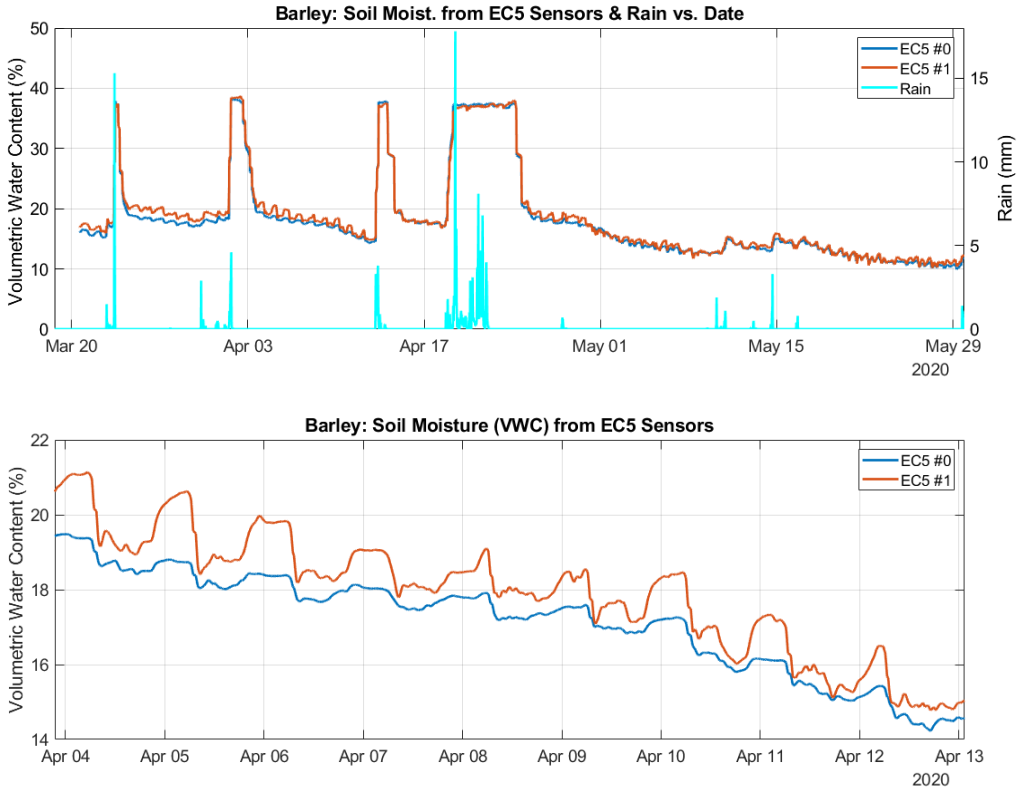

Figure 6.9. (top) Soil Moisture evolution since 20 March 2020, from the two EC5 sensors placed at Far Range. EC-5 daily variation could be seen but it can be associated to temperature dependency. Different Rain events occurred during the period. (Bottom) Zoom of the evolution of the measured VWC for the first weeks of April 2020.

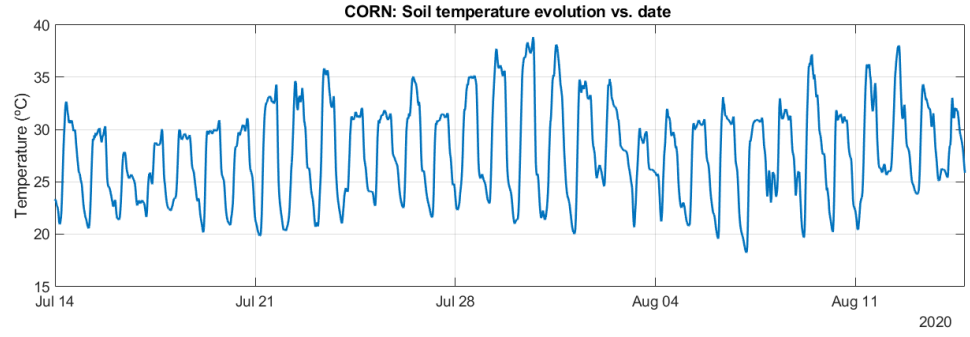

Figure 6.10. Temperature evolution of the soil obtained by a LM35 sensor buried at 5 cm depth for the period from 14 July to 14 August 2020. Bare soil was the dominant at the beginning of the period, while a dense vegetated surface coverage can be assumed at the end.

Figure 6.11 T-Style Samplers used to take samples for Gravimetric Soil Moisture determination

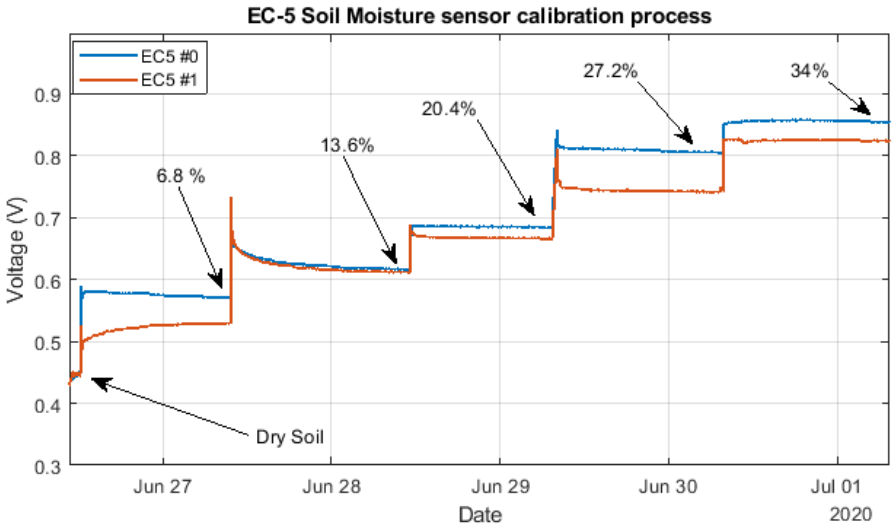

Figure 6.12 Calibration process of the EC-5 sensors. The Soil moisture is progressively increased until reaching the saturation.

6.3.3 Vegetation sampling

The field shows different fertility indexes and soil characteristics, as texture and structure. The different indexes of fertility and soil characteristics are reflected on the vegetation parameter dispersion, as the ones described below.

6.3.3.1 Plant density

Plant Density has been obtained once after crop fully emerged, in fact, it was 60 days after sowing (*Figure 6.13*). For barley, it is estimated to be in the order of 205 plants per square meter using the method proposed in [14]. Due to limitations of COVID-19 outbreak, the measurement was done on 7 May 2020, when the crop was in an advanced stage (34 in the Zadoks-Chang-Konzak growth scale [6]), some elements had tillers that could be confused as main stems.

6.3.3.2 Planting row direction

Planting Row Direction for Barley was forced by the sowing method, and it was parallel to the radar aperture movement (CrossRange)(Figure 6.16).

Figure 6.13 (Left) Zenithal photograph of the field taken on 7 May 2020. (Right) Photograph from the Radar Site, sorghum (light green) is found in between the barley plants (dark green).

6.3.3.3 Biomass & Crop Phenological stage

Due to the reduced dimensions of the radar scenario, special care had to be taken to ensure that the method of biomass measurement did not alter the radar reflectivity.

Vegetation water content (Figure 6.14) and plant phenology staging have been calculated sampling biomass as follows: Four sets, each from an area of 5x5 m^2 of the 4 corners of the field, of 10 randomly selected plants were manually cut at ground level. These four sets were placed in sealed bags and weighted before and after drying. Photographs of some representative plants were taken for phenological stage identification.

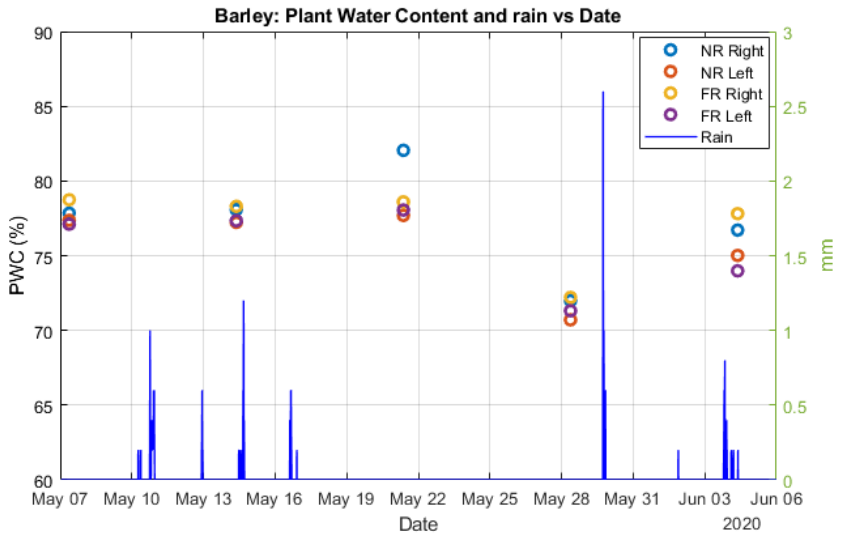

Figure 6.14 Plant Water Content in % (left axis) and rain in mm (right axis) for barley crop

6.3.3.4 Size, height and orientation of main plant elements

Size of main plant elements was obtained at the same time of Biomass and Crop Phenology. The orientation does not make sense in barley crop.

The height has been obtained from six different sectors of the field, three at near range and the other three at far range (right, centre and left). Height in each sector is the mean value of the distance from the ground to the node of flag leaf for, at least, 10 randomly selected main stems. (Figure 6.15).

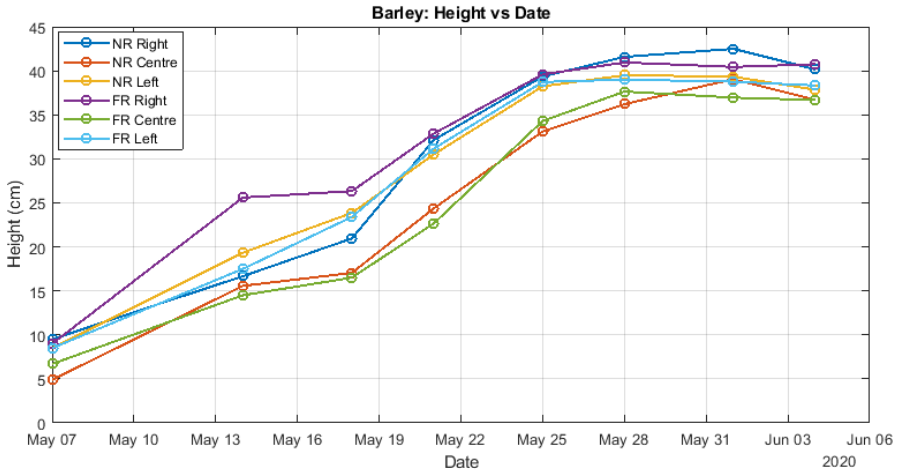

Figure 6.15 Crop height evolution since 7 May 2020.

Figure 6.16 Photographs showing row direction and density of Barley crop. Sowing of HYDROSOIL test field on 4 March 2020 (top), early stage of growth on 20 March (middle) and advanced growth stage on 28 May (bottom).

6.3.3.5 Leaf Area Index (LAI) determination

The method to measure the Leaf Area Index (LAI) is based in cutting different plants, scanning the leaves and calculating the area by image processing (Figure 6.17). The cutting strategy ensured that the plant density was not significantly affected in order to maintain the radar reflectivity. Three plants were cut from the six sectors of the field, three sectors at near range and the other three at far range (right, centre and left). This strategy for taking samples from these six sectors was induced by the fact that different growths were observed depending on the location in the field. The total leaf surface was calculated by means of the *ImageJ* open-source software [19]. The mean value for each sector is calculated and the LAI index is extrapolated considering the plant density (Figure 6.18). It is important to notice the difficulty to determine the LAI index manually, it is easy to be confused cutting different main stems from different plants assuming that they are tillers (Figure 6.13). In fact, some LAI calculations have to be rejected as an error in the execution of the measurement has been detected. Another aspect to consider is the effect of other plants in the LAI calculation and its relation with the reflectivity. At the end of the barley campaign, sorghum plants rapidly grew in the field and were not included in the LAI calculations.

Figure 6.17 Example of scanned image of the leaves before image processing by means of ImageJ software. Notice that parts of the leaves are affected by Puccinia Hordei disease

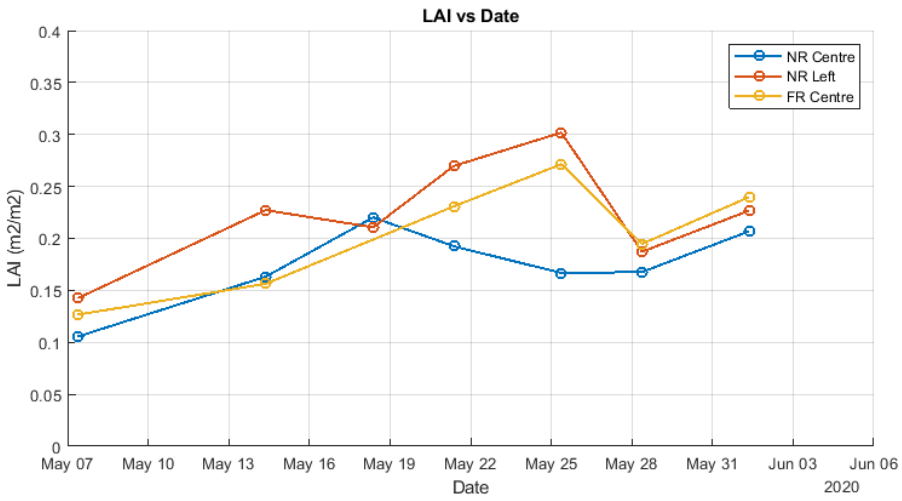

Figure 6.18 Leaf Area Index for barley crop for different sectors of the field. Only three of them are shown.

6.3.3.6 Interception of precipitation

This measurement has been done only for corn crop. For barley, the plant density was light enough to assume the rain interception was negligible (Figure 6.13).

6.3.4 Meteorological parameters

A DAVIS Vantage Pro 2 Fan Aspired local Weather Station, shown in Figure 6.19, has been installed at a 25 m distance from the field under test, at the same elevation as shown in Figure 6.20. The station has been logging the main meteorological parameters since 7 May 2020 every 10 min: air temperature, barometric pressure, air humidity, wind speed, gust and direction, rain precipitation and solar and UV radiation and derived products. The complete set of parameters has been periodically downloaded and their complete series are available as an *Excel* table. Figure 6.21 shows a sample plot of some meteorological parameters acquired in 3 days.

Figure 6.19 Davis Vantage Pro 2 Fan Aspired Weather Station

Parameter	Resolution	Range	Accuracy
Barometric Pressure	0.1 hPa	540 to 1100 hPa	1 hPa
Humidity	1%	1% to 100%	3%
Dew Point	1°C	-76°C to +54°C	1.5°C
Rainfall	0.2 mm	0 to 6553 mm	3%
Rainfall rate	0.1 mm/hr	0 to 1016 mm/hr	5% <= 250 mm/hr
Solar radiation	1W/m2	0 to 1800 W/m2	5%
UV Dose	0.1 MED	0 to 199 MED	5%
Temperature	0.1 °C	-40°C to +65°C	0.5°C
Wind speed	0.1 m/s	1 to 80 m/s	5%
Wind direction	22.5°	16 compass pts.	3°

Table 6.5 Main specifications of Davis Vantage Pro 2 Fan Aspired Weather Station

Figure 6.20 A local Weather Station (DAVIS Vantage Pro 2) was installed next to the test field

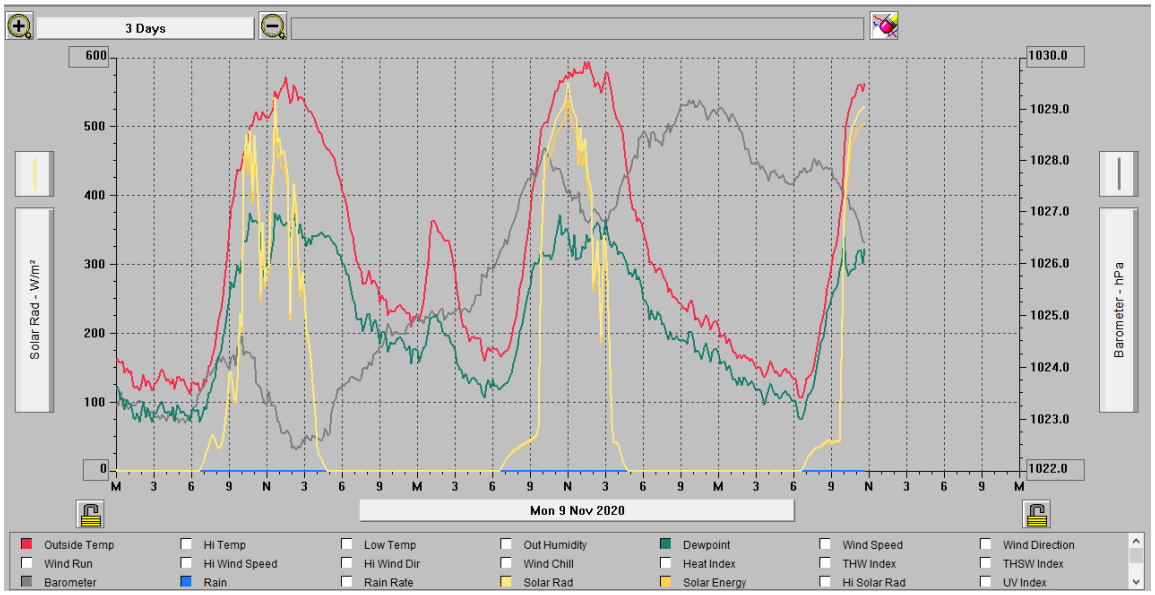

Figure 6.21 Plot of some meteorological parameters acquired between 9 and 11 November 2020 with the local Weather Station (DAVIS Vantage Pro 2). Red: Temperature in °C, Yellow: Solar radiation in W/m², Blue: Rain in mm, Grey: Pressure in hPa, Green: Dew Point in °C.

From the beginning to the end of the barley campaign, atmospheric parameters were also gathered from a weather station in Viladecans (Barcelona) of the Servei Meteorològic de Catalunya (https://www.meteo.cat/observacions/xema/dades), 8 km far from the test field.

6.4 Results

6.4.1 Backscattering evolution of barley

In this point, the long-term backscattering evolution of barley crop will be presented and related to most relevant changes.

Figure 6.22 shows the HH & VV backscattering magnitude of barley crop in the whole plant life cycle, from beginning of March after sowing, until June when barley was harvested. Ancillary data is also shown, including Plant Water Content, Soil Moisture, Plant Height and cumulated Rain every 30 minutes in millimetres.

The crop growth is slow in March to April, in this period the backscattering shows fast increases resulting from rain showers and gradual loss of backscattering in the subsequent drying process in the following days. There is an important exception in this trend around 19-23 April, when strong cumulative rain fell, resulting in a water soil saturation and formation of large water puddles on the field. As water puddles are almost specular surfaces, this results in a large forward scattering and low backscattering until the surface water is absorbed/evaporated. This backscattering loss is particularly important in HH polarization in the Near Range part of the field and slight or non-existing in Mid or Far Range as shown in Figure 6.23 In addition, a 1 to 2 dB daily ripple can be observed which is associated to dew water condensation and evaporation afterwards on both soil surface and plants. A small downtrend of backscattering in this period can be associated to loss of soil roughness due to rain events.

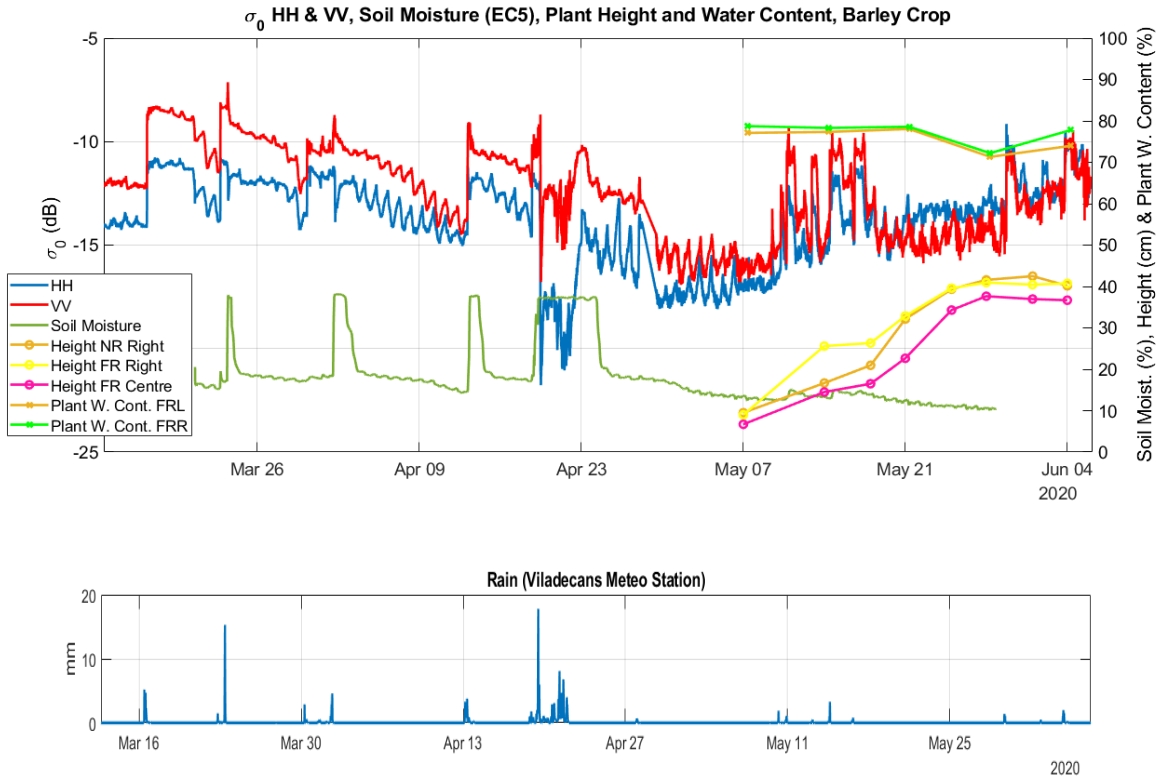

Figure 6.22 (Top) Time series of backscattering coefficient (σ^0) of barley crop at VV and HH channels for Near Range incidence angles from 55.2° to 59.1°, including Crop Height in Near and Far Range Left and Right sides, Plant Water Content at Far Range Left and Right sides of the field, Soil Moisture measured with EC5 Probe. (Bottom) Precipitation measurements from Viladecans nearby official Meteorological Station.

From May the plants contribution to backscattering becomes relevant resulting in a slow σ^0 increase in both polarisations until harvest time in June. The sudden increase in rain shower events and daily cycle is still present in this period. Also, the approximate 2 dB of co-polar σ_{VV}/σ_{HH} difference observed on bare-soil at the acquisition beginning is reduced with the larger crop growth in early May and even inverted in mid-end of May with higher HH return. These analyses will be further expanded in the following document sections.

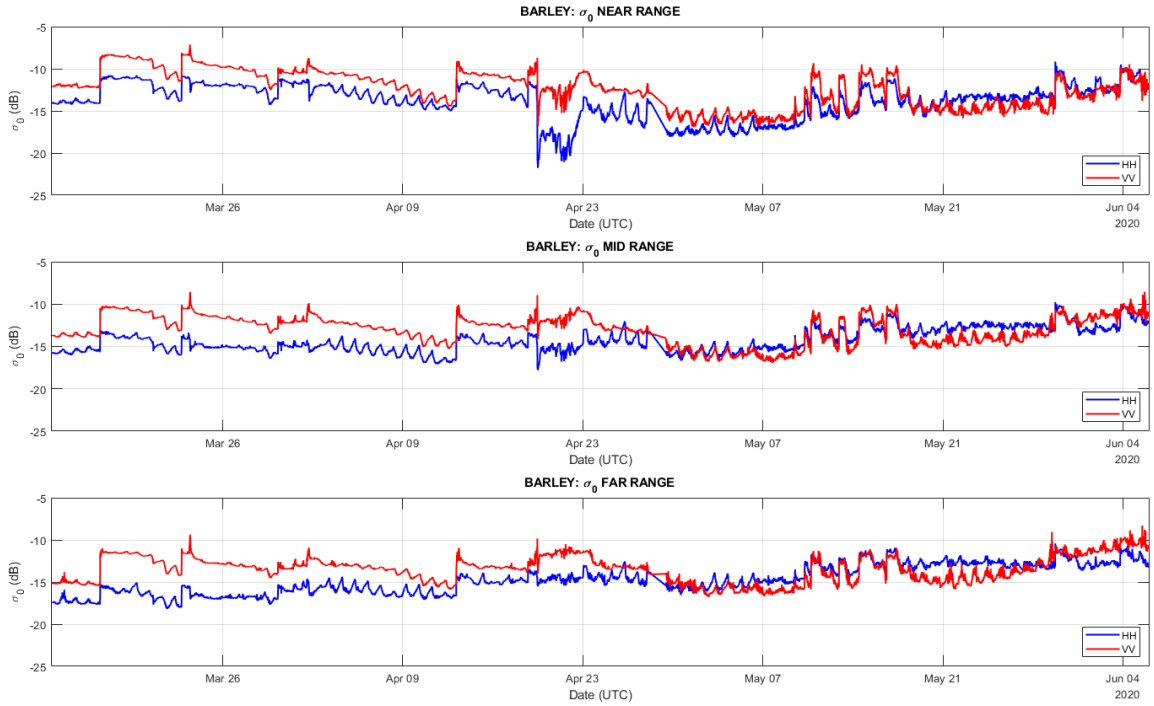

Figure 6.23 Time series of calibrated backscattering coefficient (σ_0) of barley crop at VV and HH channels for (Top) Near Range incidence angles from 55.2° to 59.1°, (Center) Mid Range incidence angles 59.1° to 63° and (Bottom) Far Range incidence angles from 63° to 66.9°.

6.4.2 Impact of Rain and Soil Moisture on Backscattering

In addition to the general evolution of backscattering presented in the previous section, more detailed observations will be outlined, related to rain and irrigation events affecting soil moisture and measured radar backscattering. From Figure 6.24, that shows the backscattering evolution of the whole barley campaign, together with Soil Moisture and Rain Intensity measurements, several significant Rain episodes will be zoomed in and interpreted.

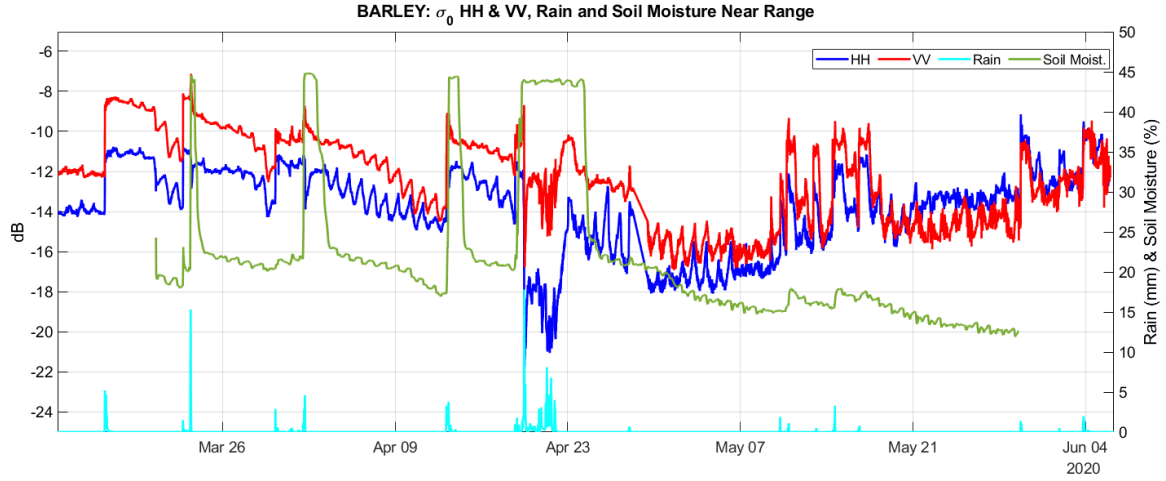

Figure 6.24 Barley campaign: complete time series of backscattering coefficient σ^0 at VV and HH channels for Near Range incidence angles from 55.2° to 59.1°.

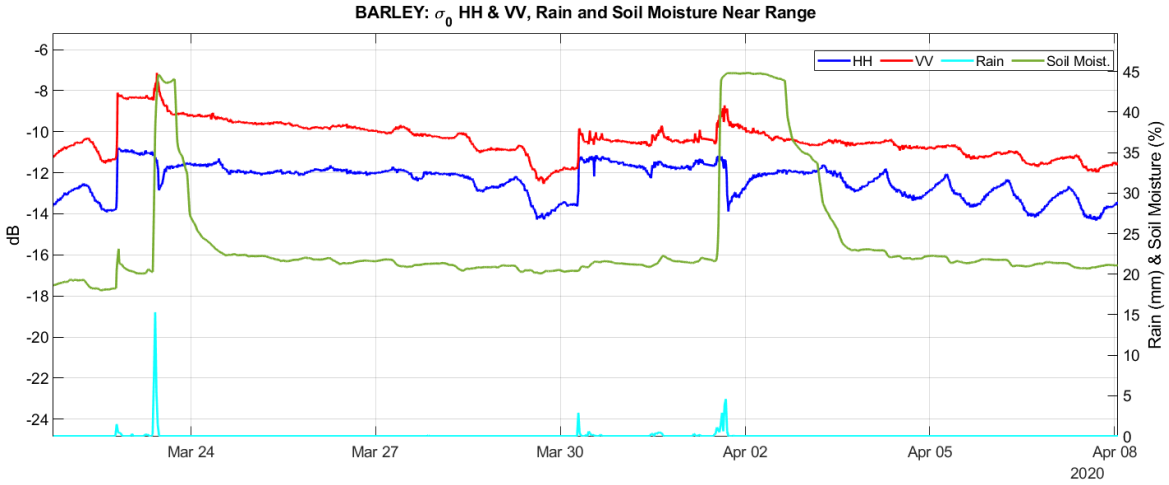

Figure 6.25 Detail of barley Near-Range backscattering at late March – early April.

Figure 6.25 shows the impact of rain showers with positive and negative backscattering changes depending on the background soil moisture of the field and polarisation. For example, on 22 March, a light rain shower increased slightly the soil moisture resulting in a +3 dB increase of backscattering in both co-polar channels HH and VV. However, an additional moderated shower of 15 mm fell next day (23 March), resulting in a large soil moisture increase with a positive +0.4 dB backscattering increase in VV, but a backscattering loss around 1 dB in HH polarisation. As both changes receded rapidly after the rain was over, they could be related to the formation of water puddles which have been observed sometimes in the field after intense rain. On 30 March and 1 April a similar situation occurs. From 4 to 8 April a typical diurnal backscattering cycle can be observed that will be discussed in Section 6.4.3. Figure 6.26 shows a photo of the barley field showing the small size of the barley plants on 20 March.

Figure 6.26 Barley crop photograph taken on 20 March.

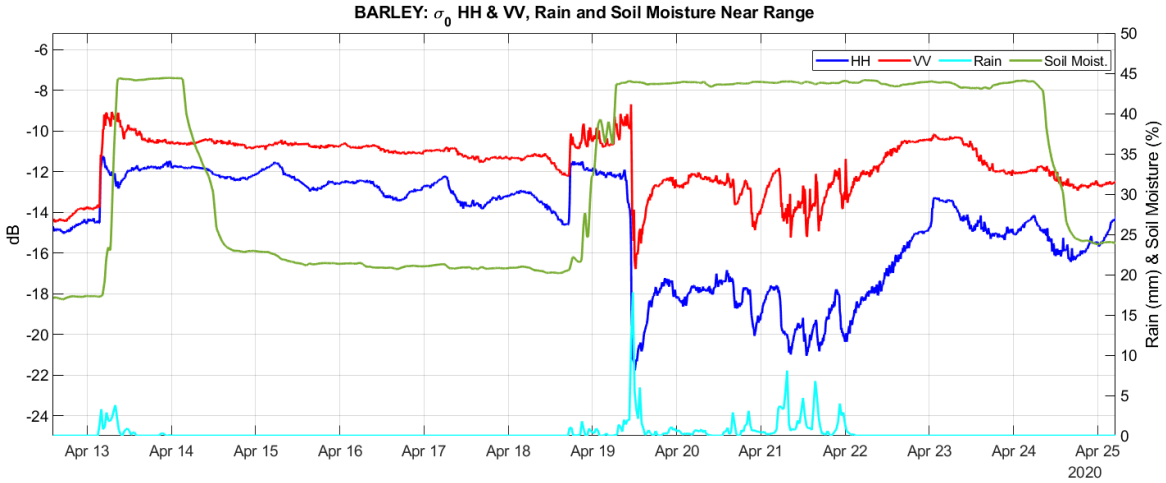

Figure 6.27 Detail of barley Near-Range backscattering in the strong rain showers of 18-21 April resulting in the field flooded.

Figure 6.28 Water puddles on barley field after the intense rain recurrent precipitation of 18-21 April (Photo taken on 24 April).

In April, a succession of rain showers ended up severely flooding the agricultural test fields of the EEABB, including the barley field under study which negatively impacted the crop evolution. In this case, in the near-range of the field both polarisations increased in the first showers but once the soil was saturated, σ^0 decreased suddenly 10 dB in HH and 6 dB in VV with additional precipitation. For higher incidence angles (see Figure 6.23), the backscattering drop after soil saturation was barely observable probably because the flooding was less severe.

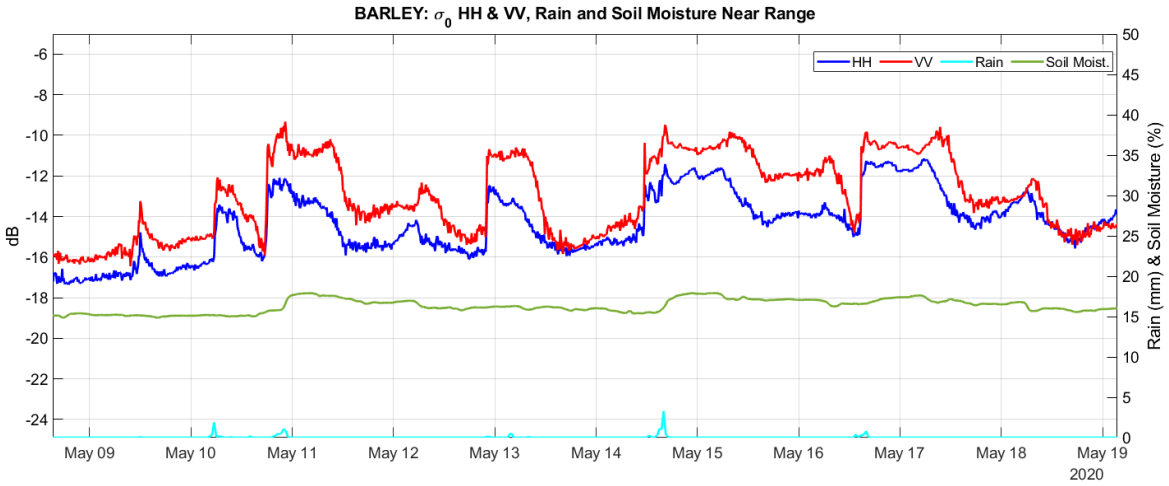

Figure 6.29 Detail of barley Near-Range backscattering changes induced by light rain showers of mid May

Mid May rain showers were much lighter, barley height at this time was 25 - 30 cm and growing fast, consequently the field soil moisture increased after precipitation but well below the saturation point. In these conditions, the field backscattering was extremely sensitive to rain and subsequent soil moisture increase as evidenced by the strong correlation between σ^0 and soil moisture measurements. Radar backscattering proved to be more sensitive than pluviometers as shown by the backscattering peaks measured on 9 and 12 May. In some cases, VV changes appear slightly delayed compared to HH, this delay could be explained by different rates of water interception and evaporation of stem and leaves.

Figure 6.30 Barley crop photographed on 14 May. Some yellowed leaves can be seen as they were affected by Puccinia Hordei disease.

6.4.3 Backscattering diurnal cycle

A few dB diurnal backscattering cycle has been consistently observed in barley campaign. The amplitude of the measured diurnal fluctuation is well above the present radar calibration precision estimated in the order of 0.4 dB (Section 8). Along the field visits and sampling activities it was evident the wet condition of both soil and vegetation in the first hours of the morning and progressive water evaporation between around noon and afternoon hours of a typical day, depending of course on the season and meteorological conditions of sun irradiation and air humidity. Accordingly, these diurnal cyclic changes were interpreted as dew impacts on soil and crop backscattering increasing in the early morning and decreasing in noon-afternoon hours (Figure 6.31).

Figure 6.31 Close view of dew water-condensation on soil and vegetation in HydroSoil field at 7:00 am. Photo taken on 19 February 2021.

The contribution of dew to backscattering changes is recognised by Long and Ulaby [21] which states that the presence of water on cereal crops leaves can increase VV polarisation backscattering at 10 GHz up to 3 dB, although the variation with frequency, angle and polarization has not yet been stablished. A study by Riedel et al. [26] have reported evidences of dew impacts showing both positive and negative changes of C-Band backscattering acquired with DLR's E-SAR system on barley and corn fields. The TerraDew Research Project [27] reported a typical radar backscattering increase of 1 to 4 dB in wet conditions induced by dew but the underlying mechanisms are still poorly understood and inconsistences can be observed among different published results with positive and negative impacts of dew on measured backscattering. One of the main problems is the lack of systematic data due to revisit time and calibration limitations of airborne and spaceborne sensors. HydroSoil is an excellent source of experimental data to improve the understanding of dew influence on SAR images and derived products, with the potential to improve exploitation of active and also passive microwave sensors since the involved scattering, absorption and extinction phenomena affect both techniques. Only initial inspection of data and preliminary interpretation has been done so far, which will be followed by more in-depth analysis. A strong correlation or influence has been observed with air humidity which has been included in the detailed plots.

Figure 6.24 shows the complete barley campaign backscattering, soil moisture and rain intensity that will be used as reference.

To minimize rain influence, 3 dry periods (2-13 April, 30 April – 10 May, 21-29 May) have been selected adding Air Humidity data in the plots of Figure 6.33 to analyse diurnal cycles in barley crop. In the early stage of barley (2 – 13 April) we can consider that the radar is observing a large fraction of bare soil and there is a very strong correlation between measured radar backscattering and air humidity changes. The HH and VV backscattering levels seems to slowly integrate the humidity level that increases rapidly after midnight. The measured air humidity decays abruptly after sunrise time, which is also reflected by a similar abrupt decrease in radar backscattering. HH change (1.25 to 1.5 dB peak to peak) is slightly higher than VV (0.6 to 1.4 dB).

In the second selected period (30 April – 10 May) the crop biomass is still small and the backscattering behaves similarly as in the bare-soil case. The diurnal cycle peak to peak oscillations up to 2.5 dB in HH and 2 dB in VV can be observed.

It is interesting to highlight a substantial delay between HH channel, that in most cases is well synchronised with air humidity changes and VV polarisation that follows a similar trend but 30' up to 2 hours later, possibly reflecting differences in water dynamics on soil, leaves and stems. The diurnal cycle is hardly observable in the 6 - 9 May interval because of a wind increase episode (from the usual light 1-2 m/s, a moderate breeze of 4-5 m/s was measured). The breeze causes vegetation random motion, resulting in the observed backscattering fast fluctuations, which in combination with lower humidity levels reduced water condensation.

The plot corresponding to the end of May in Figure 6.23, with the crop in mature stage and higher biomass (Figure 6.32) shows a differentiated behaviour with respect the previous low-density stages.

In May 21-24 the VV and HH backscattering changes are almost opposite each other, with HH increasing with air humidity and VV decreasing. From May 25 both VV and HH backscattering evolve again in phase but opposite phase with respect to air humidity. This plot is difficult to interpret due to strong winds blowing the whole week, especially around noon, with measured peak gusts up to 8 m/s.

Figure 6.32 Barley crop on 28 May.

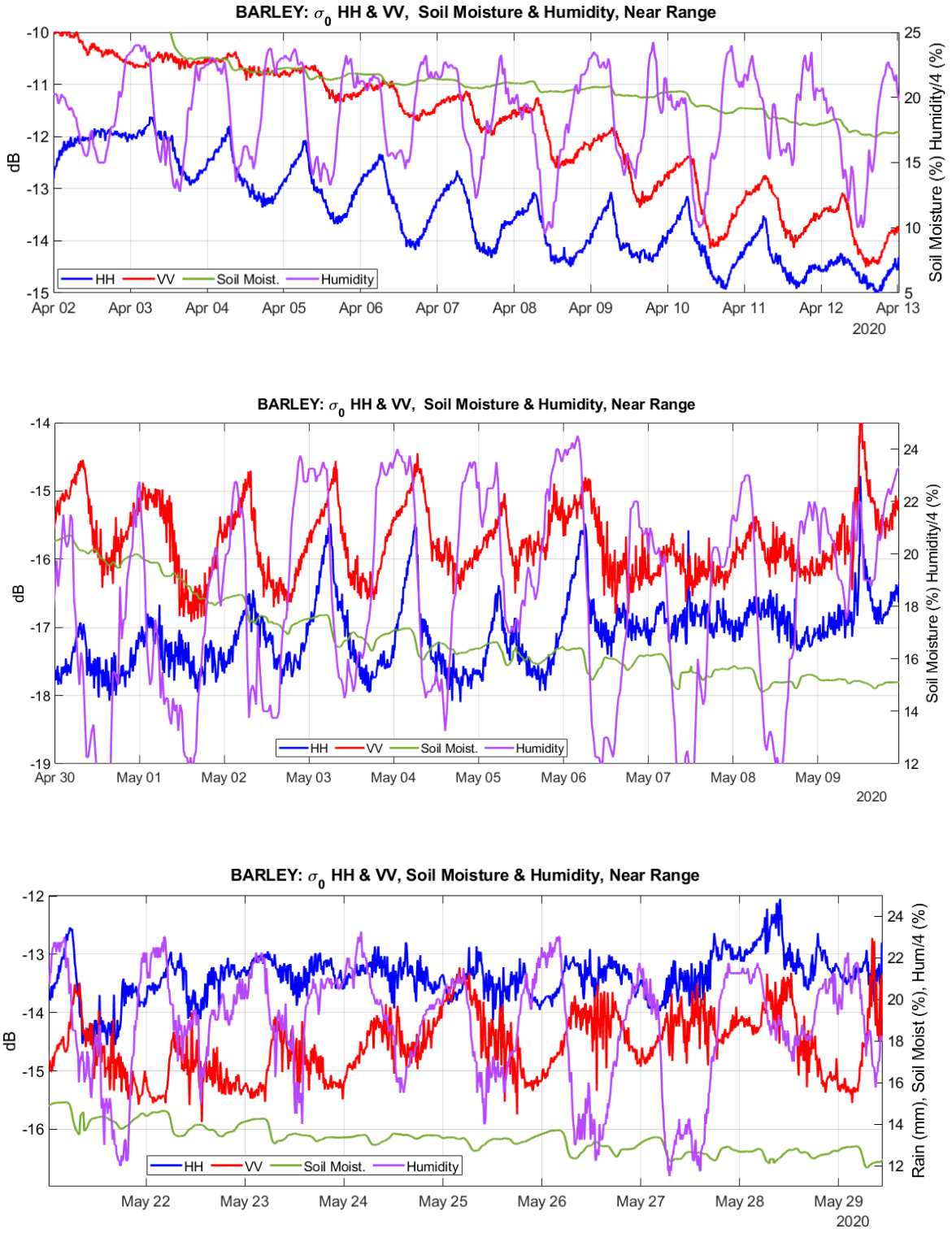

Figure 6.33 Time series of barley Near-Range backscattering coefficient σ^0 , Soil Moisture, Air Humidity in 3 selected periods: 2-13 April (top), 30 April – 10 May (middle), 21-29 May (bottom).

6.4.4 Impact of the diurnal plant water content cycle on radar backscattering

The assessment of the ability of radar backscattering data to observe crop physiology (movement of water, controlled by vegetation, in the soil and plant during the day) is based on a single day campaign, 28 May 2020. In this day, fresh and dry biomass destructive measurements were carried out every 2 hours during 12 h, from 06:00 to 18:00 UTC (8:00 to 20:00 local time). In parallel, radar, weather and soil moisture measurements were taken. Different plants were cut and segmented to extract the Plant Water Content evolution of these segments during the day (Figure 6.34). Slight changes in Plant water content (PWC) are seen for the barley crop. First segments, the ones close to the ground, show a higher water content compared with the rest. The PWC of the segments show a monotonic decay.

Backscattering coefficient (σ^0) of the different polarimetric channels for three different areas of the field (near, mid and far range) is evaluated (from Figure 6.35 to Figure 6.37). It has to be noted that for barley the backscatter is assumed to be dominated by ground, attenuated by the vegetation because of the low density of the crop, so an important contribution of the soil in the radar response is expected. Co-polar response in barley is not showing a clear relation with the PWC evolution.

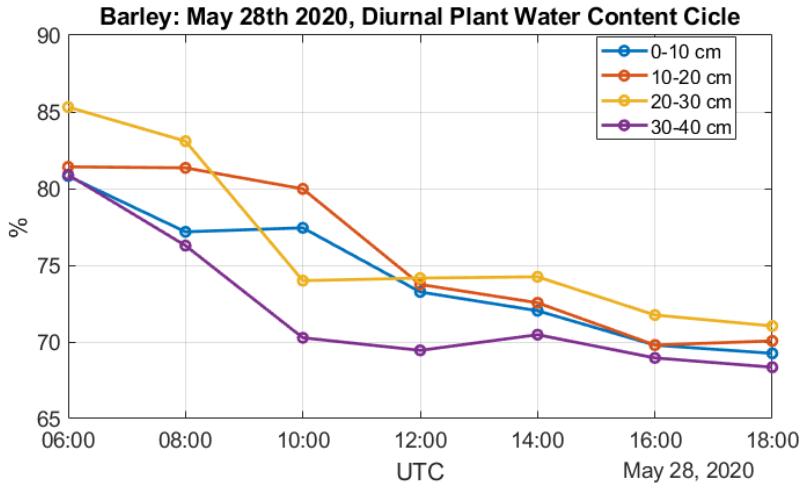

Figure 6.34 Time series of plant water content for four different segments of the plant.

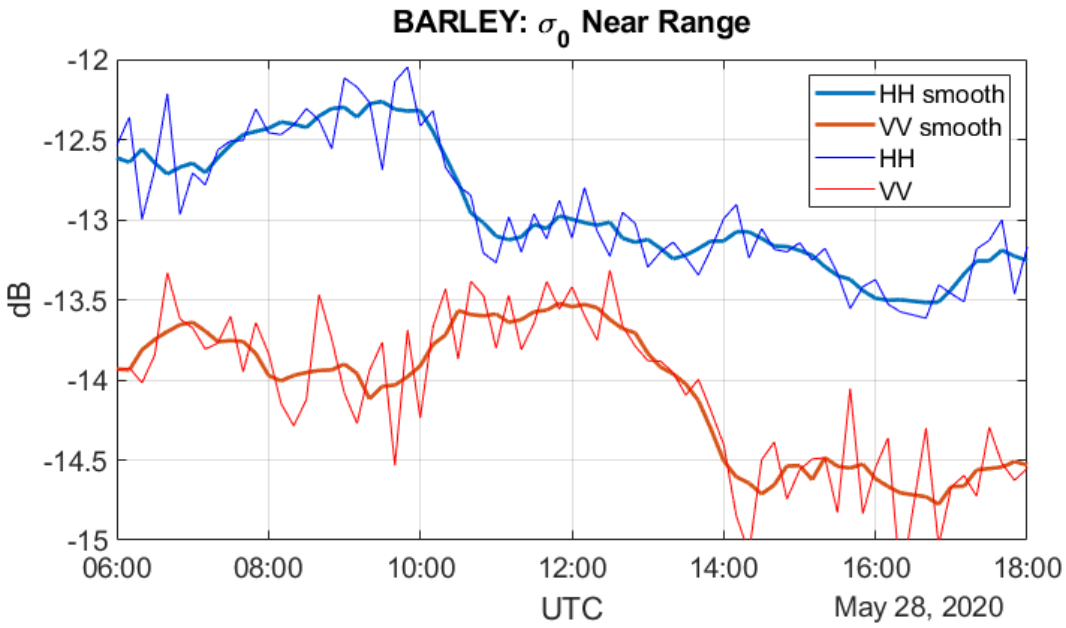

Figure 6.35 Time series of backscattering coefficient of the Co-polar Channels for Near Range.

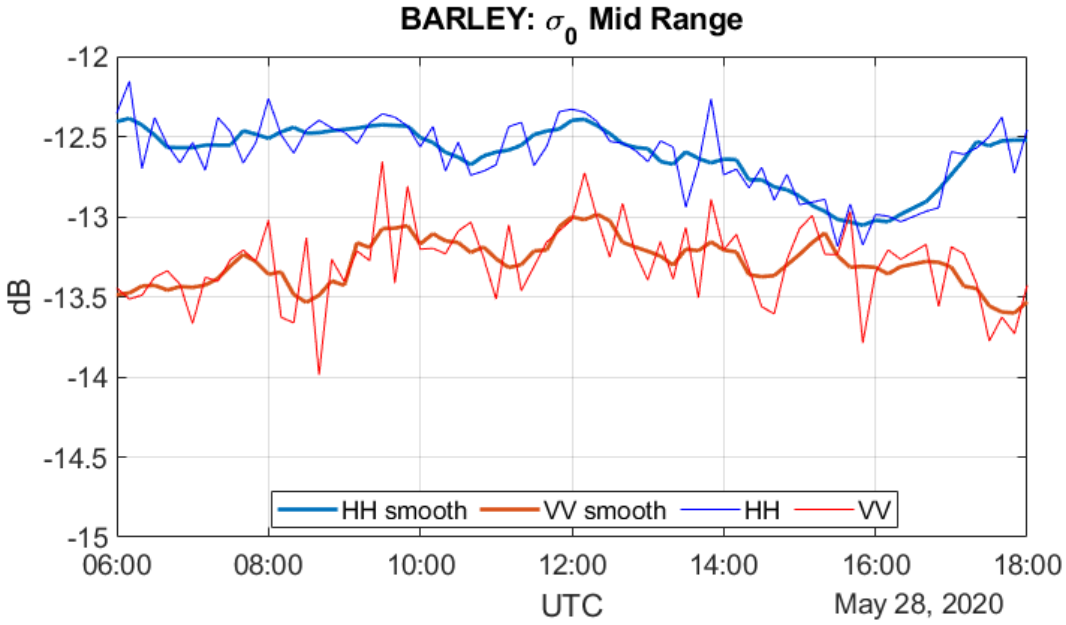

Figure 6.36 Time series of backscattering coefficient of the Co-polar Channels for Mid Range.

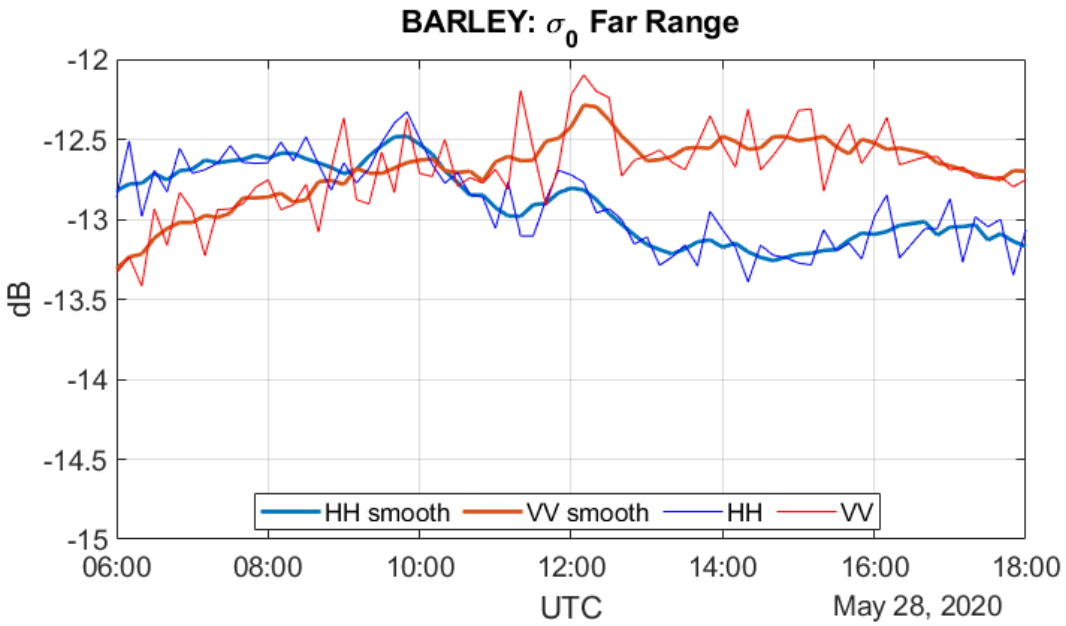

Figure 6.37 Time series of backscattering coefficient of the Co-polar Channels for Far Range.

6.4.5 HH-VV decorrelation with surface parameters

The normalized complex correlation between S_{hh} and S_{vv} is defined as

$$\rho_{hhvv} = \frac{\langle S_{hh} S_{vv}^{*} \rangle}{\sqrt{\langle |S_{hh}{}^{2}| \rangle} \sqrt{\langle |S_{vv}{}^{2}| \rangle}} \tag{6.1}$$

Where the mean value operator <·> is obtained by a spatial average (multilook) with samples with a similar incidence angle and $|\rho_{hhvv}|$ is between 0 and 1. The correlation between hh and vv: $|\rho_{hhvv}|$ is a good parameter to discriminate between absence and presence of vegetation. When surface scattering dominates, correlation between the two co-polar channels is high. As soon as the plants emerge, a decorrelation of the co-polar components appears caused by differential extinction, since the VV channel is more affected by attenuation than the HH channel. The last stages of vegetation growth are associated with a predominance of random volume (RV) scattering, expecting only a small correlation between the co-polar channels in this type of dispersion (theoretically $|\rho_{hhvv}| \approx 1/3$) [22]. The behaviour described above is evident in both the barley campaign and the corn campaign. The problem will be analysed at mid range (incidence angles from 59.1° to 63°), but the result would be equivalent for near and far range.

Figure 6.38 shows the time series of hh-vv correlation of the whole barley crop campaign including rain intensity and crop height evolution. Vegetation begins to emerge in the barley field around March 20 (Figure 6.26) and this is evidenced by a loss of correlation in the graph. Rain also produces co-polar decorrelation. The structure of the terrain facilitates the formation of water puddles in intense rainy events as can be seen in the Figure 6.28 on 24 of April. This will lead to a significant loss of correlation of the co-polar components on this date. It can be observed that for small values in the height of the vegetation there is already an important co-polar decorrelation that remains

constant with the growth of the plant.

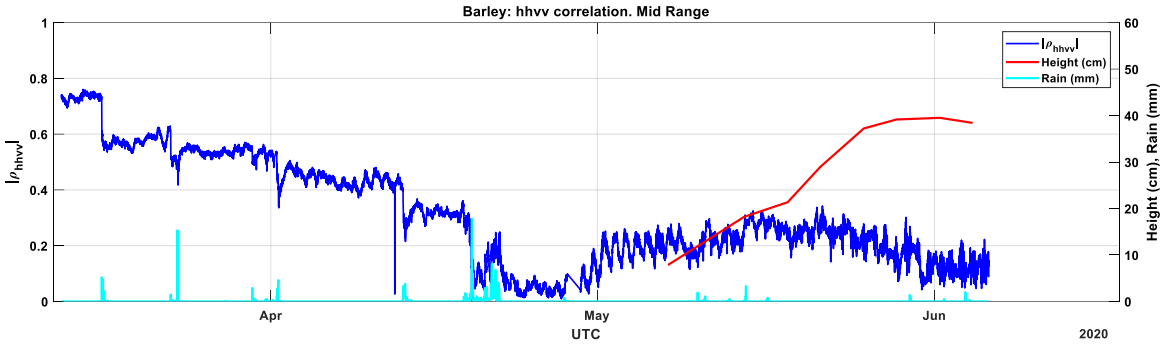

Figure 6.38 Time series of hh-vv correlation of barley crop for Mid Range: incidence angles (59.1 ° to 63 °) including rain intensity (cyan) and crop height evolution (red).

6.4.6 Phase & Coherence changes

The coherence between two SAR images is an excellent quantitative change indicator. In order to compute the coherence, a spatial average of N pixels is used,

$$\hat{\gamma} = \frac{\sum_{i=1}^{N} u_i^{SLAVE} \cdot \left(u_i^{MASTER}\right)^*}{\sqrt{\sum_{i=1}^{N} \left|u_i^{SLAVE}\right|^2} \cdot \sqrt{\sum_{i=1}^{N} \left|u_i^{MASTER}\right|^2}} \tag{6.2}$$

The coherence is computed between a master image which is used as reference and a second slave image where the changes are to be identified. Since coherence is defined as a normalised parameter, the possible magnitude values range from 0 (total decorrelation) to 1 (no changes). Since coherence is a complex parameter the phase provides a magnitude weighted average phase change information in the considered area.

In this specific study, the mid-range area has been selected as the averaging window used to compute the coherence, because the good compromise of this region between its number of samples and the incidence angle.

Two different types of processing have been implemented to obtain the mid-term and short-term evolution of coherence:

a. Taking the first radar image of the time interval as the master. The rest of images are considered different slaves, and their corresponding coherence is computed with respect to this unique master image. A mid-term one-week evolution of coherence has been obtained in this way for different crop stages.

b. Changing the master image every 24h, means that for a one-day cycle the same master is used and the next day the master image is reset to the 00:00 (UTC) value. Therefore, the slave images are used to evaluate the short-term 24 h coherence with respect 00:00 (UTC) of the same day.

The crop height is a characteristic of the agricultural field that can influence the results of our measurements. As coherence is used to detect changes, these two aspects could be related.

To study the crop height's influence over the coherence, three different time periods for each crop-type, with different growing-stages, have been selected:

- 23 March 2020 – 29 March 2020. Plant height ~5 cm, corresponding to an initial stage
- 8 May 2020 – 14 May 2020. Plant height ~20 cm, being a mid-stage of growth
- 22 May 2020 – 28 May 2020. Plant height ~40 cm, in this period the plants achieved the maximum height and the grain developed

Furthermore, these time-intervals have been selected avoiding rain events, to avoid rain alterations on coherence.

6.4.6.1 Short term and long-term coherence evolution. Impact of crop height

From Figure 6.39 to Figure 6.44 , the magnitude of the coherence is represented for the different time intervals selected to study. For each time period, this magnitude has been computed for the two methods of master image selection. As expected, depending on the crop growth stage, the coherence decay slope changes, affected by diurnal cycles and rain events.

A clear relation between crop height and coherence decay can be observed looking at the figures, specially focusing on the cases where only one master image is used as shown in Figure 6.39, Figure 6.41, and rest of odd numbers up to Figure 6.44.

In order to better observe the diurnal cycle with fast decorrelation crop stages, the short term coherence figures, with a 24 h master reset are more suitable: Figure 6.40, Figure 6.42 and Figure 6.44.

For the barley campaign (Figure 6.39 to Figure 6.44), some differences between the coherence evolution of the three proposed time-intervals can be observed. At the beginning of the campaign, when the plant has its shortest height, notwithstanding the fact that on 23 March, between 9:00 h and 11:30 h (UTC), there is a noticeable decay of the coherence due to a rain event. For the rest of the interval the coherence is very stable along the whole week, ending with a good coherence value at the end of the interval. In other words, at this initial-stage, the field is still coherent after one week.

When barley has achieved a height of approximately 20 cm, on the second week of May, the coherence is not maintained as stable as in the previous case, showing lower coherence values at the end of the week. Nevertheless, there is not a strong decay and at the end of this interval, the coherence value is still good enough to be considered a coherent scenario. The abrupt coherence losses are caused by frequent rain showers (Figure 6.29).

In the last barley mature stage interval, with a plant height ~40 cm, it can be observed that the coherence magnitude value decays faster along the observed week. In this case, some differences can be observed between the different polarizations: In HH polarization after 7 days presents an acceptable coherence value. The VV polarization, with a stronger contribution of the crop compared to HH, shows a much lower value, which combined with wind induced motion resulted in remarkable coherence losses for this polarization.

An aspect that all these three intervals have in common is that even there are no strong decays of coherence, the value decreases progressively, and how much it does decrease depends on the plant height in combination with daily wind.

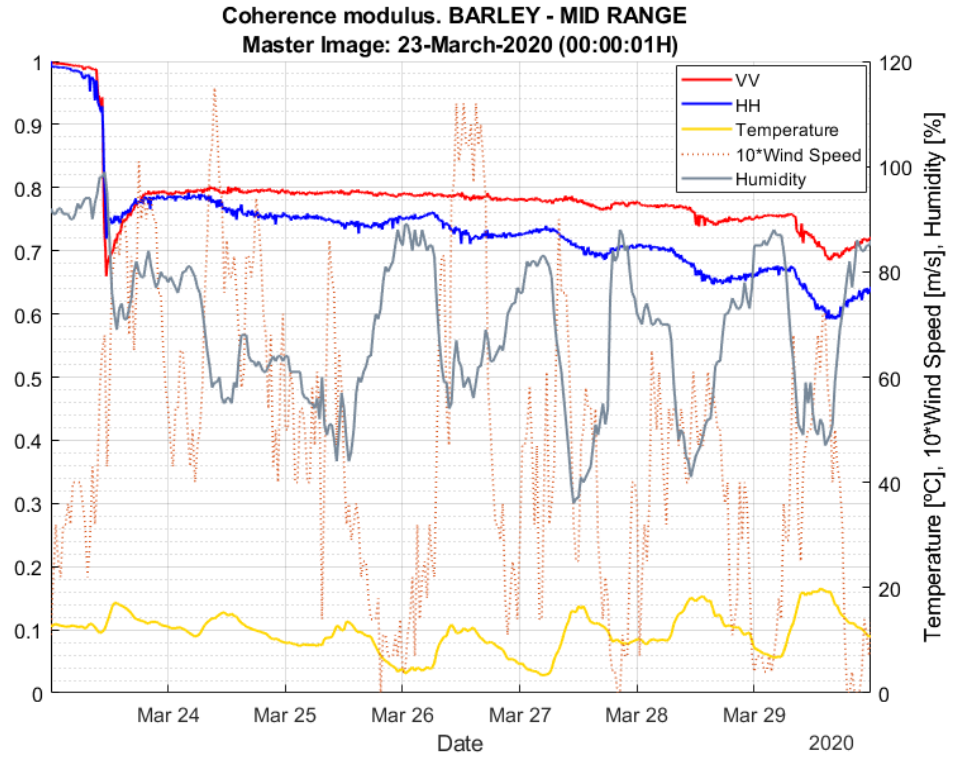

Figure 6.39 Modulus of the coherence. Barley campaign, plant height ~5 cm. Only 1 master image used. The wind speed has been multiplied by a factor of 10 in order to adjust its dynamic range to the right-side vertical axis values.

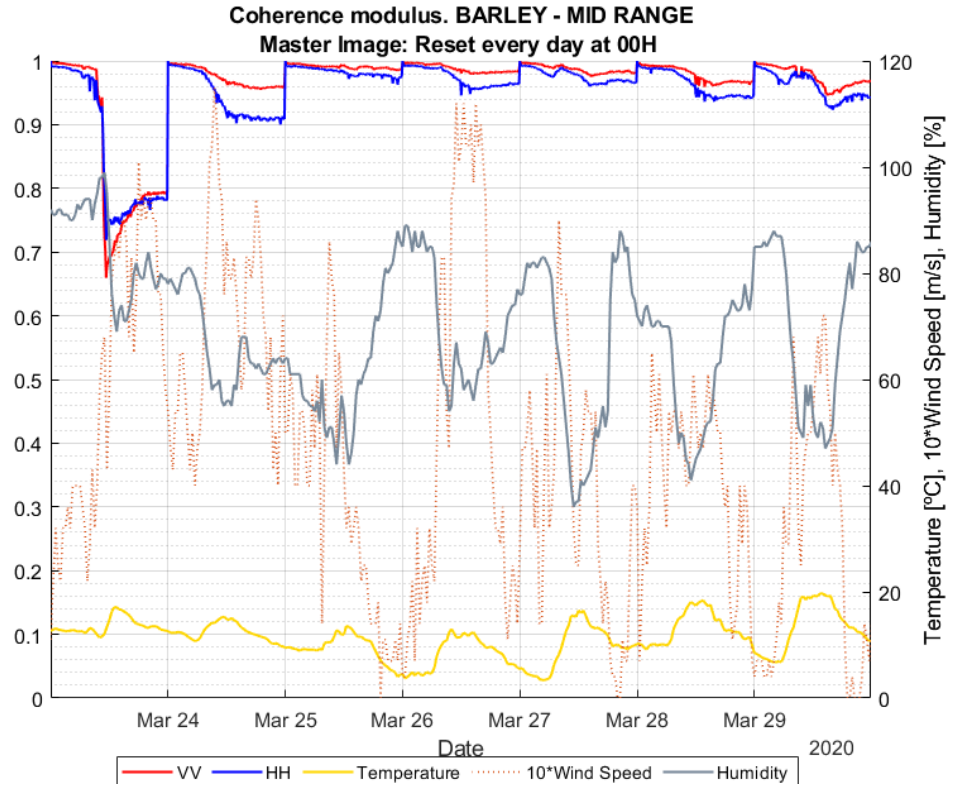

Figure 6.40 Modulus of the coherence. Barley campaign, plant height ~5 cm. Master image reset every 24 h.

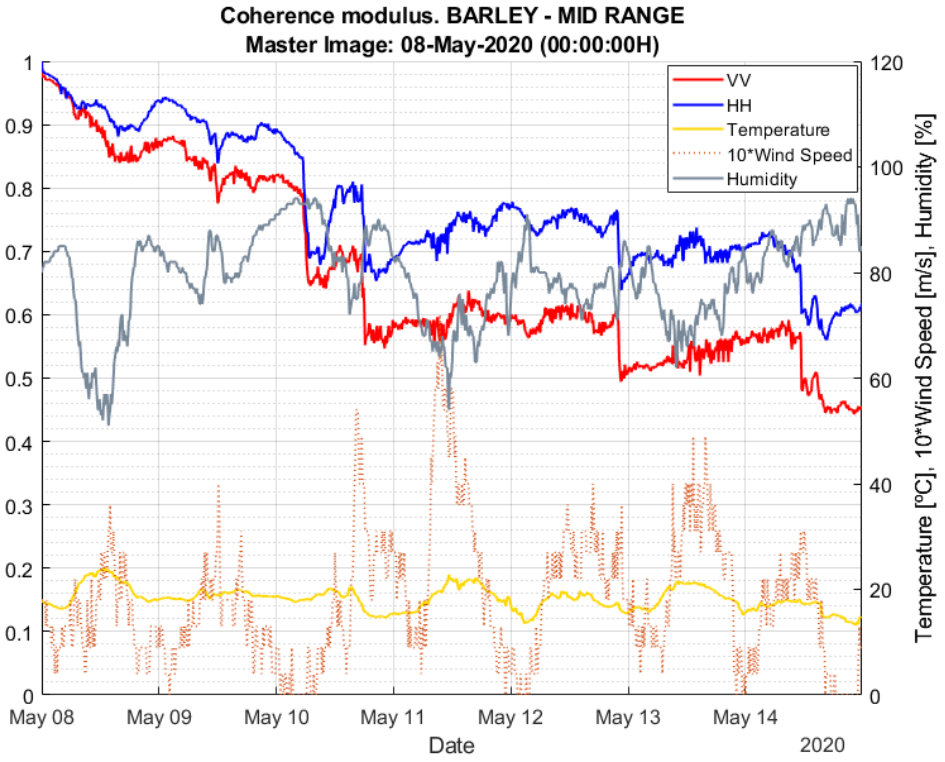

Figure 6.41 Modulus of the coherence. Barley campaign, plant height ~20 cm. Only one master image is used.

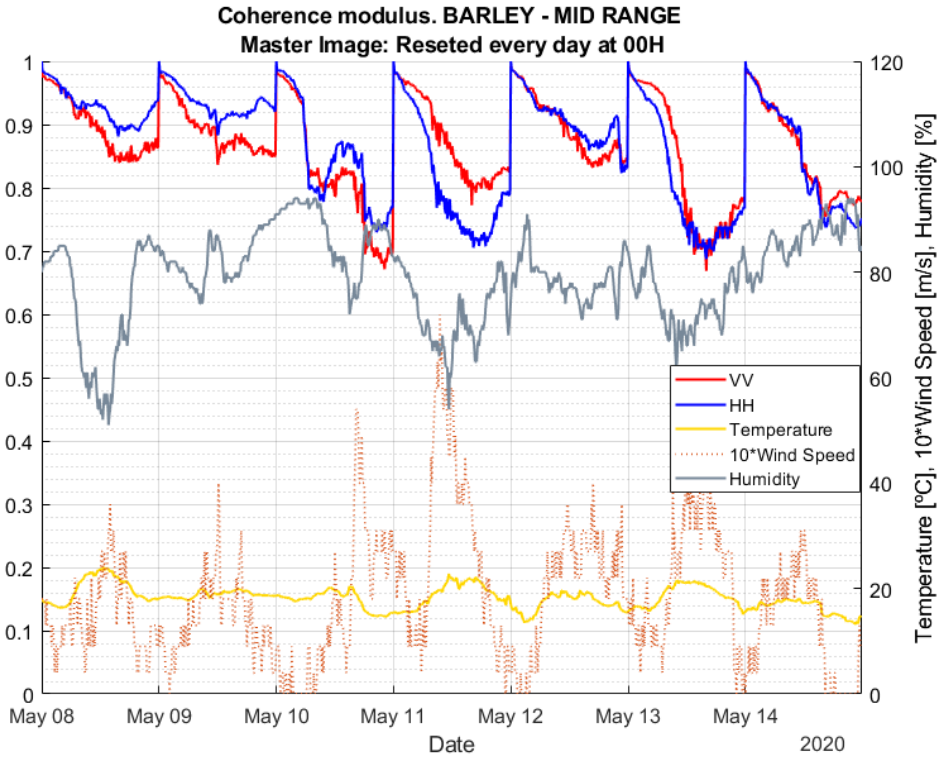

Figure 6.42 Modulus of the coherence. Barley campaign, plant height ~20 cm. Master image reset every 24 h.

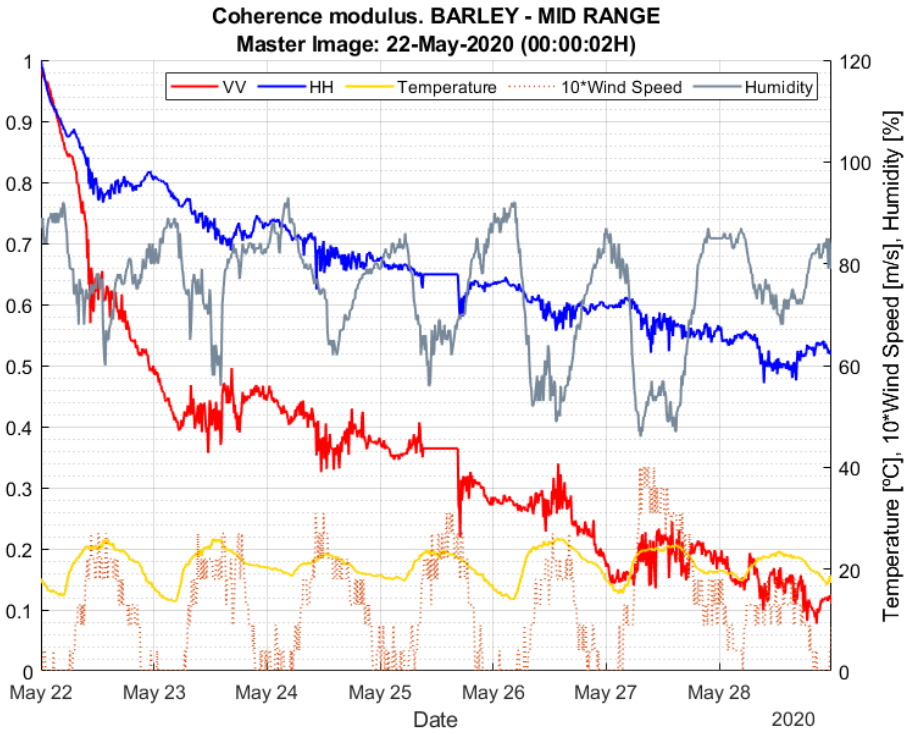

Figure 6.43 Modulus of the coherence. Barley campaign, plant height ~40 cm. Only one master image used. The radar did not operate for few hours around noon of May 25.

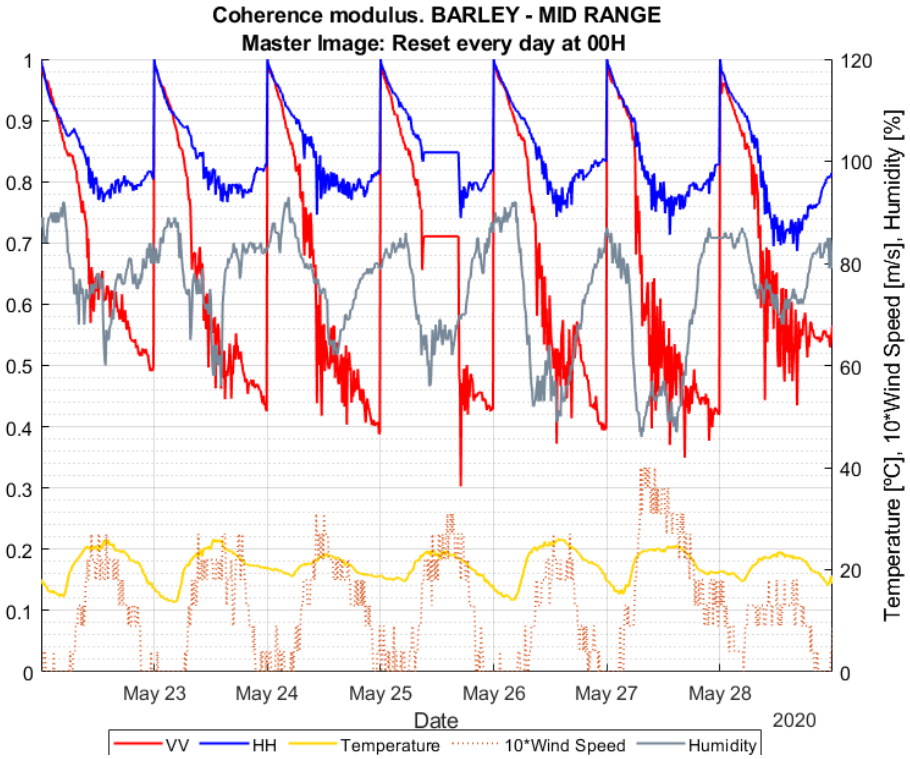

Figure 6.44 Modulus of the coherence. Barley campaign, plant height ~40 cm. Master image reset every 24 h. The radar did not operate for few hours around noon of May 25.

Furthermore, the influence of wind can be observed with a higher coherence decay and instability when the wind is stronger, typically around noon and afternoon. The coherence increases again when wind stops (mostly during the night). As expected the wind impact is proportional to plant height and density.

From these results, present models relating crop height and radar observations can be reviewed to study possible improvements that could be exploited in present and future missions, considering the limitations in revisit time and local times of satellite ascending and descending passes.

6.4.6.2 Multitemporal Coherence Matrix. Impact of time baseline length

When a time series of N SAR images S(t) is available, a multitemporal coherence matrix can be defined [23] [24].

$$\hat{\Gamma} = \begin{bmatrix} 1 & \gamma_{12} & \gamma_{13} & \cdots & \gamma_{1N} \\ \vdots & & \ddots & & \vdots \\ \gamma_{N1} & & \cdots & & 1 \end{bmatrix} \tag{6.3}$$

where the complex coherence elements γ_{ij} are

$$\gamma_{ij} = \frac{\langle S(t)S^*(t+\Delta t)\rangle}{\sqrt{\langle |S(t)|^2\rangle\langle |S(t+\Delta t)|^2\rangle}} \tag{6.4}$$

and Δt is the temporal baseline between images.

This matrix contains all possible combinations of images of dataset. The absolute value of any element provides the coherence between different elements of the dataset. The coherence is symmetric $|\gamma_{ij}| = |\gamma_{ji}|$ and therefore all the information can be obtained from the upper o lower triangular matrix. If the data is ordered chronologically, all the terms close to the matrix main diagonal presents a short temporal baseline. The rows and columns of the matrix represent the classical master-slaves time series terms described in the previous section. The impact of the length of the temporal baseline on the coherence will be analysed from the k-diagonal terms of the matrix, where k=0 is the main diagonal of the matrix, k > 0 are the diagonals above the main one. For a given k-diagonal, all its terms have the same temporal baseline. For this analysis, the following temporal baselines between images have been selected: 10 minutes, 1 hour, 4 hours, 24 hours, 3 days and 6 days in both crops. All figures show mid-range data, but the result would be equivalent for near and far range. In the figures, coherence has been located on the x-axis at the lower date of the two images.

Figure 6.45 shows the coherence between images with a temporal baseline of 10 minutes (k=1 diagonal matrix) of the whole barley crop campaign for HH and VV channels including rain intensity and crop height evolution. As expected for such a small temporal baseline, coherence presents very high values except for those rainfall events that reduce it. As vegetation grows, coherence fades appear associated with variations in the wind in the diurnal cycle, which can be observed in more detail in Figure 6.46, where the period from 8 May to 5 June has been represented. In this figure, the entire growth process of the plant is presented. It can be clearly seen how this fading is associated with an increase in wind speed that occurs during daytime. In the absence of wind, coherence returns to its high values. As the vegetation grows, this phenomenon is accentuated and is more affected in the VV polarization than in the HH polarization. This is caused by differential extinction since the VV channel is more affected by attenuation than the HH channel and therefore the volumetric component is more important than that produced by the soil. For a temporal baseline of 1h or 4h (Figure 6.47, Figure 6.48, Figure 6.49 and Figure 6.50) the same phenomena analysed in the previous figures are observed but with a loss of coherence produced by the increase in the temporal baseline between images.

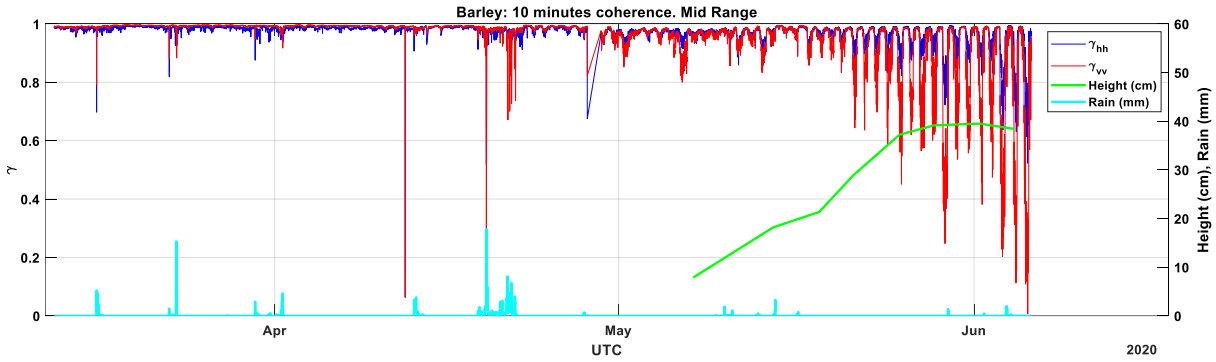

Figure *6.45 Time series of 10 minutes temporal baseline coherence of the whole barley crop campaign for HH and VV channels for Mid Range: incidence angles (59.1 °to 63 °) including rain intensity (cyan) and crop height evolution (green)*

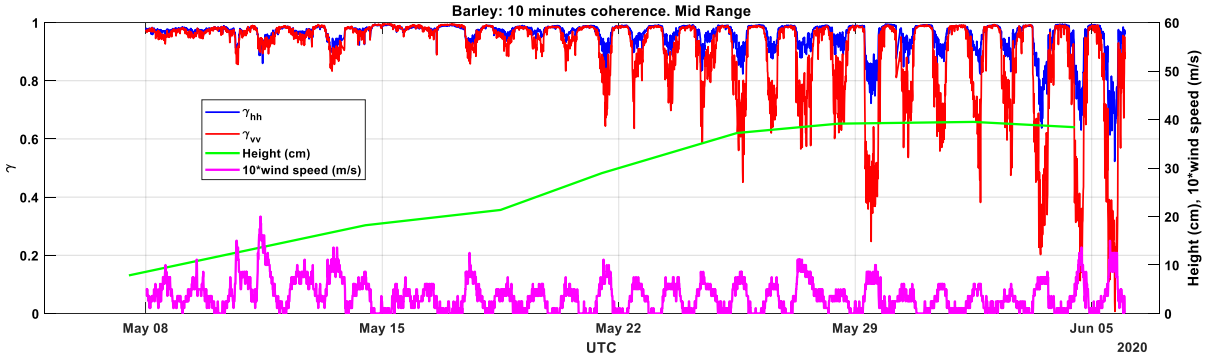

Figure 6.46 Time series of 10 minutes temporal baseline coherence of barley crop between 8 May and 5 June for HH and VV channels for Mid Range: incidence angles (59.1 °to 63 °) including wind speed (magenta) and crop height evolution (green)

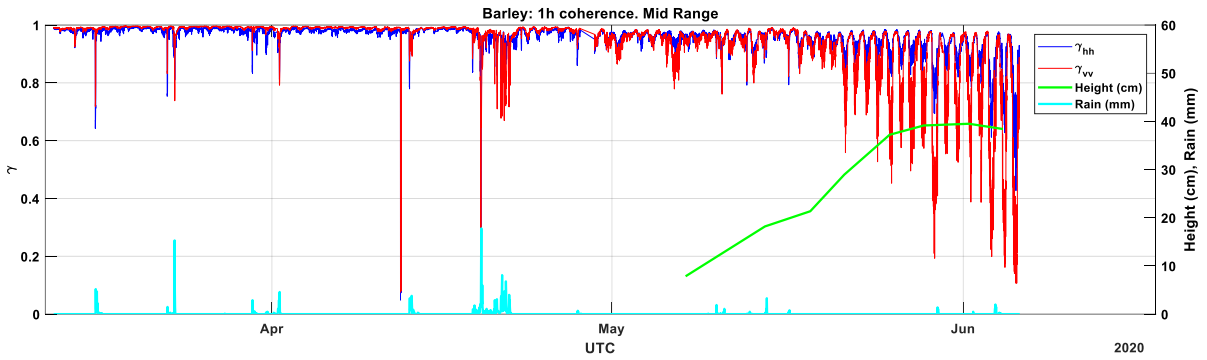

Figure 6.47 Time series of 1 hour temporal baseline coherence of the whole barley crop campaign for HH and VV channels for Mid Range: incidence angles (59.1° to 63°) including rain intensity (cyan) and crop height evolution (green)

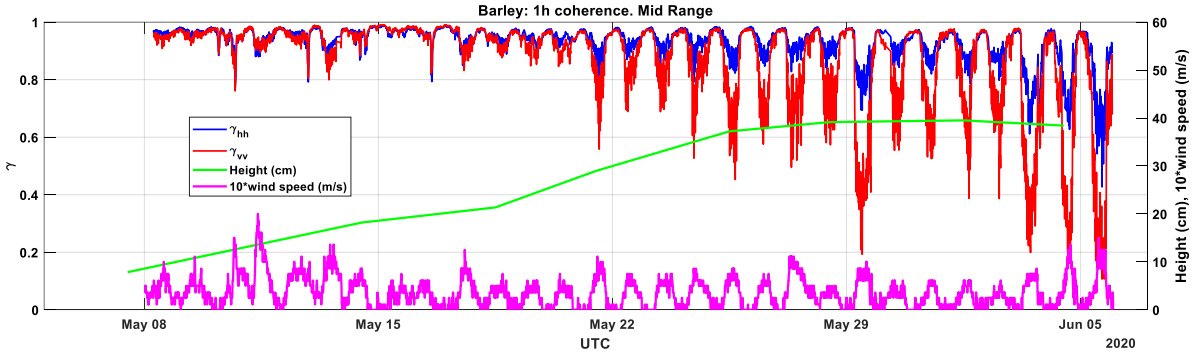

Figure 6.48 Time series of 1 hour temporal baseline coherence of barley crop between 8 May and 5 June for HH and VV channels for Mid Range: incidence angles (59.1° to 63°) including wind speed (magenta) and crop height evolution (green)

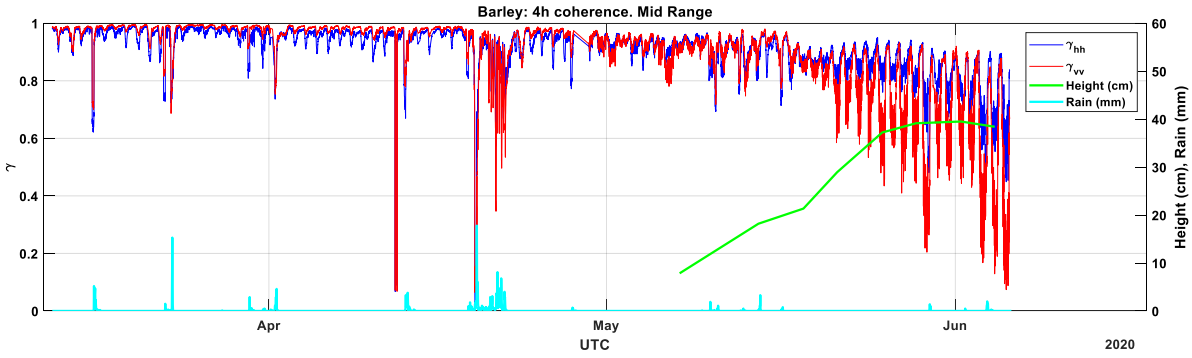

Figure 6.49 Time series of 4 hours temporal baseline coherence of the whole barley crop campaign for HH and VV channels for Mid Range: incidence angles (59.1° to 63°) including rain intensity (cyan) and crop height evolution (green)

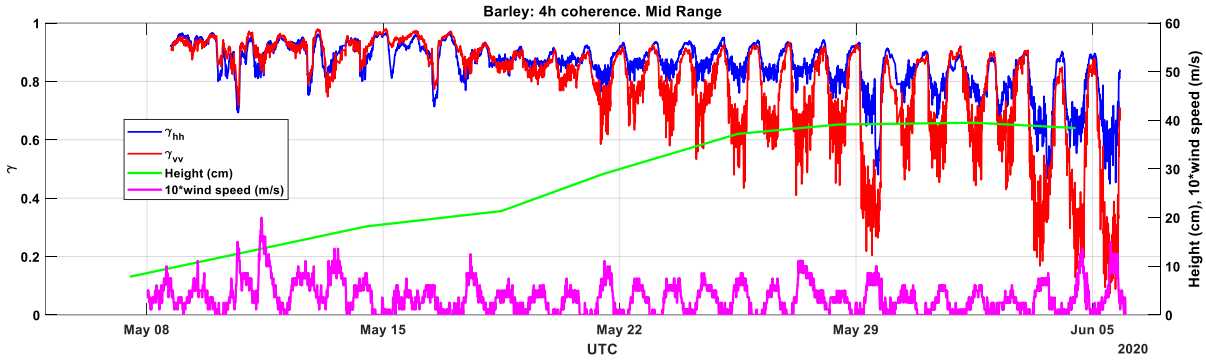

Figure 6.50 Time series of 4 hours temporal baseline coherence of barley crop between May 8 and June 5 for HH and VV channels for Mid Range: incidence angles (59.1°to 63°) including wind speed (magenta) and crop height evolution (green)

Figure 6.51, Figure 6.52 and Figure 6.53 show the coherence between images with a temporal baseline of 1 day, 3 days and 6 days respectively of the whole barley crop campaign for HH and VV channels including rain intensity and crop height evolution. A temporal baseline of 6 days coincides with the repeat pass that the Sentinel 1 constellation (A and B) can provide at the moment. If there is no vegetation or it is very low, coherence presents high values except for rain events. When the plant reaches a height of around 20 cm, the co-polar components begin to separate, presenting a greater loss of coherence in VV polarization than HH polarization as the plants grow. As expected the loss of coherence increases with the temporal baseline.

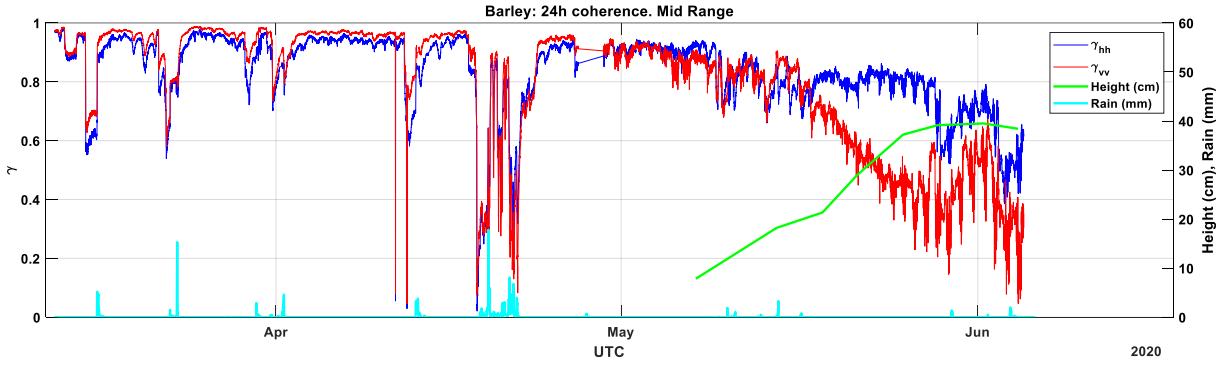

Figure 6.51 Time series of 24 hours temporal baseline coherence of the whole barley crop campaign for HH and VV channels for Mid Range: incidence angles (59.1°to 63°) including rain intensity (cyan) and crop height evolution (green)

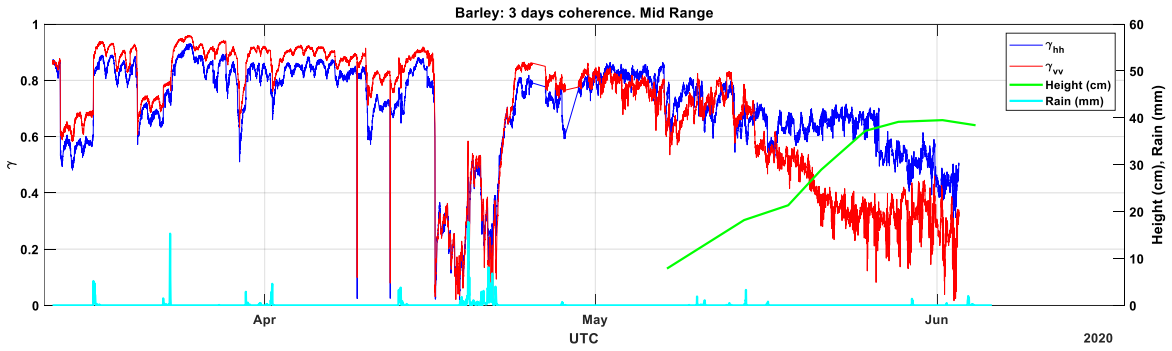

Figure 6.52 Time series of 3 days temporal baseline coherence of the whole barley crop campaign for HH and VV channels for Mid Range: incidence angles (59.1° to 63°) including rain intensity (cyan) and crop height evolution (green)

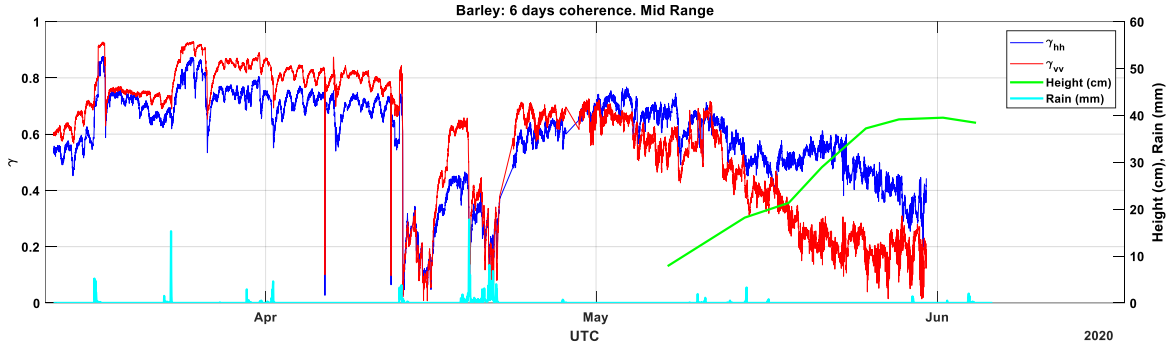

Figure 6.53 Time series of 6 days temporal baseline coherence of the whole barley crop campaign for HH and VV channels for Mid Range: incidence angles (59.1° to 63°) including rain intensity (cyan) and crop height evolution (green)

6.4.6.3 Barley crop phase changes

For the same time intervals for which the short and long-term coherence magnitude has been studied in section 6.4.6.1, the interferometric phase has also been computed to see if, as it happened with the coherence modulus, a possible relation exists between the crop height and the interferometric phase evolution. A spatial average value of the field phase change has been obtained as the argument of the complex coherence parameter. In this way, considering the speckle random pattern of SLC images, the pixels with higher radar reflectivity receives more weight in the phase computation compared to the noisier lower amplitude pixels. Only the mid range zone of corn crop has been studied so far, which has the best compromise between number of looks and incidence angle.

In Figure 6.54, Figure 6.55 and Figure 6.56, the interferometric phase results for the calibrated radar images are presented. To avoid the impact of air refractivity changes on the results, the phase has been computed from the atmospheric compensated images (level 1c product).

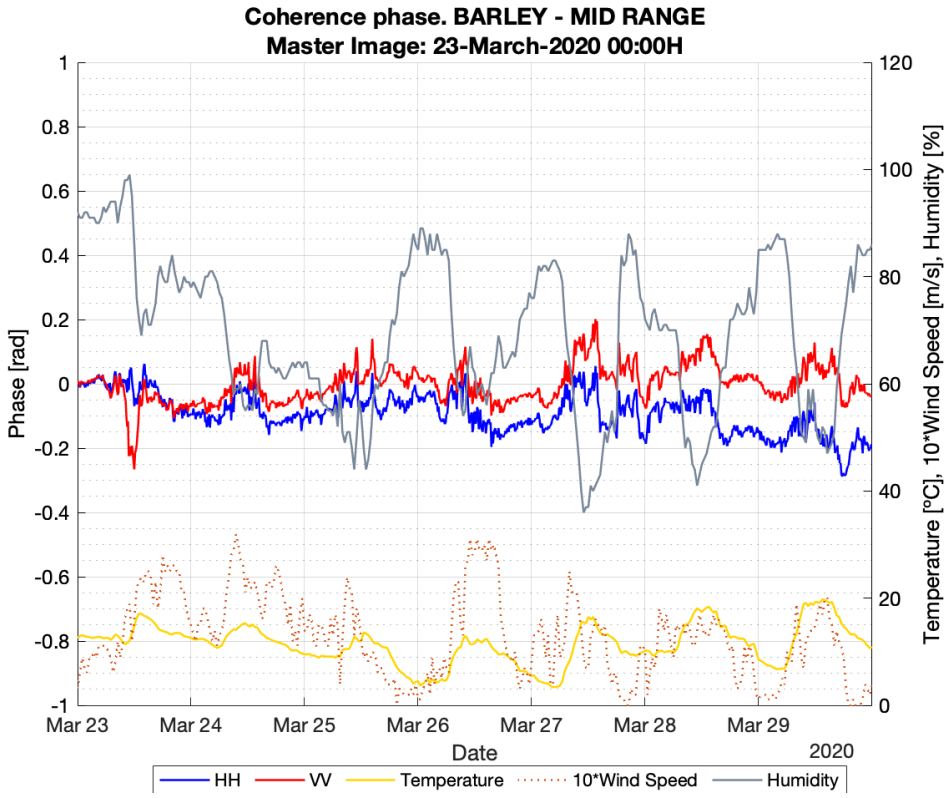

Figure 6.54 Phase of the Coherence. Plant height ~5 cm. The first image of the interval is the Master.

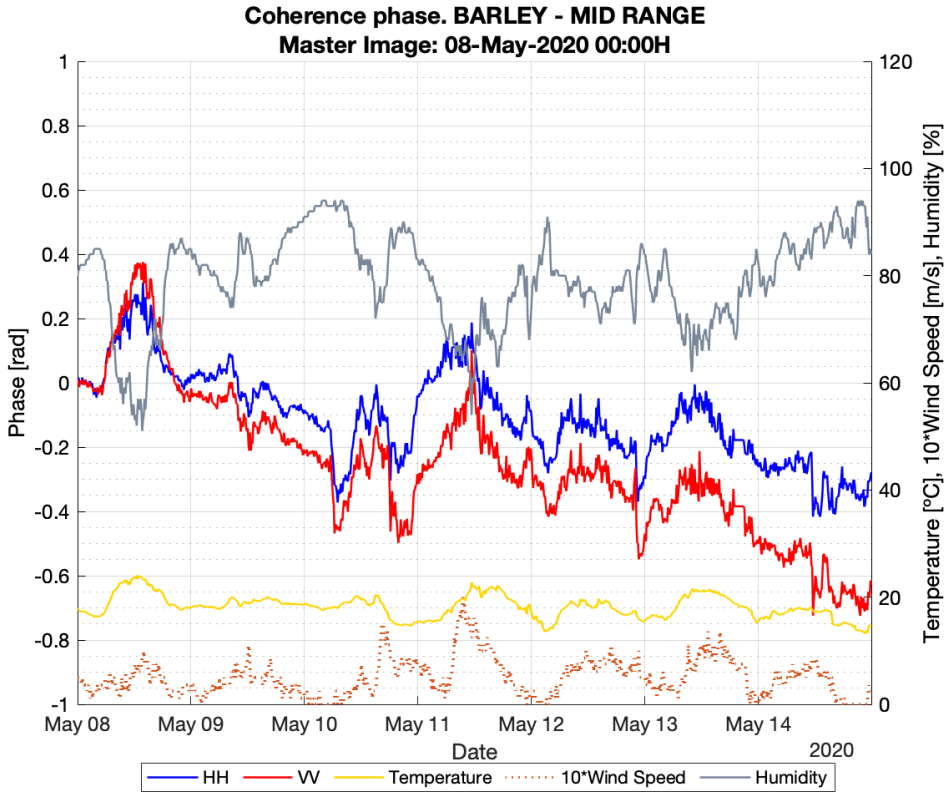

Figure 6.55 Phase of the Coherence. Plant height ~20 cm. The first image of the interval is the Master.

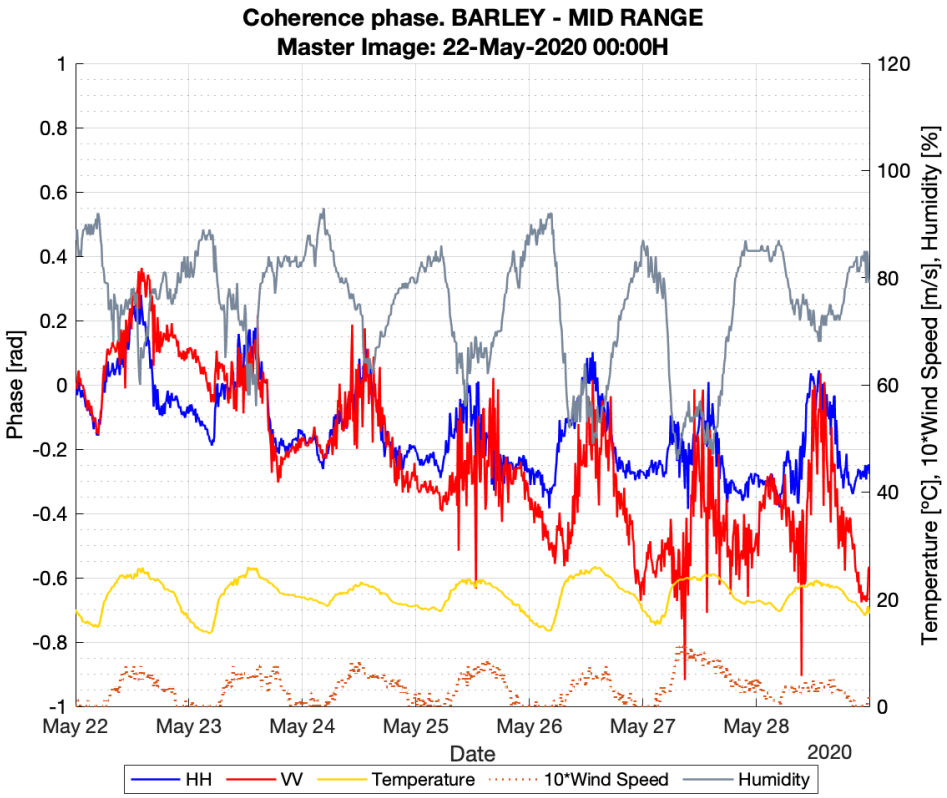

Figure 6.56 Phase of the Coherence. Plant height ~40 cm. The first image of the interval is the Master.

From the obtained phase results, shown in Figure 6.54, Figure 6.55 and Figure 6.56, there is no clear relationship between crop height and interferometric phase evolution.

Nevertheless, the phase evolution shows an inversely proportional relationship with the atmospheric humidity in the three studied cases. The results are very similar if obtained from the level 1b product which has no atmospheric refractivity phase compensation. For this reason, the observed impact of air humidity on the image phase is predominantly due to changes in the scene surface and volumetric complex backscattering.

The impact of wind velocity, typically larger around noon every day, introduces fast phase fluctuations, associated to plants random motion. The resulting phase decorrelation is particularly strong in the last processed week (Figure 6.56) corresponding to the largest crop height.

6.4.6.4 Impact of field operations on coherence

The fact of having a radar operated with an acquisition period of 10 minutes eases the detection of fast changes of the scenario. Figure 6.57 shows the coherence map evolution of the field on 4 March 2020, the day of the barley sowing, from 8:30 to 13:00 (UTC), of consecutive pairs of SLC every 10 minutes. The different tracks of the tractor are clearly seen. A detail of the sowing operation seen from the radar site is depicted in *Figure 6.58*.

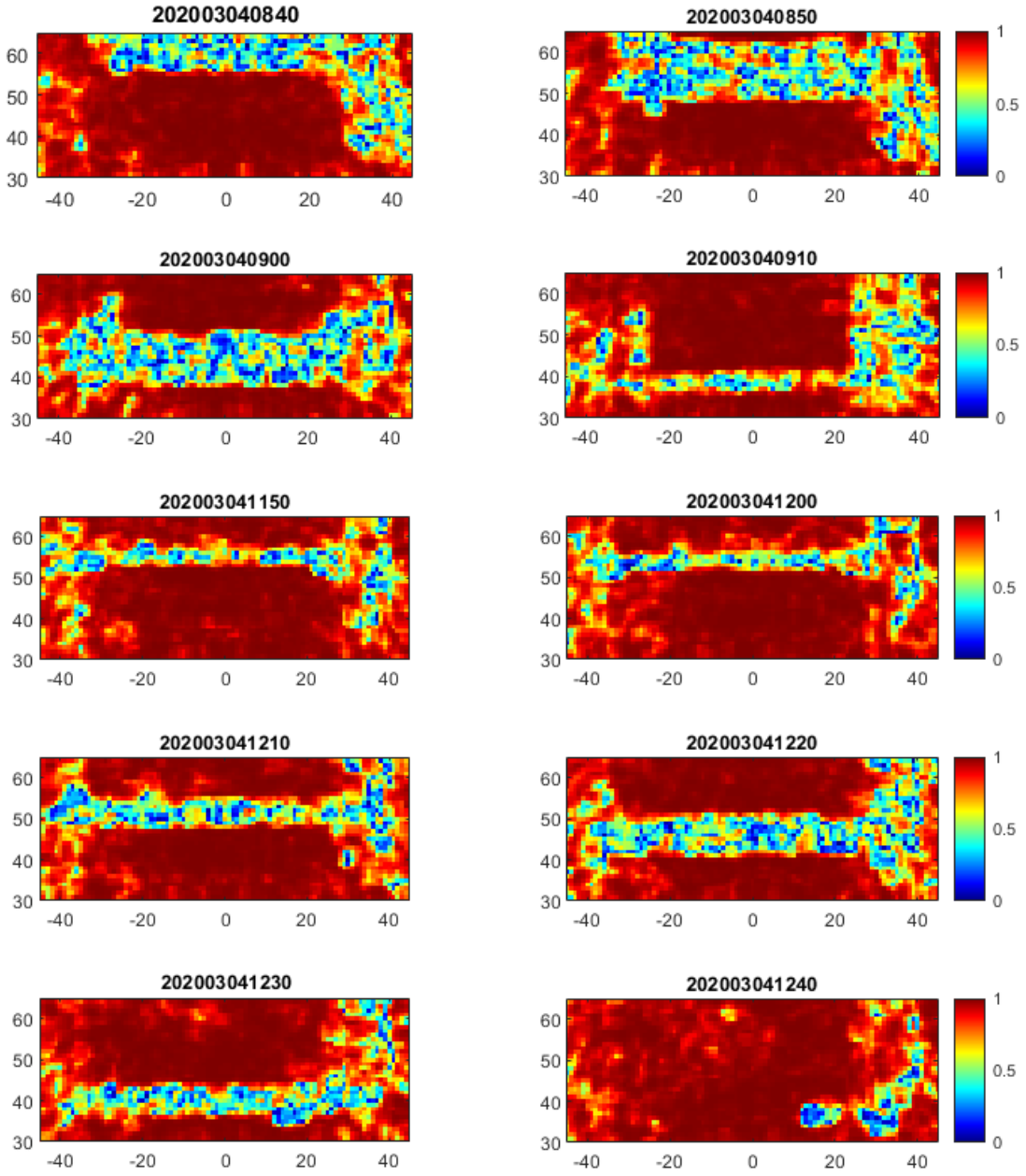

Figure 6.57 Temporal sequence of Coherence maps between consecutive 10 minutes SLC images from 4 March 2020. Image number is: <YYYY:year, MM:month, DD:day, HH:hour, mm: minutes>.

Figure 6.58 Picture taken at 4 March 12:15H from the radar site showing the barley sowing operation.

7 CORN CAMPAIGN

After the strict lockdown imposed in Spain since the beginning of the first campaign, the main RADAR instrument and sensors for ancillary data gathering could be fully deployed for the corn campaign. The radar was operated with few modifications as expected. The main ancillary parameters were acquired by means of different sensors and data loggers deployed by the members of CommSensLab and EEABB School. Hereafter only the modifications/improvements on the main instrumentation used in the second campaign of the project respect to the barley campaign will be described.

The main instrument was the same Ground Based Full-Polarimetric Synthetic Aperture Radar (GB-PolSAR) as the one used in the barley campaign. Few modifications were introduced in the system:

- The original 3D printed and metalized four pyramidal horn antennas were replaced by four brass based equivalent radiating elements. The new set of antennas were fully characterized at the anechoic chamber of CommSensLab in order to obtain the new correction terms for the SLC image compensation.
- The tilt angle of the antennas was modified from -15° to -30°, improving the illumination of the field and maximizing the polarimetric purity of the antenna over the corn field.
- The frequency generation unit was reprogrammed to generate a 5.6 GHz centred, 200 MHz bandwidth chirp signal.
- Both receiver channel Gains were increased by 10 dB. After checking the echo signal levels in the first campaign, it was concluded that the gain could be increased, improving the signal dynamic range. Both receiver channels frequency responses were characterized and used in the SLC image compensation.

Parameter	Value
Central Freq.	5.6 GHz
Bandwidth	200 MHz
Mode of Operation	Full-Polarimetric
Modulation	Saw-Tooth FM-CW
Peak Transmitted Power	28.7 dBm EIRP
Chirp PRF	338.5 Hz
Ramp duration	1.47 ms
Receiver Gain	50 dB
Receiver Noise Figure	2 dB
Antenna Gain	9.7 dB
3dB Antenna Beamwidth	60˚ (Azi), 40˚ (Elev)
Base Band Beat Frequency	902 Hz/m
ADC resolution	14 bits
No. of samples/ramp sweep	2048
Aperture length	1.477 m
Rail speed	1 m/s
Temporal baseline	10 minutes

Table 7.1. RADAR main parameters for corn crop campaign.

7.1 Corn crop description

Corn (Zea Mays L.) is a crop with tropical origin that is cultivated in warm and humid conditions. Temperature is a key factor for crop development which greatly depends on accumulated temperatures during the season (starting from 6 ˚C). Water availability is a limiting factor to ensure corn biomass development and yield, with annual water needs of around 700 mm. There exists different corn varieties and crop cycles, from short (80 days) to super long cycles (more than 155 days). The longer the cycle the higher the yield potential.

The corn planted was *Zea Mays L. Konfites* from *KWS enterprise*. It is a cycle FAO 400 (a FAO cycle is defined as the accumulated average day temperature from seeding to maturity of the grain). This is translated as a short period crop (from 80 to 110 days), useful as a second crop of the season.

The first stage of corn phenology starts when the seed emerges from the ground, exposing small, typically rounded, leaves. Emergence can take several days depending on the depth of planting, soil moisture, and soil temperature. After emergence, leaves appear, expand, and reach their maximum sizes, causing the plant canopy and biomass to grow exponentially. The end of the growth of each leaf is marked by the appearance of a "collar" at the base of the leaf, where it attaches to the stem. These "collars" are noticeable to an observer in an actively-growing corn field and have been used by farmers to compare growth patterns across fields and years, and to adjust their management decisions. A critical milestone in the phenology of row crops like corn is flowering. This stage of development marks the transition from vegetative growth to reproductive growth, when kernels are formed and filled with carbon and nutrients. This is a critical period for the plant, as the corn plant directs scarce resources to the kernels to build them up. This redirection of resources to the kernels limits the availability of resources to the rest of the plant. Kernels are the only organs on the plant that can ensure perpetuation of the species. In corn, when kernels are filled to full capacity, a black layer appears at the base of the kernel, signalling the maturity stage

This crop is really demanding on Nitrogen fertilization. From 6th leaf collar the demand is boosted and between 4th and 12th week of crop, the 85% nitrogen is absorbed.

The most crucial stages of the crop regarding water availability and nitrogen presence are: emergence, silking (stage R1 ±15 days) and blister of the grain.

During the vegetative period (that can occur from 2 to 8 weeks) 50% of the leaves are visible. Then, from tasselling to pollination (around 3 to 3.5 weeks more) 80% of leaves are visible, until blistering (around 3 to 3.5 weeks more), where 100% of the leaves are visible.

According to Ritchie and Hanway development stage classification [25], two principal phases are identified: vegetative and reproductive. On the following table (Table 7.2), all the stages are described. Some of this growth stages were observed during field monitoring.

R&H Code	Description	Obs. date	R&H Code	Description	Obs. date
Vegetative phase			Reproductive phase		
VE	emergence	6 July 2020	R1	silking	21 Aug. 2020
V1	first leaf collar	10 July 2020	R2	blister	31 Aug. 2020
V2	second leaf collar	17 July 2020	R3	milk	
V3	third leaf collar	22 July 2020	R4	dough	16 Sept. 2020
V4	fourth leaf collar		R5	dent	
V5	fifth leaf collar		R6	maturity	11 Nov. 2020
V6	sixth leaf collar	3 Aug. 2020			
V7	seventh leaf collar				
V8	eighth leaf collar	11 Aug. 2020			
Vt	tasseling				

Table 7.2 Stages of the corn crop campaign

7.2 Chronology

The Table 7.3 and the Figure 7.1 describe the main events of the corn campaign.

22 June 2020	Radar operates in 24/7 mode, performing a measurement every 10 minutes. The Corner Reflector is installed at NR Centre. 45° tilt dihedral is kept at FR Left
25 June 2020	Field preparation for sowing
26 June 2020	Corn is sown
24-25 June 2020	Non-programmed radar halt. From 15:30 to 14:40 aprox.
29-30 June 2020	Soil Roughness is measured with the Laser Ranger
30 June 2020	Drip Irrigation system is deployed
1 July 2020	Drip Irrigation is activated for the first time
2-3 July 2020	Non-programmed radar halt. From 00:00 to 07:30 aprox.
6 July 2020	2 *VanWalt* Soil Moisture Dataloggers, with 2 pairs of *HydraProbe* and 2 pairs of 3 segment *GroPoint* sensors, are deployed at Near and Far Range
8 July 2020	A 90° tilted Dihedral is installed beyond the field, at the right part.
10 July 2020	Part of the field (Far Range) is resowed
13-14 July 2020	Human activity on the field.
16 July 2020	Heavy rain.
17 and 21 July 2020	45° tilted dihedral is readjusted
22 July 2020	Human activity on the field.
23 July 2020	90° tilted dihedral is readjusted
30 July -16 Sept. 2020	Soil Moisture datalogger at Far Range Out of Order
17 August 2020	Field is fertilized (50Kg of Nitrosulfate)
31 August 2020	45° tilt dihedral is moved from original place to beyond Far Range centre
1 and 21 Sept. 2020	Radar is operated in 2minute Time Baseline
16 September 2020	1-day Water Cycle Campaign.
25 September 2020	Windy day. System is operated in Doppler Spectrum mode
7 October 2020	A Flat panel is installed at Near Range (Right). The pole where the flat panel was attached showed a progressive inclination and rotation movement. A slight movement of the pole that held the CR is detected.

10 October 2020	Intense Rain period
4 November 2020	Soil moisture data loggers are disassembled. Drip Irrigation hose are eliminated
6 November 2020	Human activity on the field
16 November 2020	Radar stops taking measurements

Table 7.3 Main events of the corn campaign.

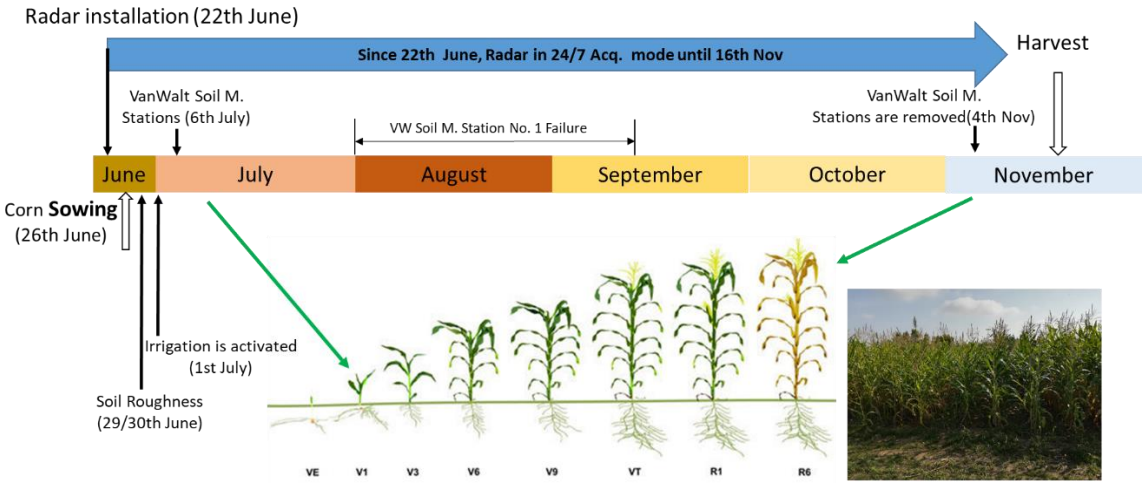

Figure 7.1. TimeLine and main events of the corn crop campaign.

7.3 Ancillary data

7.3.1 Soil roughness

Soil Roughness was measured at the beginning of the corn campaign (29 and 30 June 2020), just after seeding (26 June 2020). The measuring instrument was the same laser ranger (LEICA Disto Pro) used in the first campaign. The laser ranger was moved along a linear motion unit of 2 m length (Figure 7.2). Every soil roughness profile was sampled every 2 mm for the length of the rail. Different roughness profiles were taken from different places and orientations on the field. To characterize the surface roughness, the standard deviation of the surface height variation (or rms height) and the surface correlation length were obtained [9] (Table 7.4) (Figure 7.3).

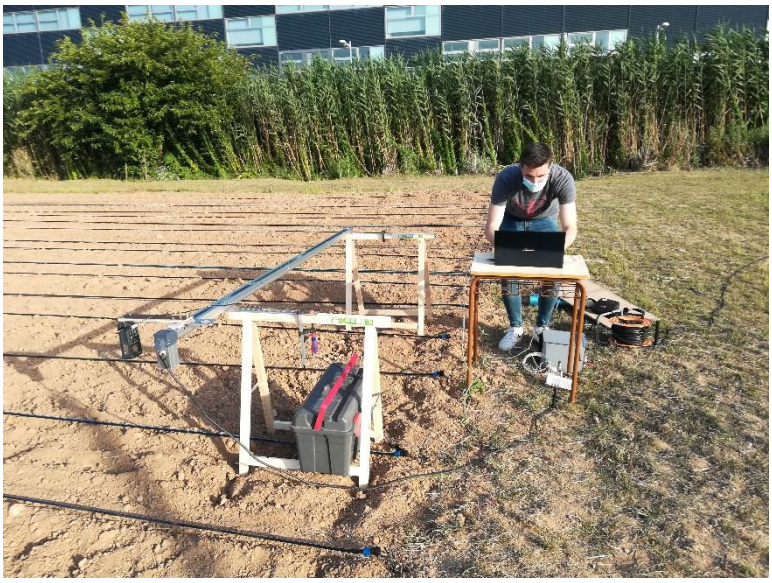

Figure 7.2. Soil Roughness was measured, as in the barley campaign, by means of a Laser ranger on a rail. The Profile length was 2.1m with a sampling interval of 2 mm. Different locations of the field were measured with different rail orientations.

LASER PROFILES	***s* (mm)**	***l*(mm)**	***k·s***	***k·l***	***s/l***
Far Range LEFT rough (Cross-Range)	10.6	300	1.24	35.19	0.04
Far Range LEFT (Range)	29.0	240	3.40	28.15	0.12
Far Range LEFT (Range)	20.9	164	2.45	19.23	0.13
Mid Range LEFT (Cross-Range)	9.8	300	1.15	35.19	0.03
Mid Range LEFT (Range)	26.4	256	3.10	30.03	0.10
Near Range CENTRE flat (Cross-Range)	6.9	422	0.81	49.49	0.02
Near Range CENTRE rough (Cross-Range)	16.1	40	1.88	4.69	0.40
Near Range CENTRE (Range)	25.3	142	2.97	16.65	0.18
Average value	**18.1**	**233**			
Std. Dev	**7.9**	**109**			

*Table 7.4 Soil Roughness parameters extracted from Laser Ranger and Photogrammetric profiles. **s** is the rms height while **l** stands for the surface correlation length. **k** is the wavenumber. Names of the laser profiles correspond to the different locations in the field. The orientation of the cut respect to the radar is indicated (in parentheses). Different profiles were taken in Cross-Range orientation because the field showed different soil roughness patterns.*

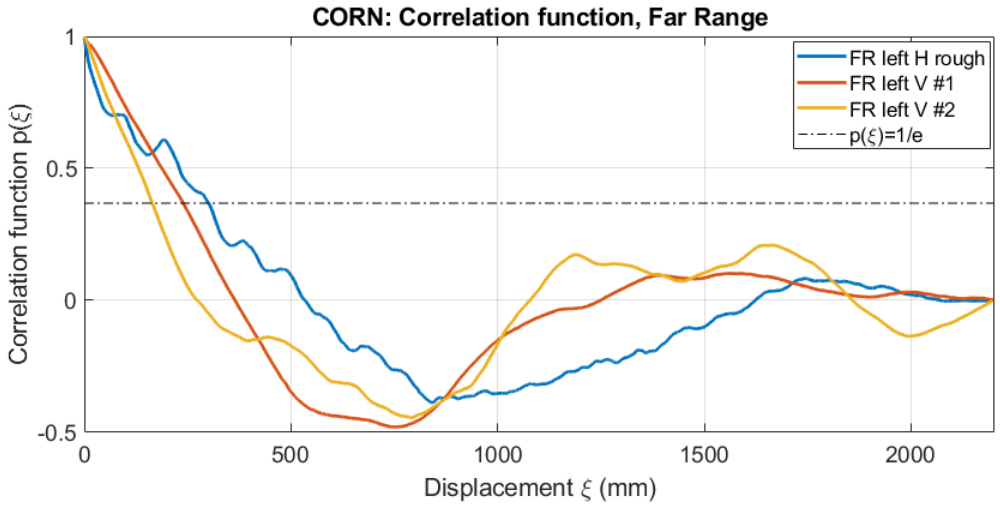

Figure 7.3. Correlation function of the different roughness profiles taken by laser ranger.

7.3.2 Soil moisture

The planned number of soil moisture sensors could finally be installed since the second week of the corn campaign. Two pairs of data loggers were deployed at Near and Far Range, each of them included two pairs of different soil moisture sensors, 3-segments *GroPoint* sensors (RIOT Technology Corp.) (Table 7.5) and two *HydraProbe* sensors (Stevens Water Monitoring Systems, Inc.) (Table 7.6) (Figure 7.4).

Figure 7.4. HydraProbe (left) and the 3-segment GroPoint (right) Soil Moisture sensors

HydraProbe sensors provide soil permittivity and electrical conductivity, soil temperature and temperature compensated soil moisture for a segment of 10 cm, while *GroPoint* 3-segment sensors provide Soil Moisture and Temperature of the segments 0-15 cm, 15-30 cm and 30-45 cm.

The equipment was delivered and installed on 6 July 2020. As originally planned, two main sets of sensors with their corresponding data loggers (hubs) were installed after sowing, one of them in the Near Range field side and the second in Far Range side of the field. Each data logger acquired soil parameters data from 2 *HydraProbe* and 2 *GroPoint* 3-segment sensors. As a drip irrigation system was used in the corn campaign, the sensors were deployed at different positions, close or centred with respect to the irrigation lines as shown in Figure 7.5 and Figure 7.6. In this way the different

soil moisture values due to the irrigation process could be measured. The Near Range data logger (Hub 000163) and sensors operated continuously taking measurements every 15 min. The Far Range data logger (Hub 000162) ceased to operate due to an internal power supply regulation failure on 30 July and was sent to the UK provider for repair. It was reinstalled and operated correctly again from 16 September.

Gravimetric Soil Moisture determination by means of soil sample extraction was also done using T-style samplers, as in the barley campaign.

Moisture	
Measurement range	0% to 100% of VMC
Accuracy	±2.0%
Precision	< 0.2%
Temperature	
Measurement range	-20°C to +70°C (-4°F to 158°F)
Accuracy	±0.5°C
Electrical	
Input voltage	6 to 14 VDC max. 18 VDC
Current consumption	Quiescent: Active: 15-20 mA for 100 mS
Environmental	
Operating temperature	-20°C to 70°C (-4°F to 158°F)
Storage temperature	-40°C to 85°C (-40°F to 185°F)
Physical	
Length	3-segment probe is about 45cm long.
Probe weight	3 segments: 351 g (12.4 oz.)
Temperature Placement	3 segments: 3.5 cm, 10 cm, 20 cm, 30 cm, 40 cm, and 45 cm

Table 7.5. Main specifications of the 3-segment GroPoint sensor

Measurement	**ACCURACY**
Real dielectric permittivity (isolated)	± 0.5% or ± 0.2 dielectric units
Soil moisture for inorganic & mineral soil	± 0.01 WFV for most soils ± 0.03 max for fine textured soils
Bulk electrical conductivity	± 2.0% or 0.02 S/m whichever is typically greater
Temperature	± 0.3°C
Inter-sensor variability	± 0.012 WFV (θ m^3 m^{-3})
Electrical	
Power supply	9-20 VDC
Power consumption	1 mA idle / 10 mA active for 2 seconds during duty cycle
Environmental	
Operating temperature range	Standard temperature probe range: -10 °C to +60 °C
Storage temperature range	-40 °C to +65 °C
Water resistance	Tolerates continuous full immersion
Length	4.9” (124 mm)
Diameter	1.6” (42 mm)
Weight	7 oz. (200 g)
Sensing volume (cylindrical region)	Length: 2.2” (5.7 cm), Diameter: 1.2” (3.0 cm)

Table 7.6. Main specifications of the HydraProbe sensor.

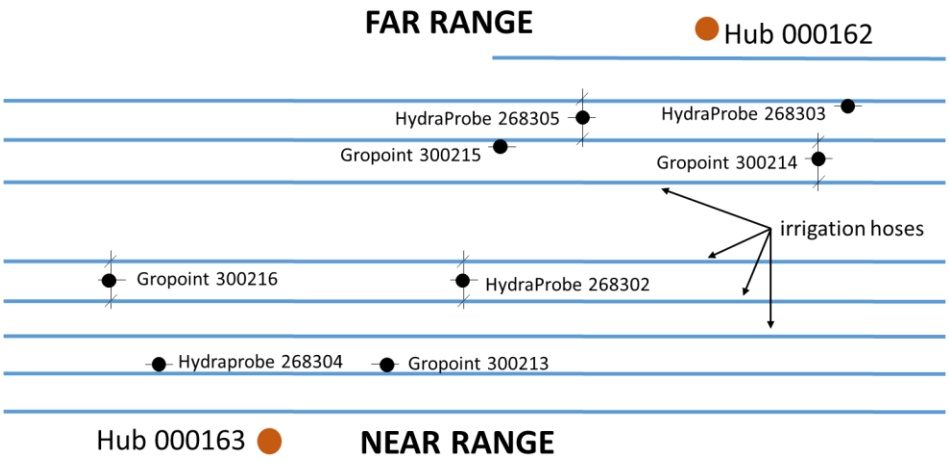

Figure 7.5. Map of the location of the Soil Moisture sensors. Two pairs of sensors are connected to each data logger. For each data logger, one pair of different sensors is placed close to an irrigation hose while the other pair is placed in between two hoses.

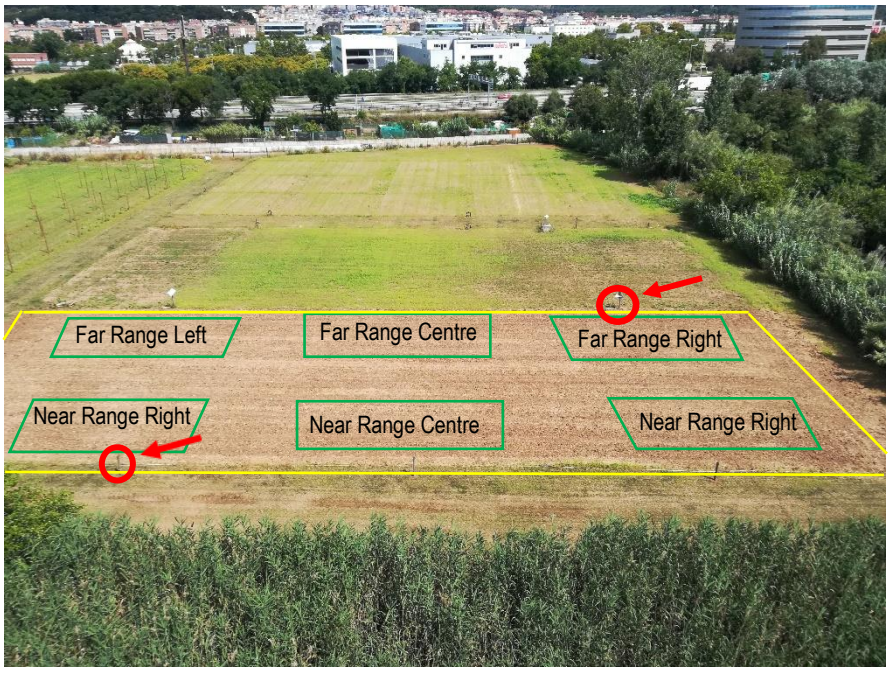

Figure 7.6. Two soil moisture Data loggers were placed at Near and Far Range. The sensors were deployed at least 4 meters from the contour in the field.

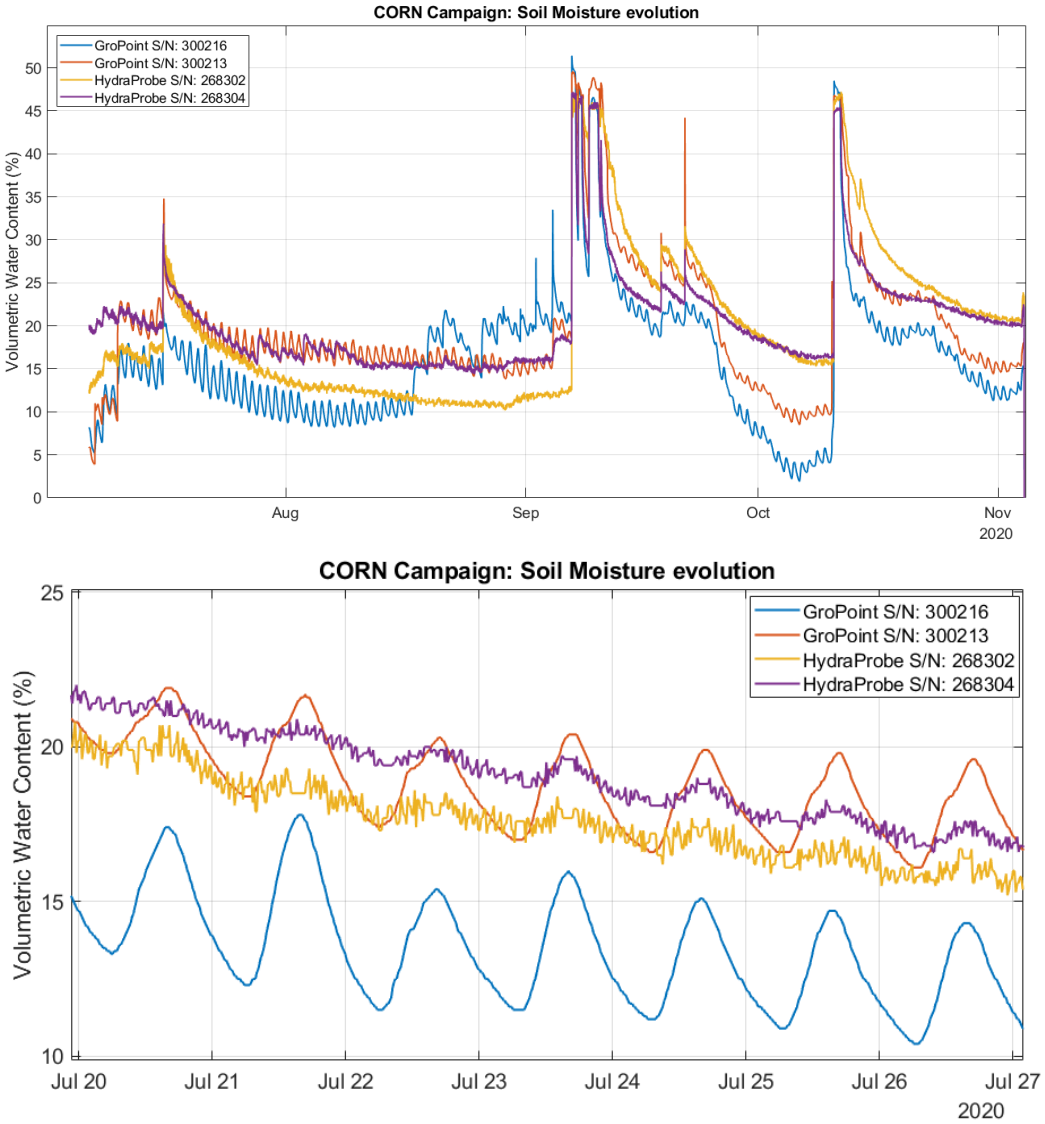

Figure 7.7. (Top) Soil Moisture evolution since 6 July 2020, taken by the four different Soil Moisture sensors (0-15 cm depth) at Near Range. Different rain and irrigation events occurred during the campaign. As in the Barley campaign, the sensors, especially the GroPoint probes measured daily variations. (Bottom) Zoom of the period 20 to 27 July 2020.

As in 6.3.2, some comments have to be pointed out about the soil moisture sensors.

The soil moisture sensors use either a TDR or a capacitance technique; both of which indirectly measure the soil dielectric constant to determine the soil moisture content. According RIOT Tech Corp, GroPoint soil moisture sensors utilize the Time Domain Transmission (TDT) method of measuring soil moisture, which is a refined version of the Time Domain Reflectometry (TDR) technique. TDT-based sensors do not need to be calibrated to each type of soil they will be buried in. Near-surface measurements of soil water content using TDR may exhibit anomalous behaviour in the presence of diurnal temperature fluctuations [15]. HydraProbe Sensors [16] are based on measuring the energy storage and energy loss across the soil using a 50 MHz signal [17]. It is pointed out that these sensors are less sensitive to changes in temperature, salinity and soil mineralogy.

After some review of literature about Soil sensors, it is important to notice the following: For soils with water content below the equilibrium water content (θ_{eq}), the temperature effect of soil

dielectric permittivity is positive, i.e. it increases with temperature, and for soils with water content above θ_{eq}, the temperature effect of soil dielectric permittivity is negative, i.e. it decreases with temperature [17]. Thus, any sensor that is based on the determination of the Volumetric Water Content by means of the measurement of the dielectric property of the soil would be strongly affected by the soil temperature. This can cause moisture readings to Go Up when the substrate/soil is actually drying out and vice versa

After Figure 7.7, a difference in sensor performance is clearly seen. For example, comparing the VWC from sensor GroPoint 300213 and HydraProbe 268304, both buried close to an irrigation hose, a clear daily fluctuation of the VWC is seen for the GroPoint sensor while the HydraProbe shows a reduced daily fluctuation, despite both are measuring at the same depth of 0-15 cm. The same applies for the other pair of sensors, buried in between two irrigation hoses.

Despite a slight change of VWC during a day cycle that has to be assumed in the 0-15 cm sector, with a reduction during the day due to the effect of the sun and an increment by night due to nocturnal dew, retrieved values from the sensors are showing a daily cycle up to 5% fluctuation where the minimum is reached at 6:00 and the maximum at 16:00 (UTC).

The Soil Moisture sensors (HydraProbe and 3 Segment GroPoint) come Factory-calibrated for most agricultural soils. The probes were initially calibrated in fine sand, as this provides an easy to reproduce reference point. For this reason, there may be slight differences between the readings given by the sensor and the actual moisture content due to differences in the measured soil's dielectric constant. These differences are generally small, on the order of a few percent.

7.3.3 Vegetation sampling

As it has been mentioned, two years before the campaign, a 50 cm thick layer of soil was added. Due to the origin of the added soil, the field shows different fertility indexes and soil characteristics, as texture and structure. The different indexes of fertility and soil characteristics are reflected on the vegetation parameter dispersion.

Vegetation sampling data has been taken according to the plan presented in [CIP]. Nonetheless, and considering the rapid stage evolution of the corn crop in the first part of the campaign, the programmed schedule was altered and the time between samples was reduced (Table 7.7).

Calendar of Soil samples extraction for gravimetric soil moisture determination has been altered because of two main reasons: firstly, the field has been drip irrigated so a uniform Soil Moisture along the field was assumed. Secondly, two data logger units with 8 soil moisture sensors have been deployed along the field, four of them were capable of measuring the three segments (0-15 cm, 15-30 cm and 30-45 cm).

LAI and Plant Water Content	17/7/2020 - 24/7/2020 - 31/7/2020 - 7/8/2020 – 14/8/2020 21/8/2020 - 27/8/2020 - 4/9/2020 - 10/9/2020 – 18/9/2020 28/9/2020 - 2/10/2020 - 23/10/2020
Gravimetric Soil Sample ext.	17/7/2020 – 27/7/2020 – 10/8/2020 – 24/8/2020 – 5/10/2020

Table 7.7. Calendar of Leaf Area Index, Plant Water Content and Soil Moisture Sampling extraction. Dates are in day/month/year

(a)


(b)


(c)


(d)

Figure 7.8. The field was prepared for sowing on 25 June (a) and 26 June 2020 (b). Corn was 20 cm height on 20 July (c) and was fully grown on 26 August 2020 (d).

7.3.3.1 Plant density

Plant Density has been obtained according to the sowing procedure. Plants were sowed in rows, 75 cm far from each other, with a distance between seeds of 15cm.

7.3.3.2 Planting row direction

Planting Row Direction for corn was forced by the sowing method (Figure 7.8), and it was parallel to the radar aperture movement.

7.3.3.3 Biomass and crop phenological stage

Due to the reduced dimensions of the radar scenario, special care had to be taken to ensure that the method of biomass measurement did not alter the radar reflectivity.

As it has been mentioned, vegetation water content (Figure 7.9) and plant phenology staging have been calculated sampling biomass from randomly selected areas. Several elements were cut and placed in sealed bags. They were weighted before and after drying in a thermally controlled oven.

Photographs of some representative plants were taken for phenological stage identification. The sampling frequency was adjusted according to the crop evolution.

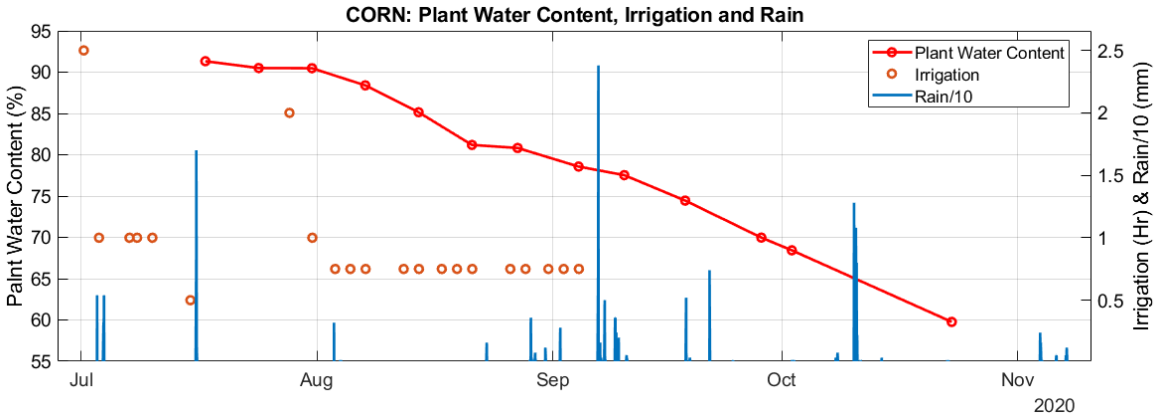

Figure 7.9. Plant Water Content in % (left axis), irrigation in hours and Rain/10 (right axis) for corn crop

Figure 7.10 Four phenological stages in the growing period of corn. (top left) 2 July 2020. (Top Right) 20 July 2020. (Bottom left) 28 August 2020. (Bottom right)

7.3.3.4 Size, height and orientation of main plant elements

The size of the main plant elements was obtained at the same time of Biomass and Crop Phenology. The orientation of the rows of plants was parallel to the radar aperture while the leaves spread around the stems.

The height has been obtained averaging the height measurements from 20 different plants, randomly selected, from different parts of the field. Height of each element is measured from ground to the flag leaf. The mean value of these 20 measurements is obtained and plotted (Figure 7.11).

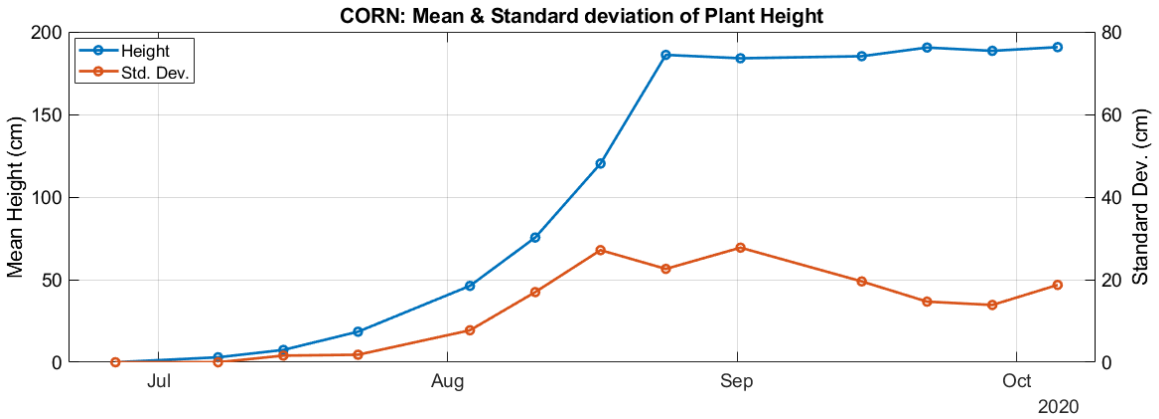

Figure 7.11 Corn crop height evolution since July 2020.

7.3.3.5 Leaf Area Index (LAI) determination

Due to the large surface of corn leaves, the method to measure the Leaf Area Index (LAI) has been different from the one used in Barley Campaign. The cutting strategy had to ensure that the plant density was not significantly affected in order to maintain the radar reflectivity. Several plants were cut from different sectors of the field, from near range to far range. The total leaf surface was calculated by means of image processing of the different scans of the leaves. For the first 2 workdays, the 100% of leaves were scanned and processed. The third workday, the 50% of the weighted leaves were scanned and processed. The rest of the workdays only 25% of the weighted leaves were processed. Measured LAI is shown in Figure 7.12 together with its standard deviation.

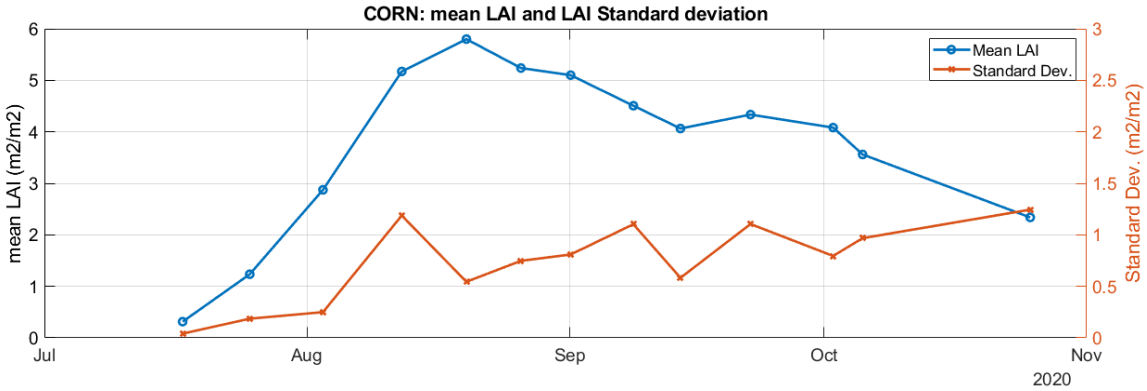

Figure 7.12 Mean Leaf Area Index and its Standard deviation for the corn crop.

7.3.3.6 Interception of precipitation

This measurement has been done only for corn crop. The procedure has been the following: before a rain event, two buckets are placed in the scenario, one between two plant rows and the other outside the field with no obstacles around it (Figure 7.13). The water content of both buckets are measured just after the rain event in order to minimize the error due to water evaporation. The ratio between internal to external gathered rain volumes is very irregular probably due to strong sensitivity of the internal bucket with respect to plants stems and leaves which act as a funnel with irregular efficiencies under the falling rain. A higher number of buckets under the canopy would be needed to obtain more consistent results.

Figure 7.13 Interception of precipitation. Two buckets were strategically deployed to measure the intercepted precipitation by comparing the accumulated water.

7.3.4 Meteorological parameters

The weather station that provided the meteorological parameters was the same one used in the barley campaign. This unit is installed at 25 m distance from the field under test, 4m above the field. It has been logging the main meteorological parameters since 7 May 2020 every 10 min: air temperature, barometric pressure, air humidity, wind speed, gust and direction, rain precipitation and others.

7.4 Results

7.4.1 Backscattering evolution of Corn

After sowing, the last week of June shows a backscattering similar to the one measured in the first days of the barley campaign since in both cases rough bare soil can be considered. Figure 7.14 shows the near-range part of the field backscattering, including cumulated millimetres of rain measured every 10 min with the HydroSoil *in-situ* meteorological station, minutes of irrigation and the measurements of the Near-Range group of 4 soil moisture probes. As expected, the impact of rain showers or irrigation is an increase in radar backscattering in all polarizations. Cross-polar backscattering levels are about 10 dB below the Co-polar levels. This difference is quickly reduced down to 6-7 dB with the growth of corn. Figure 7.15 provides additional information of interest such as Crop height, Leaf Area Index and Plants Water Content. The increase of backscattering levels, especially the cross-polar channels is remarkable in the growth phase from July to end of August. In September-October the crop reaches maturity and stops growing.

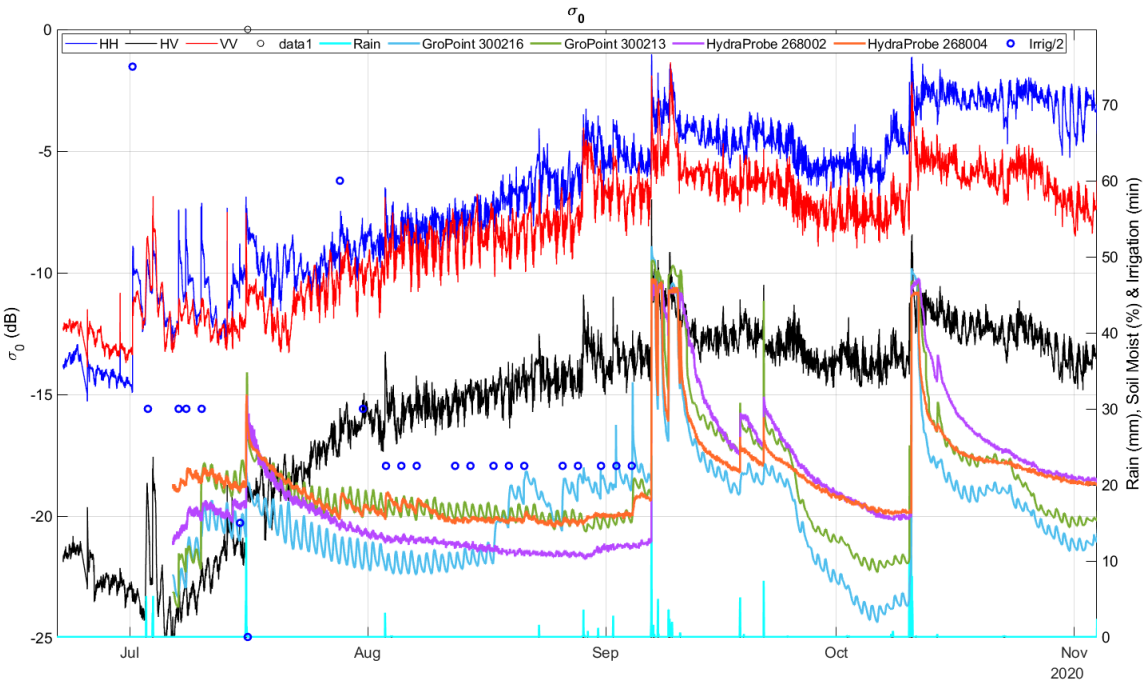

Figure 7.14 Time series of backscattering coefficient (σ_0) of corn crop for VV, HH and HV channels for 57° average incidence angle (55.2 °to 59.1 °) including rain intensity, irrigation times and measured soil moisture with a) GroPoint 300216 and b) Hydraprobe 268302 probes between irrigation lines and c) Gropoint 300213 and d) Hydraprobe 268304 probes close to the irrigation lines.

The backscattering generally decreases in this period since the plants lose water content and leaf area as it can be seen in Figure 7.16. As opposed to the barley case, light rain showers have only a noticeable impact in the first weeks, which is consistent with the expected opacity of a corn field. Very intense rain however, produces a significant increase of backscattering in all polarisations. The initial positive co-polar σ_{VV}/σ_{HH} difference of about + 2 dB is quickly reversed with the crop growth with higher HH returns along the corn life cycle, especially at the end when leaves and ears decay to almost horizontal positions. As in the barley case, a strong daily backscattering ripple of 1 to 3 dB is observed.

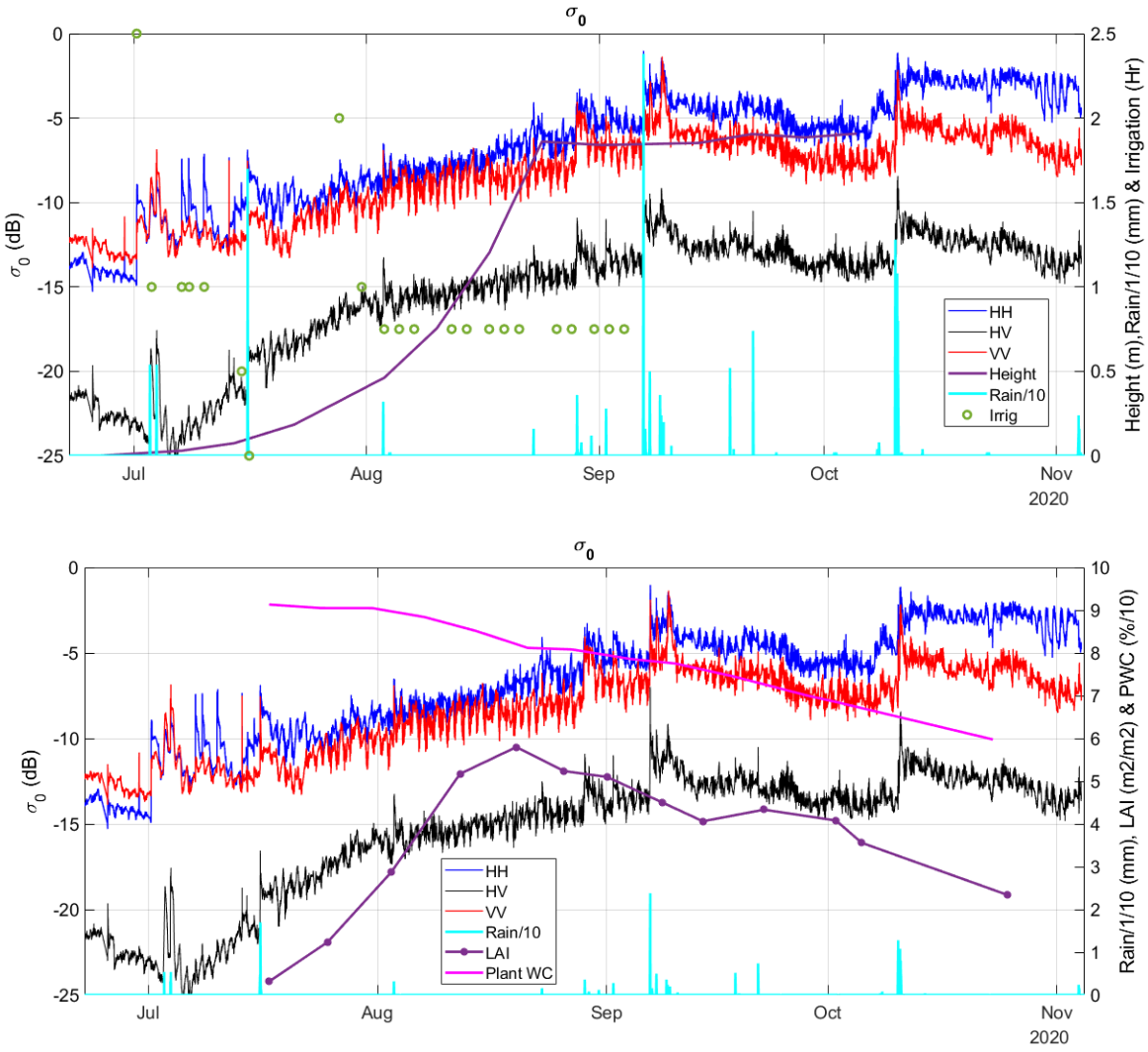

Figure 7.15 Time series of backscattering coefficient (σ_0) of corn crop for VV, HH and HV channels for 57° average incidence angle (55.2 °to 59.1 °) including rain intensity and: (Top) irrigation times and crop height evolution and (Bottom) Leaf Area Index (LAI) and Plant Water Content (PWC)

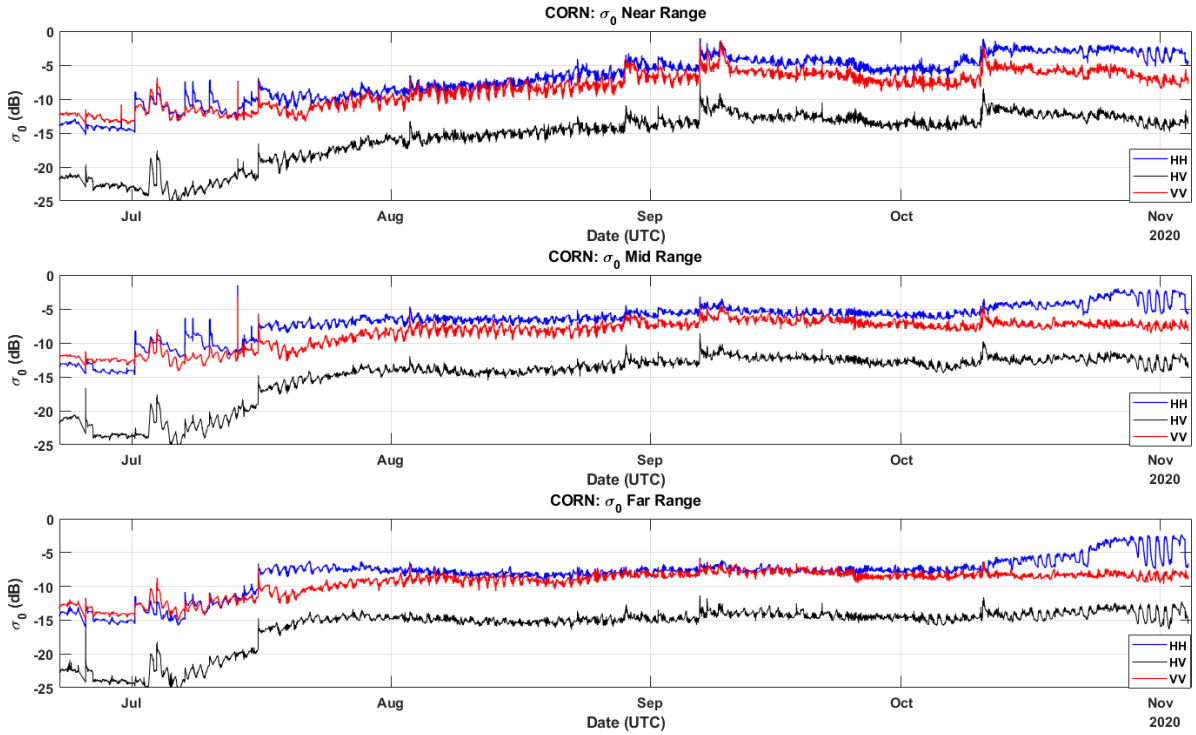

Figure 7.16 Time series of backscattering coefficient (σ_0) of corn crop at VV, HH and HV channels for incidence angles from 55.2 °to 59.1 °(Near Range), 59.1° to 63° (Mid Range) and 63 to 66.9° (Far Range).

7.4.2 Impacts of Rain and Soil Moisture on Backscattering

In the first days of the corn campaign, a similar impact of rain on radar backscattering was observed in both co-polar and cross-polar channels. In addition, the irrigation days in this period contributed to a remarkable increase in the observed backscattering. However, the backscattering sensitivity with respect to soil moisture quickly decreased with the crop growth. As a reference, Figure 7.17 reproduces the complete corn campaign evolution before detailing several events of particular interest.

In the first half of July, the radar backscattering is strongly depending on soil moisture as shown in Figure 7.18. This is a consequence of low crop density with short stems and small leaves size, in comparison with row separation as shown in Figure 7.19.

Rain showers result in a σ^0 rise, up to 3 to 4 dB in all polarisations, however irrigation events produced a higher backscattering increase in horizontal polarisation (2 to 3 dB) compared to 1 to 2 dB in VV, HV and VH. This probably results from the geometry of irrigation drip hoses deployed horizontally and parallel to the along-track direction.

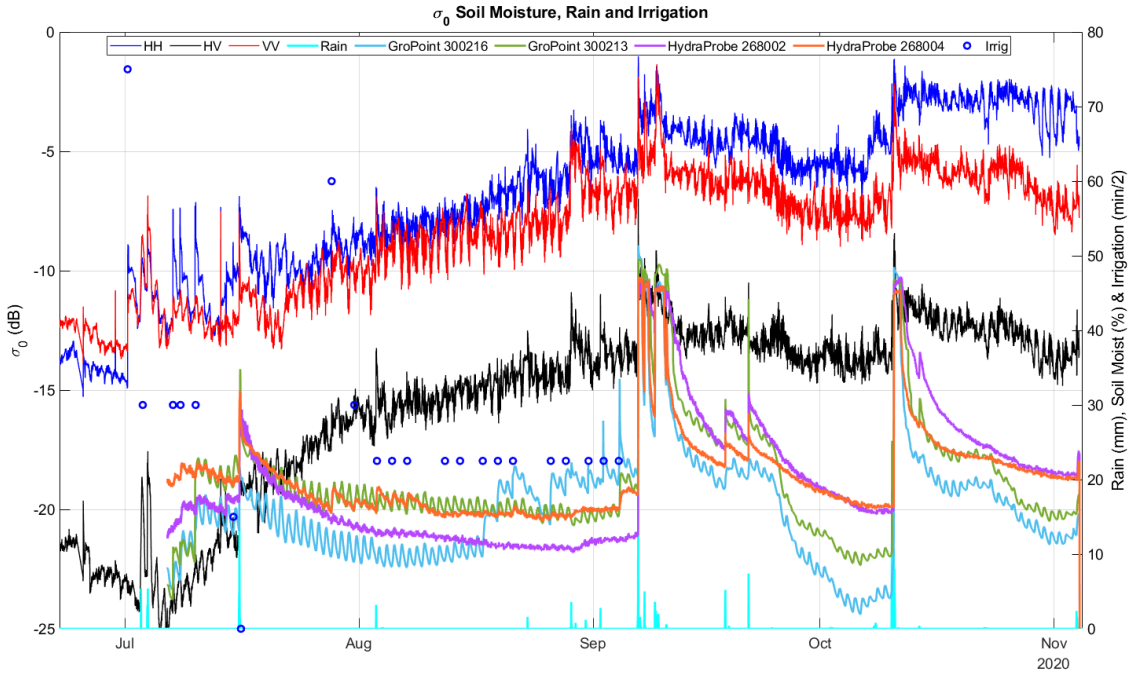

Figure 7.17 Corn campaign: complete time series of backscattering coefficient σ^0 at VV, HH and HV channels for Near Range incidence angles from 55.2 ° to 59.1 °

In August, the rapid growth of corn introduced significant backscattering changes as shown in Figure 7.20. The crop development can be observed in Figure 7.21 with a high volumetric density and well-hydrated leaves and stems. The strong volumetric scattering results in increased backscattering and a remarkable reduction of co-polar to cross-polar ratio from 10 to 6 dB approximately. The irrigation events do not increase significantly the backscattering levels which show a diurnal cycle of about 2 dB irrespectively of irrigation. However, rain showers, which were weak in August, resulted in slight increase of backscattering.

In September, the crop achieved its maximum height as depicted in Figure 7.15. Like in August, drip irrigation is not affecting measured backscattering, shown in Figure 7.22, in spite of the increase of soil moisture measured by the probes. However, a strong rain episode in 7 to 9 September wetting the crop and saturating soil moisture produced a measurable σ^0 increase. Lighter rain events on 1 and 18 September did not change backscattering magnitudes. In October, the corn crop reached maturity stage, losing leaves and trunks and thus a significant water content. As a result, radar backscattering decreased slightly in the second half of October in all polarisations except HH (Figure 7.24). The geometry of the plants changed significantly with both leaves and core ears declining from elevated angles and typical "V" shapes to more horizontal positions (Figure 7.25). A strong rain on 10 October increased backscattering notoriously probably due to water accumulation on the plants leaves, ears and trunks. In November, the plants have dried significantly as shown in Figure 7.26. However, the average backscattering levels were almost maintained in HH polarisation, although with a strong diurnal cycle, possibly because individual plant scattering reduction was compensated by lower Horizontal polarisation attenuation allowing a higher number of plants contributing to volume scattering mechanism in HH.

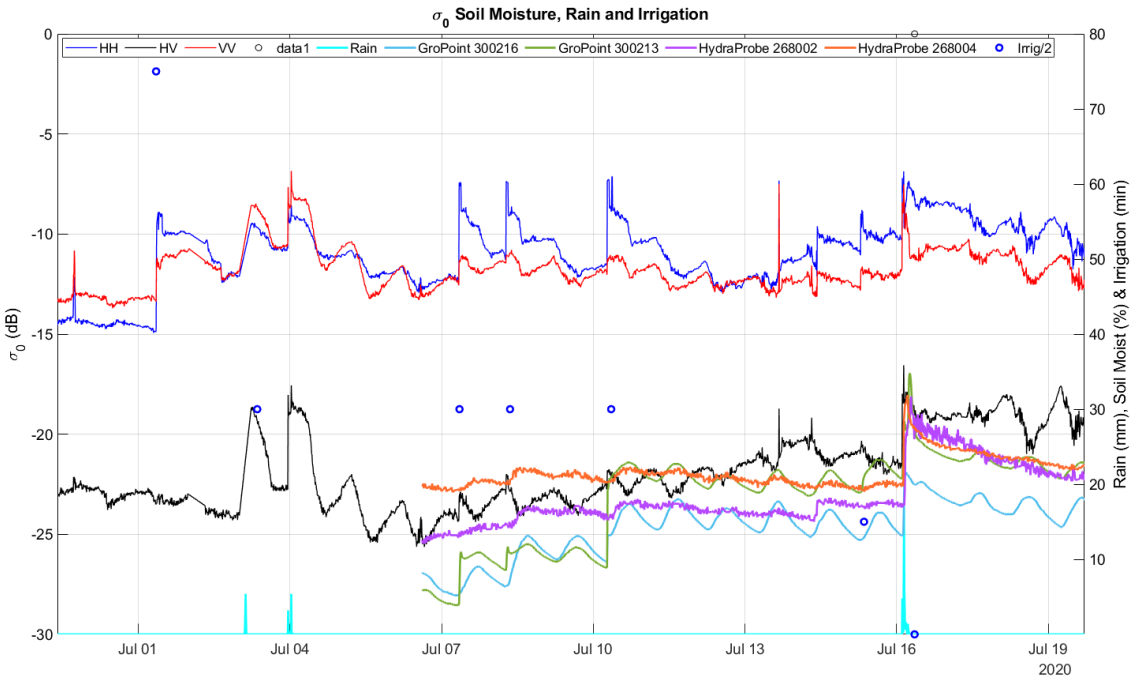

Figure 7.18 Expanded Near-Range view of corn backscattering changes induced by rain showers and irrigation on the first half of July.

Figure 7.19 Corn initial stage on 17 July.

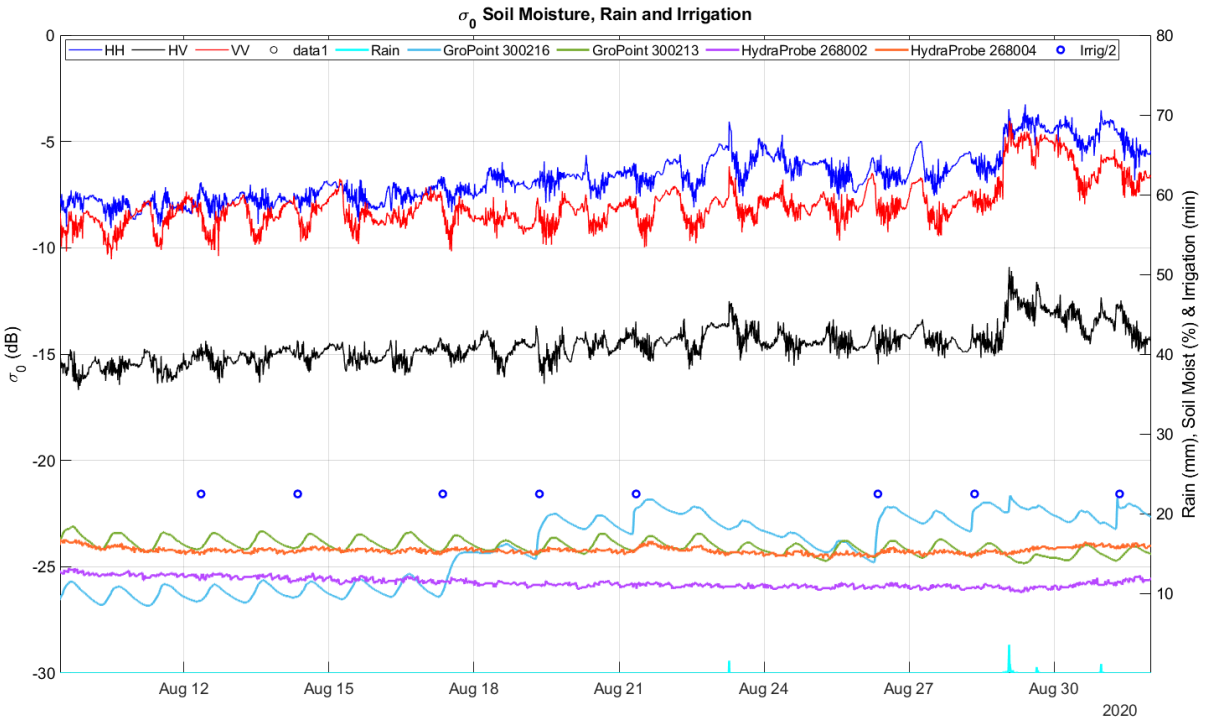

Figure 7.20 Expanded Near-Range Corn backscattering changes induced by irrigation and rain showers in the second half of August.

Figure 7.21 Corn crop on 11 August 2020.

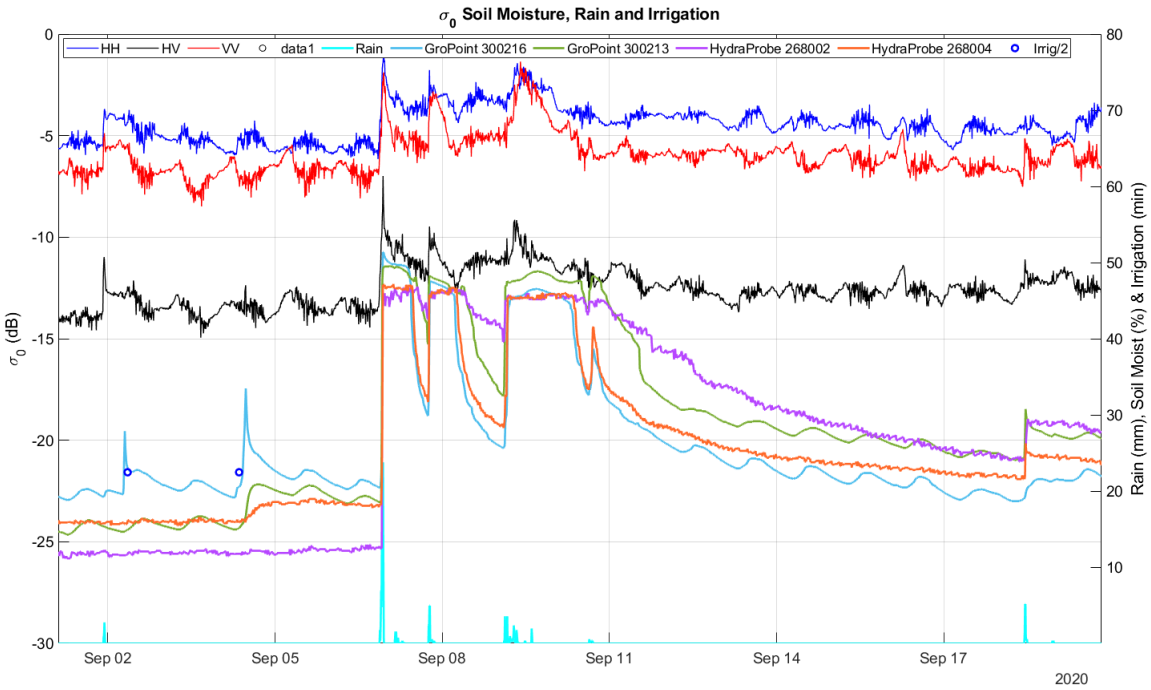

Figure 7.22 Expanded Near-Range view of Corn backscattering coefficient σ^0 in first half of September.

Figure 7.23 Corn crop on 16 September.

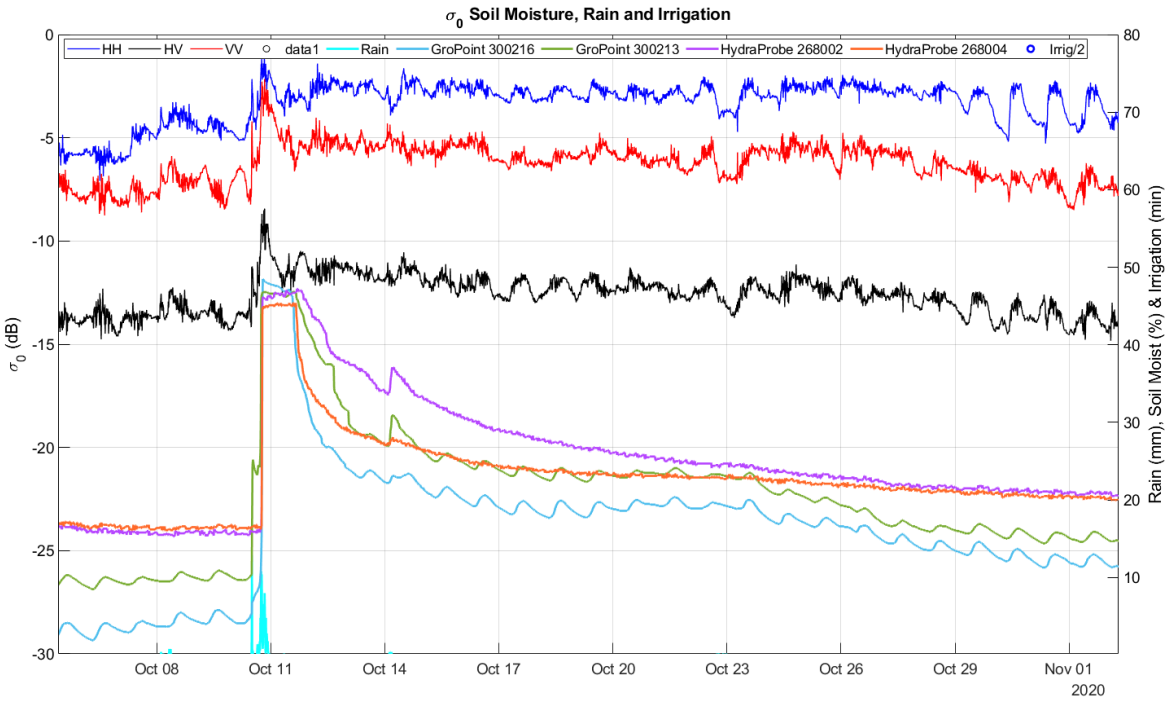

Figure 7.24 Close-up Near-Range view of corn backscattering coefficient σ^0 in the second half of October

Figure 7.25 Corn crop on 14 October.

Figure 7.26 Corn crop on 11 November 2020.

7.4.3 Backscattering diurnal cycle

As in the barley campaign, few dB diurnal backscattering cycle has been consistently observed in the corn campaign.

The corn diurnal cycle has some similarities and differences with respect to the barley campaign. Figure 7.27 shows, as a reference, the whole corn campaign backscattering evolution with evident diurnal cycles affecting all polarisations HH, VV, HV/VH. The plot includes also Rain Intensity, Irrigation times and Soil Moisture probes measurements. Additional detailed plots have been included, showing backscattering, Air Humidity, Soil Moisture and Rain Intensity in some periods of interest.

In July, the diurnal cycle in the co-polar channels is similar to the early stage of barley. The backscattering increases in the late night/early morning relaxing again along noon-afternoon hours as it is shown in Figure 7.28. Similar cycle amplitudes around 1.5 to 2.5 dB are observed in all polarisations. The fluctuations appear to be almost in synchronism in all polarisations, with occasional delays of HH and VV.

In August, usually a very hot and dry month in the Catalan costal area, the field was irrigated almost every 2 days except after rain showers, to supply the required water in the intense growth stage of the crop. This fact complicates the interpretation of backscattering changes, since diurnal water cycles induced by dew are mixed up with irrigation events. In the periods with no irrigation, for example 22-25 August, some correlation between humidity and backscattering can be observed although less consistent compared to earlier crop stages. The cyclic changes in HH, VV, HV/VH polarisations are generally very similar, with peak to peak amplitudes in the order of 2 dB.

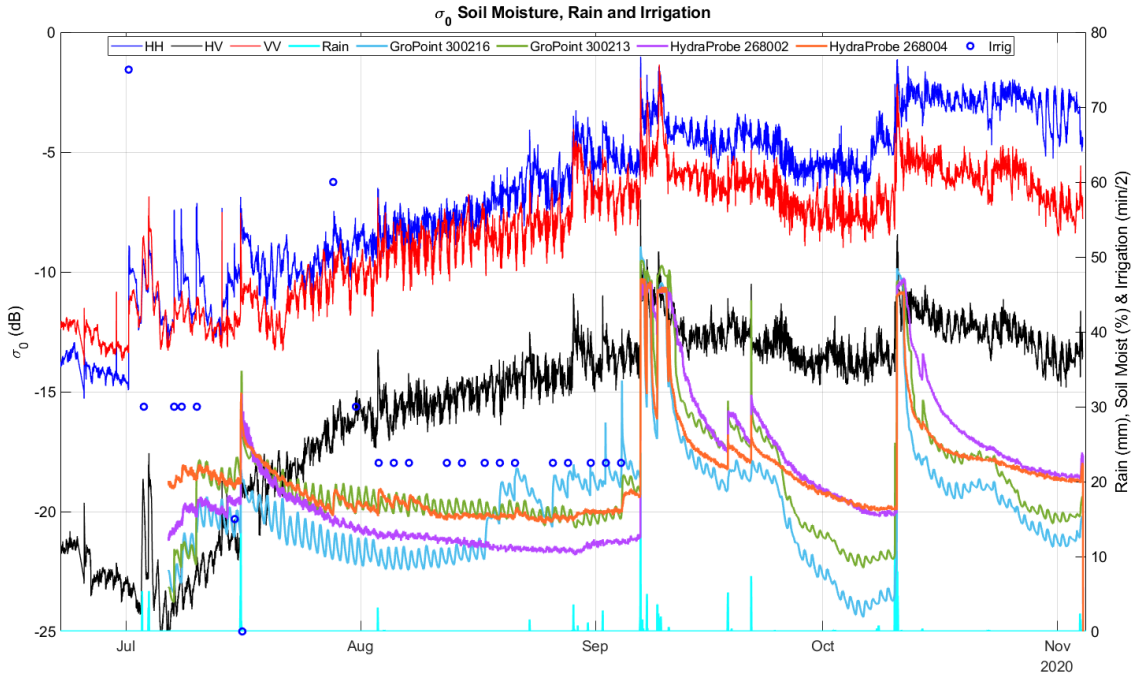

Figure 7.27 Time series of corn crop Near-Range backscattering coefficient along the whole campaign.

In late September, the crop is losing water content, reducing the attenuation and surface scattering, however, the backscattering levels in all polarisations presented in Figure 7.30 show very little decay probably due to higher volumetric scattering. The strong correlation between air humidity and backscattering is lost, sometimes radar backscattering decays slightly with humidity increase, which is opposite to what is observed in earlier stages. With 1.8 m height the crop is very sensitive to wind rise around noon and afternoon, the induced time decorrelation might contribute to the observed backscattering increase.

At the end of October, the crop is in senescence stage, very dry and with notorious changes in the shape and orientation of leaves tilted horizontally or downwards (see Figure 7.26). In this period, air humidity shows a typical diurnal cycle from 20 to 23 October, a relatively dry interval from 24 to 28, and cycling again every day from 29 to 2 November as shown in *Figure 7.31*. The influence of humidity changes on backscattering daily cycles becomes evident since backscattering stops cycling in the low humidity period from 24 to 28 October.

The correlation between air humidity and backscattering at the final crop stage end-October and beginning of November is negative: the humidity increase produces a notorious drop in radar backscattering in all polarisations. The fluctuations are particularly strong in HH polarisation with an amplitude of about 3 dB peak to peak at the end of this period. These strong backscattering cycles are produced by a loss of backscattering level in the intervals when the plants are expected to become wet, which seems counterintuitive.

A possible explanation is a dominant volumetric scattering mechanism at this dry stage that could be negatively affected by the increase of radar illumination extinction when the plants become wet. The relation between scattering and extinction (albedo), in the canopy might be determinant to stablish the positive or negative correlation between radar backscattering and air humidity observed in this campaign and in previous experiments. A recent study has pointed out the need to review the role of extinction in radar remote sensing models for vegetation [28].

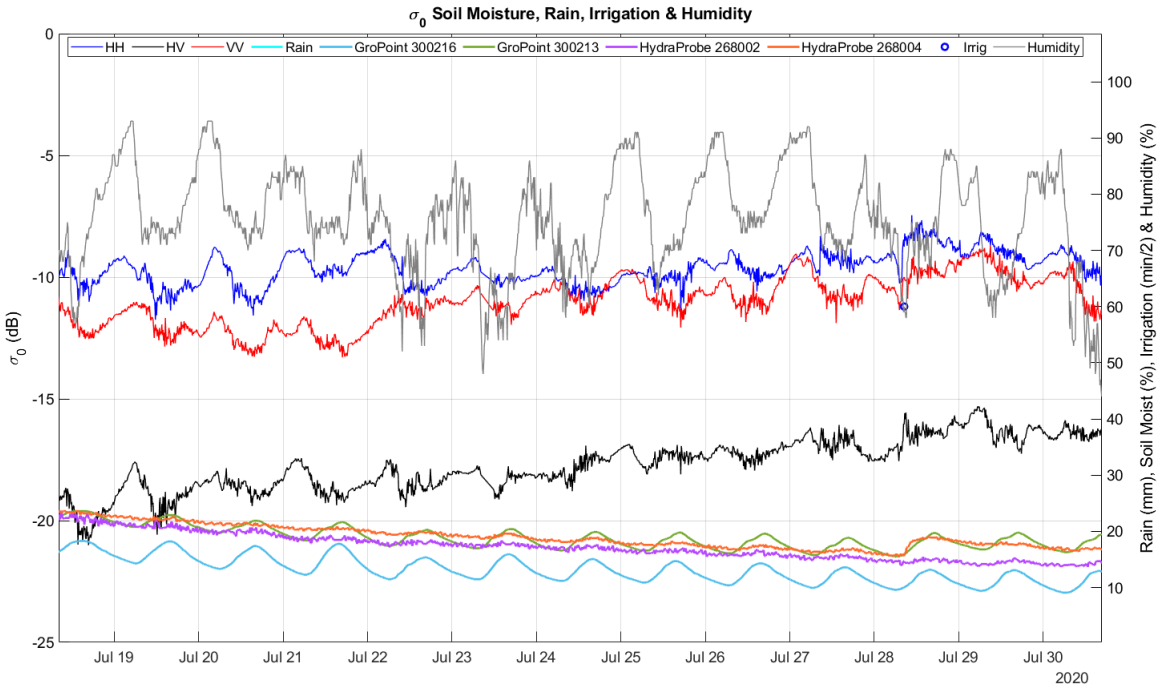

Figure 7.28 Expanded view of corn Near-Range backscattering coefficient σ^0 in late July.

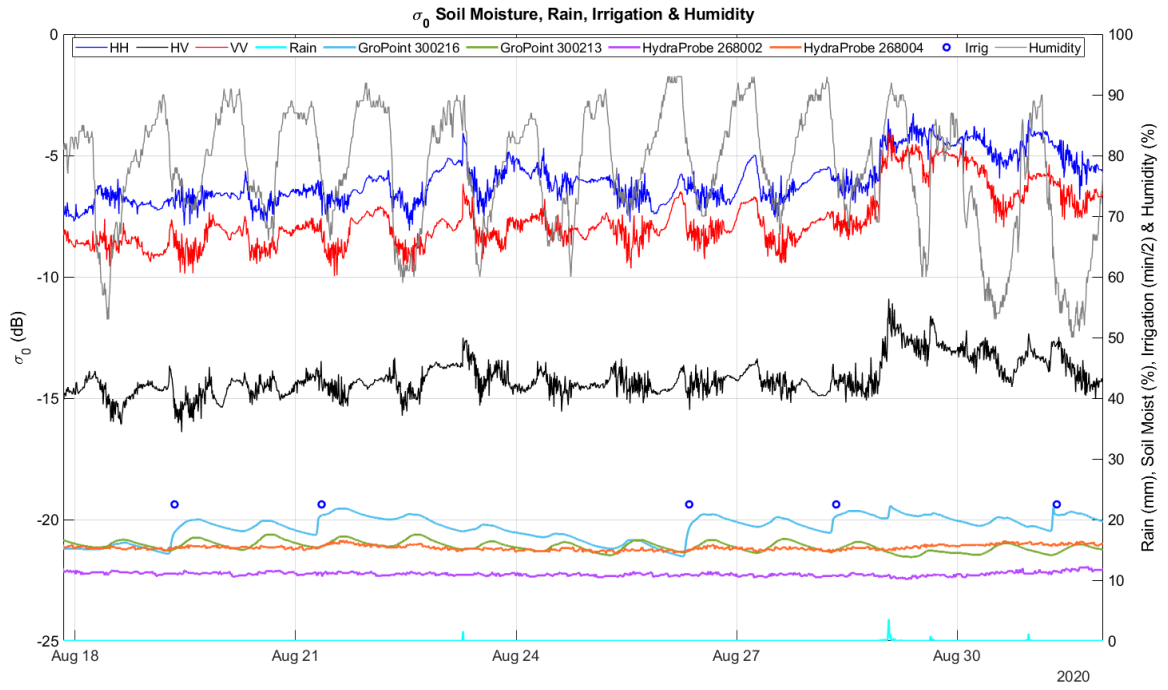

Figure 7.29 Expanded view of corn Near-Range backscattering coefficient σ^0 in late August.

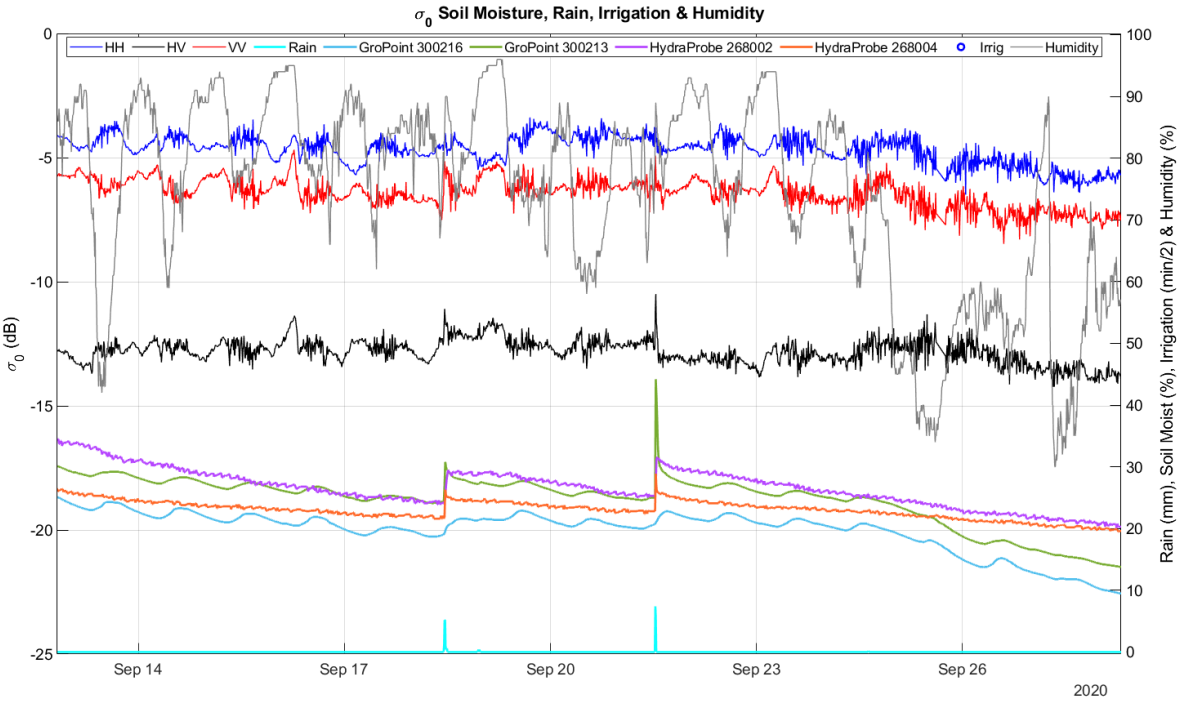

Figure 7.30 Expanded view of corn Near-Range backscattering coefficient σ⁰ in late September.

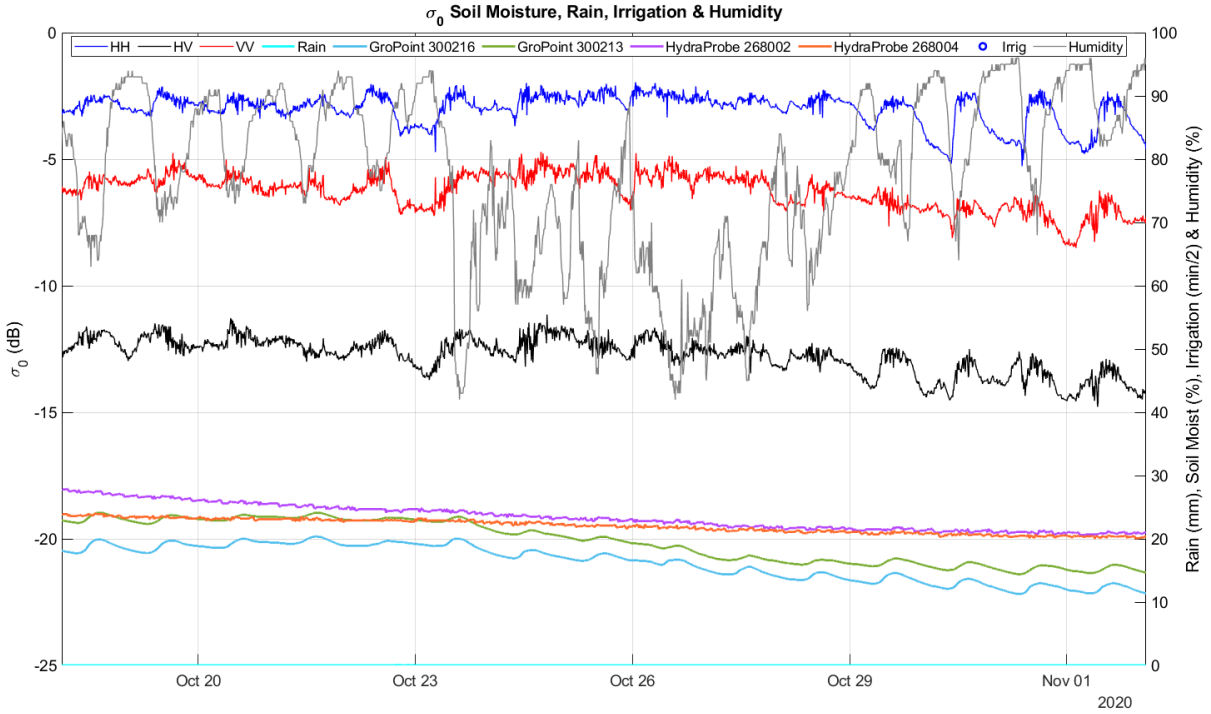

Figure 7.31 Expanded view of corn Near-Range backscattering coefficient σ⁰ in late October.

7.4.4 Impact of the diurnal plant water content cycle on radar backscattering

The assessment of the ability of radar backscattering data to observe crop physiology (movement of water, controlled by vegetation, in the soil and plant during the day) for corn crop is based on a single day campaign, 16 September 2020. In this day, as in barley crop campaign, fresh and dry biomass destructive measurements were carried out every 2 hours during 12 h, from 06:00 to 18:00 UTC (8:00 to 20:00 local time). In parallel, radar, weather and soil moisture measurements were taken. Different plants were cut and segmented to extract the Plant Water Content evolution of these segments during the day. Slight changes in Plant water content (PWC) are seen Figure 7.32. As expected, first segments, the ones close to the ground, show a higher water content compared with the rest. The PWC of the segments shows an oscillating behaviour.

Backscattering coefficient (σ^0) of the different polarimetric channels for three different areas of the field (near, mid and far range) is evaluated for corn crop (Figure 7.33 to Figure 7.38). It has to be noted that, as a large-dense crop, significant backscatter from vegetation volume has to be considered.

For corn, a change in reflectivity is seen between 6:00 and 8:00, slightly advanced respect an increase of PWC index for the lowest segments of the plant. Since magnitude backscattering changes are very small, this assessment is being complemented with an on-going evaluation of average phase drift obtained from the complex coherence averaged in the near, mid and far range field areas.

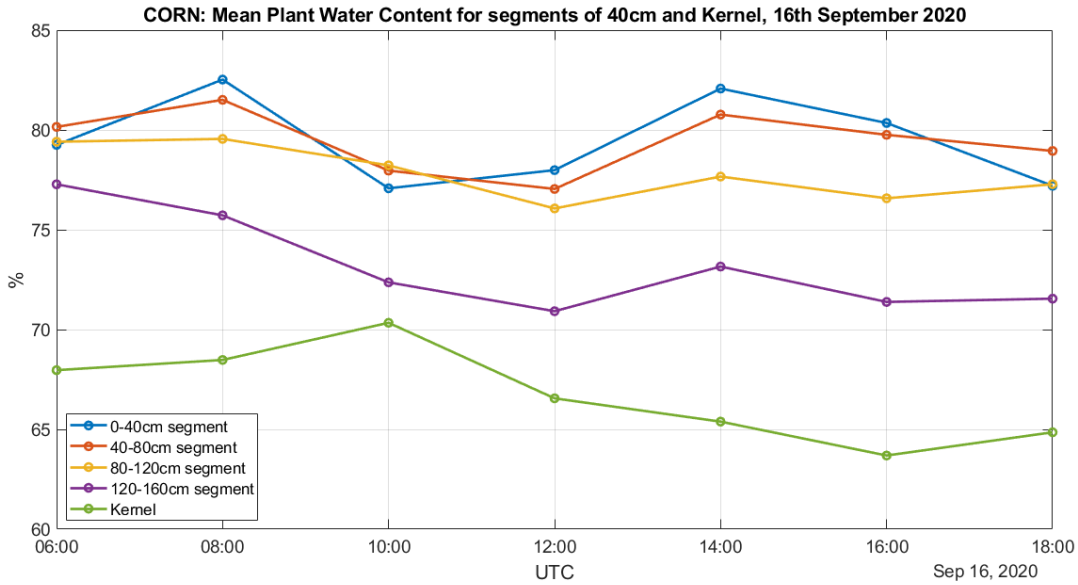

Figure 7.32 Time series of plant water content for four different segments and kernels of the plant.

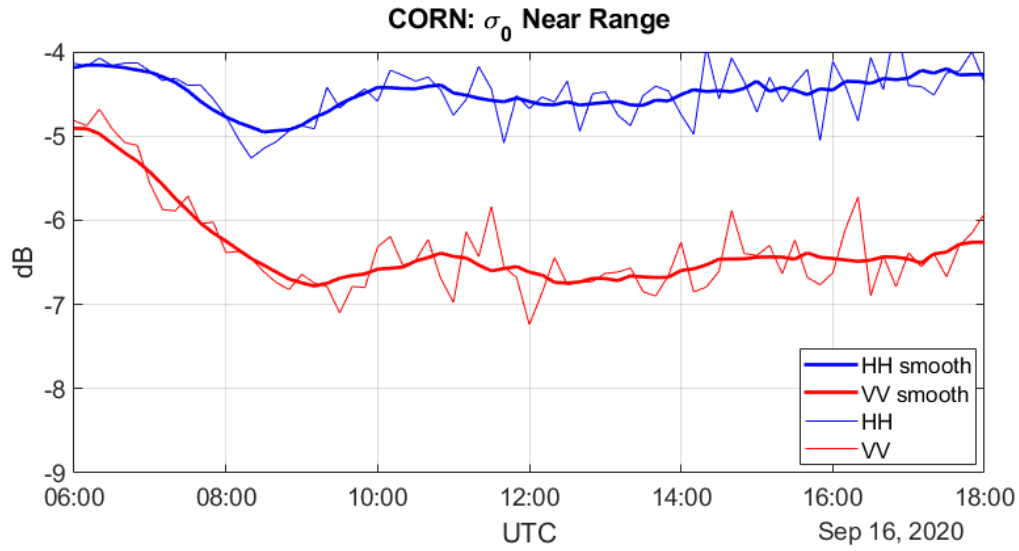

Figure 7.33 Time series of backscattering coefficient σ_0 of the Co-polar Channels for Near Range.

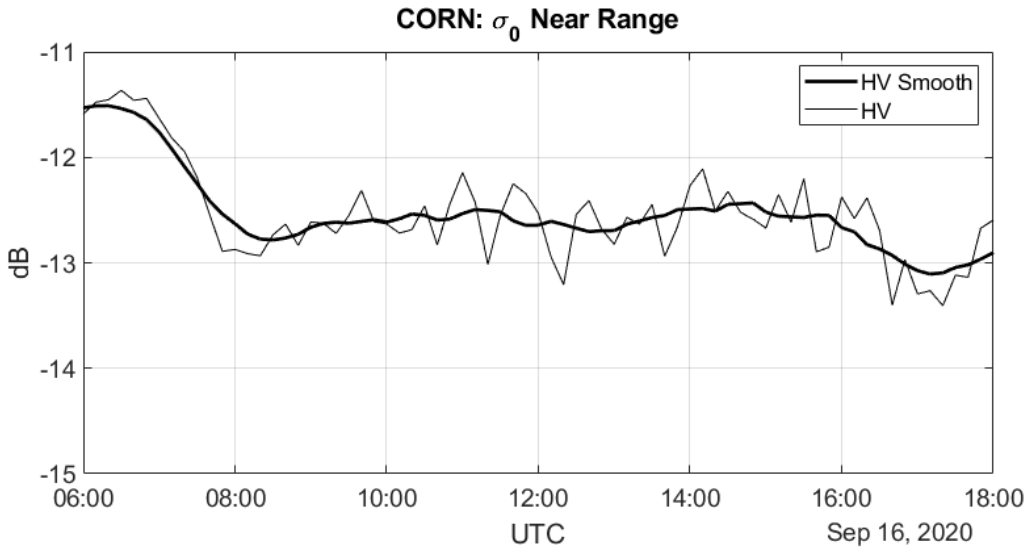

Figure 7.34 Time series of backscattering coefficient σ_0 of the Cross-polar Channel for Near Range.

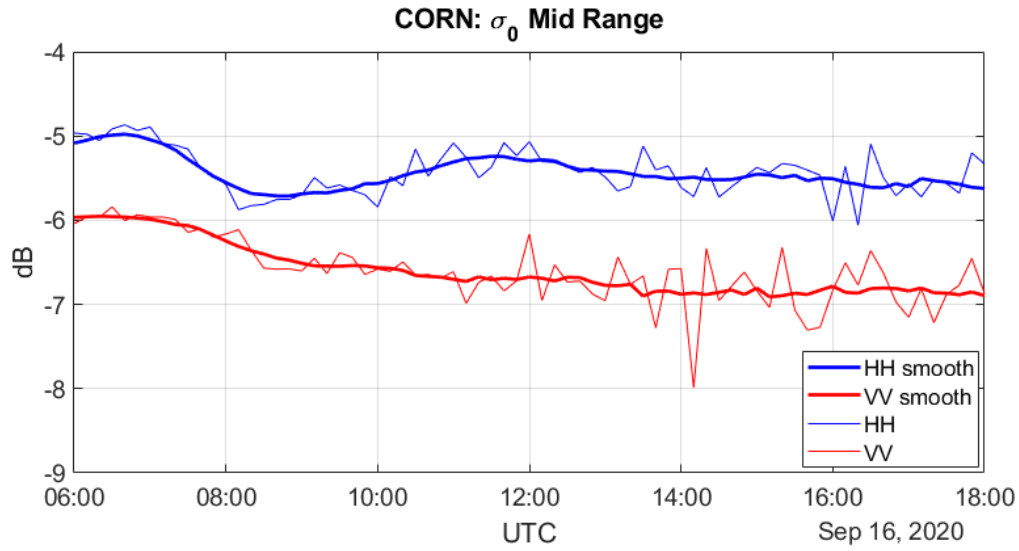

Figure 7.35 Time series of backscattering coefficient of the Co-polar Channels for Mid Range.

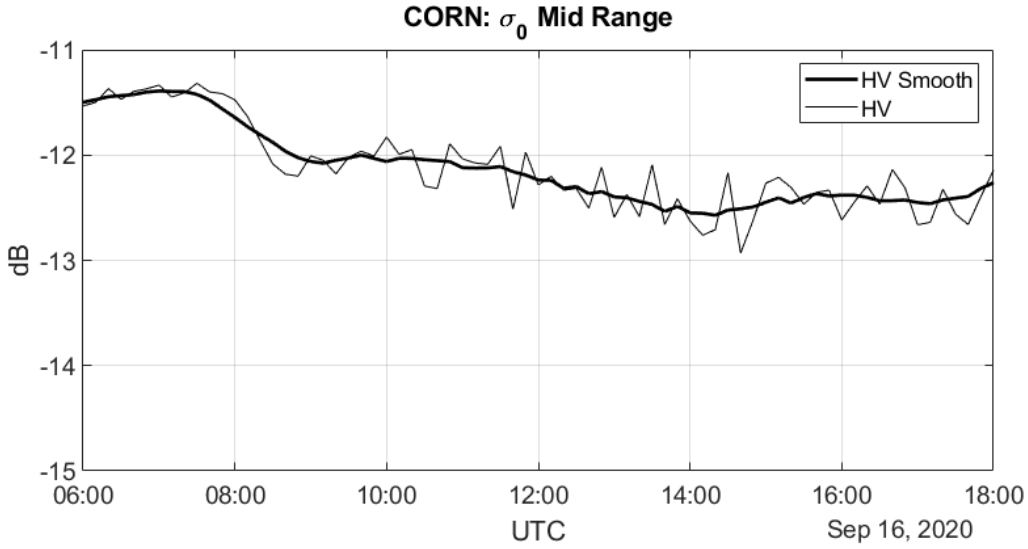

Figure 7.36 Time series of backscattering coefficient σ_0 of the Cross-polar Channel for Mid Range.

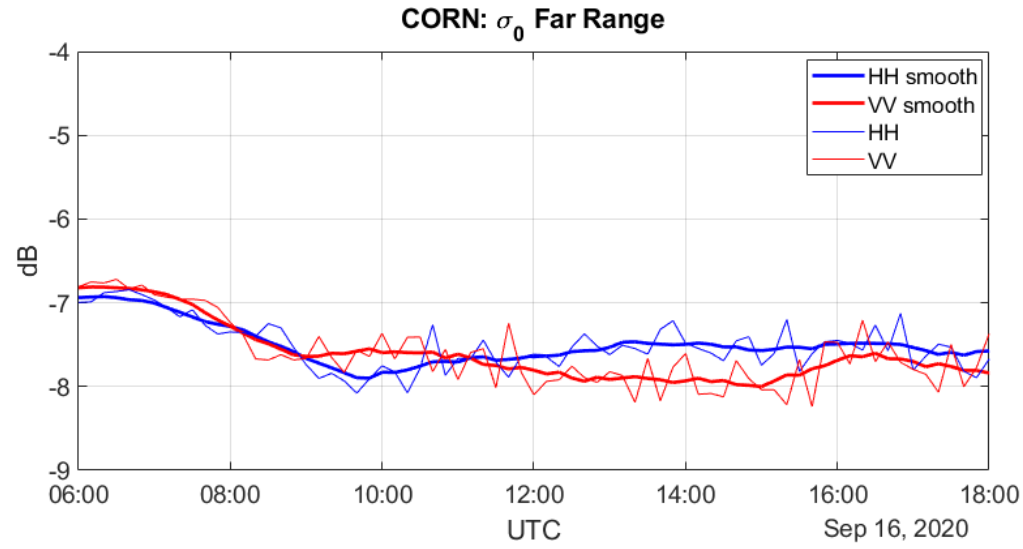

Figure 7.37 Time series of backscattering coefficient σ_0 of the Co-polar Channels for Far Range

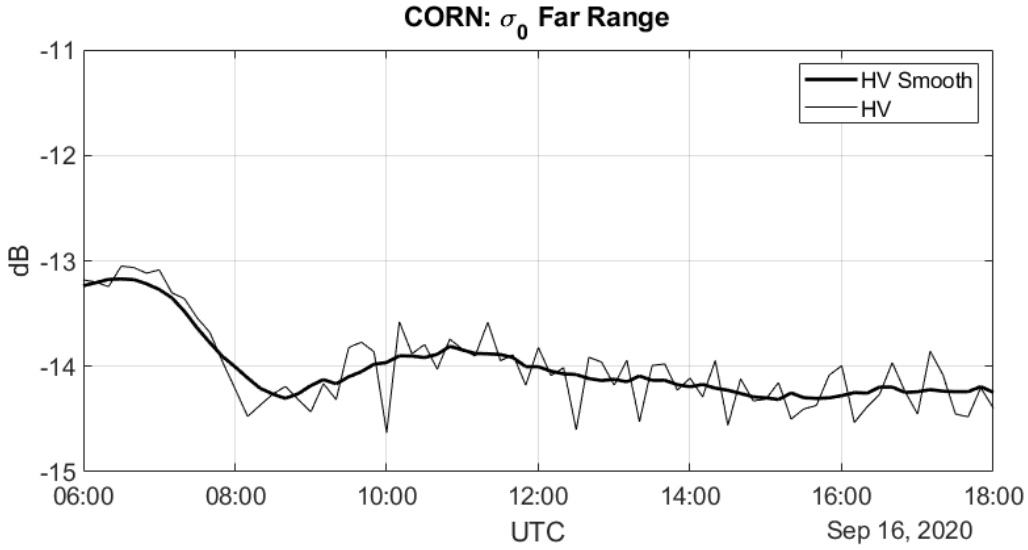

Figure 7.38 Time series of backscattering coefficient σ_0 of the Cross-polar Channel for Far Range

7.4.5 HH-VV decorrelation with surface parameters

Figure 7.39 and Figure 7.40 show the time series of hh-vv correlation of the whole corn crop campaign including rain intensity-crop height evolution-irrigation and LAI-crop height evolution respectively. A behaviour similar to barley can be observed. When vegetation emerges in the field, the correlation decreases significantly. Bearing in mind the growth speed of the corn, low correlation values are obtained quickly. A dependence between the irrigation process and the co-polar decorrelation is not observed. When the corn dries (Figure 7.26) at the end of the measurement campaign, a double bounce component appears between corn and soil, which increases the co-polar correlation slightly.

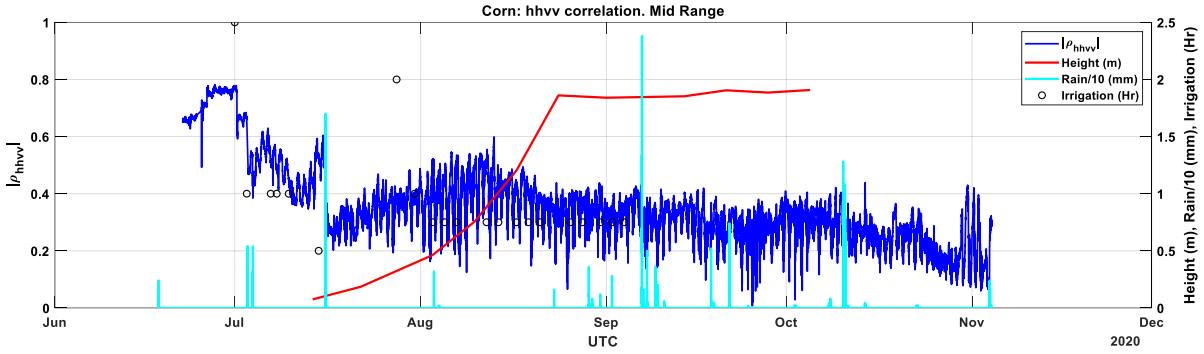

Figure 7.39 Time series of hh-vv correlation of corn crop for Mid Range: incidence angles (59.1 ° to 63 °) including rain intensity (cyan), crop height evolution (red) and irrigation times (black circles)

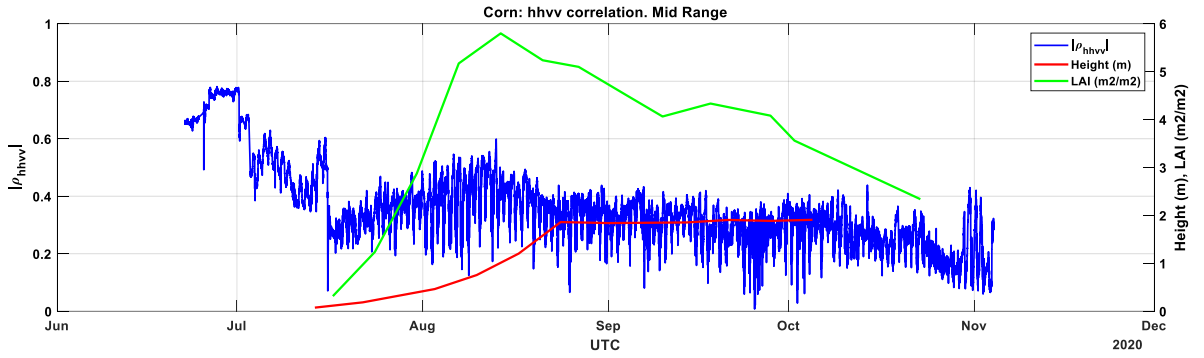

Figure 7.40 Time series of hh-vv correlation of corn crop for Mid Range: incidence angles (59.1 ° to 63 °) including crop height evolution (red) and LAI evolution (green)

7.4.6 Phase & Coherence changes

To study the crop height's influence over the coherence, three different time periods for corn crop, with different growing-stages, have been selected:

- 28 June 2020 – 04 July 2020. Bare soil stage
- 25 July 2020 – 31 July 2020. Plant height ~40 cm, where the plant already started growing at fast rate
- 13 August 2020 – 19 August 2020. Plant height ~1 m, corresponding to a developed stage, still growing fast.

As in the study of phase and coherence changes for barley crop, these time-intervals have been selected avoiding rain events, to avoid rain alterations on coherence.

7.4.6.1 Short term and long-term coherence evolution. Impact of crop height

From Figure 7.42 to Figure 7.46, the magnitude of the coherence is represented for the different time intervals selected to study as in 6.4.6. In all the cases a diurnal cycle can be observed and, as expected, depending on the crop growth stage, the coherence decay changes.

Looking at the figures Figure 7.42 to Figure 7.46, some complementary conclusions to the ones for barley crop campaign (6.4.6.1) can be extracted. For the bare-soil stage, the results are much more coherent, with its module having an acceptable value until around 3 days and a half have passed. At this time the coherence decays drastically, and the reason is that there was an irrigation event that produced a big change in the reflectivity of the soil, producing a loss of coherence.

When the plant height is around 40 cm, the coherence is lost faster than in the bare soil case. Nevertheless, it still has values that can be considered as coherent until 2 days after the master image acquisition. In this case, the effect of the irrigation event is not as evident; although we see a decay of coherence right after irrigation, as the coherence value was already low, it is not so relevant.

In the case where the plant reaches around 1 m height still growing fast, a fast drop of the coherence is clearly observed, with almost total decorrelation after 12 h interval from the master image. In this case, the irrigation impact on coherence is not visible, because of two main reasons: when it does happen the coherence already is very noisy and low; and as the crop height is already quite high, the irrigation over the field itself is blinded by the plant signal extinction due to both scattering and absorption mechanisms.

Furthermore, in the two crop cases, the influence of wind can be observed with a higher coherence decays and instability when the wind is stronger, typically around noon and afternoon. The coherence increases again when wind stops (mostly during the night). As expected the wind impact is proportional to plant height and density.

From these results, present models relating crop height and radar observations can be reviewed to study possible improvements that could be exploited in present and future missions considering the limitations in revisit time and local times of satellite ascending and descending passes.

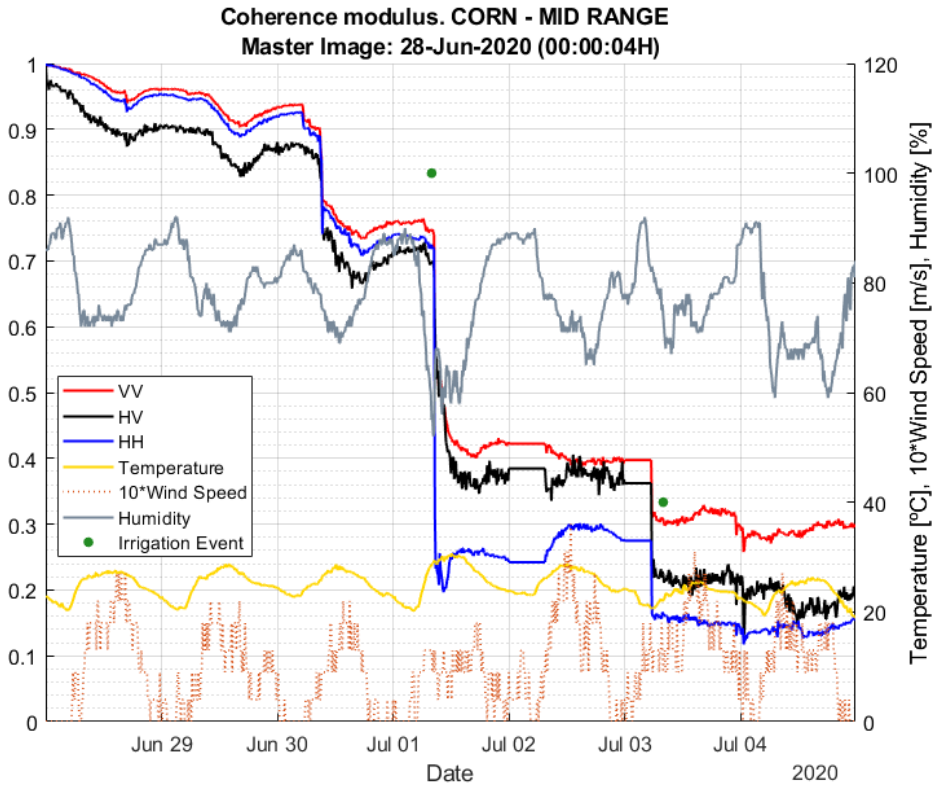

Figure 7.41 Modulus of the coherence. Corn campaign, bare soil. Only 1 master image used.

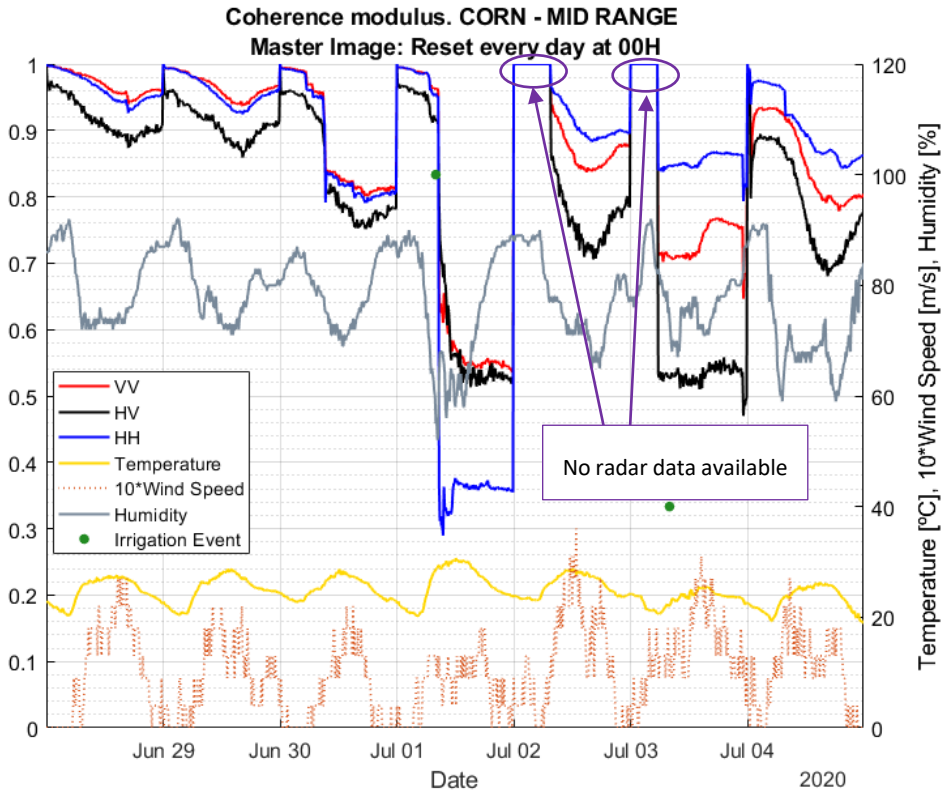

Figure 7.42 Modulus of the coherence. Corn campaign, bare soil. Master image reset every 24 h. Notice that for the first hours of 2 and 3 July no radar data was available, so the values for these periods are irrelevant.

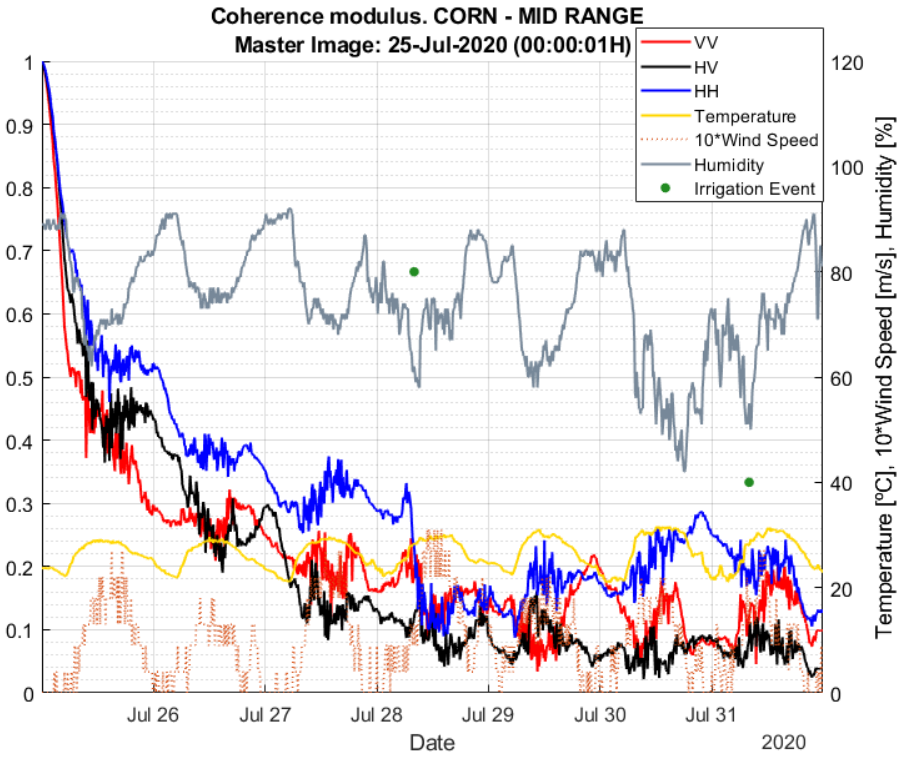

Figure 7.43 Modulus of the coherence. Corn campaign, plant height ~40 cm. Only 1 master image used.

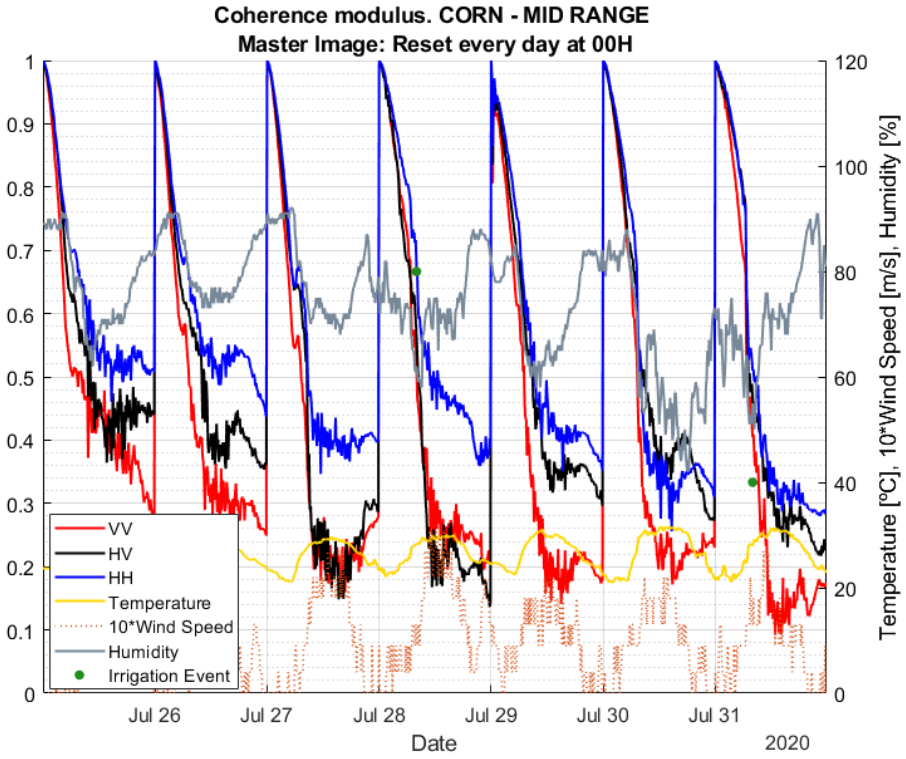

Figure 7.44 Modulus of the coherence. Corn campaign, plant height ~40 cm. Master image reset every 24 h.

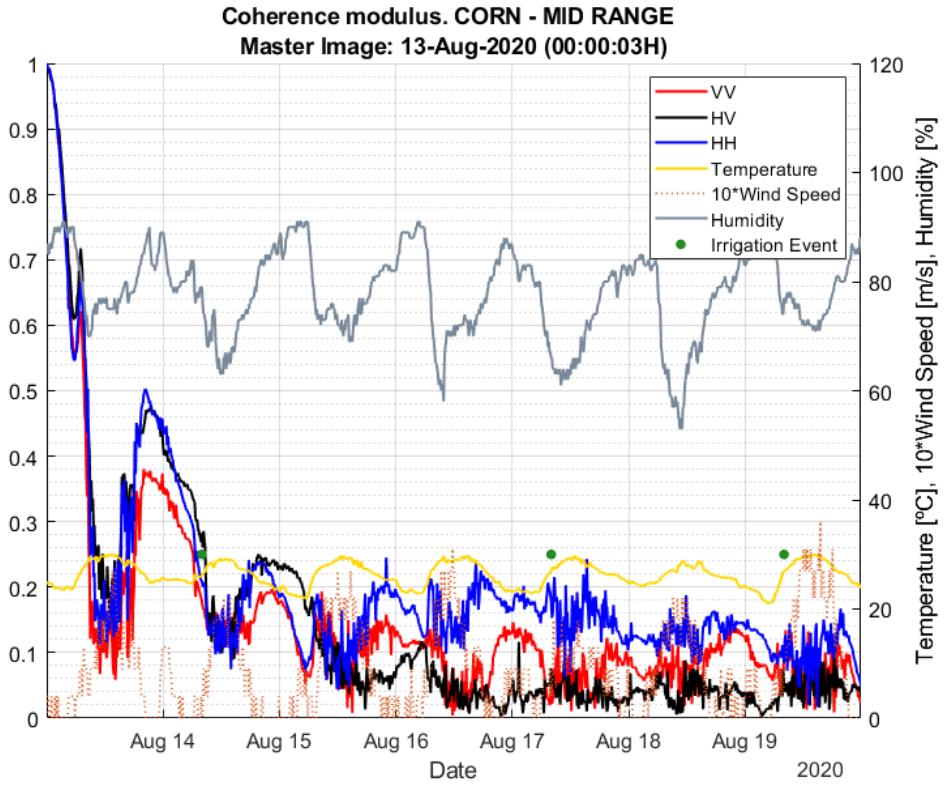

Figure 7.45 Modulus of the coherence. Plant height ~1 m. Only 1 master image used.

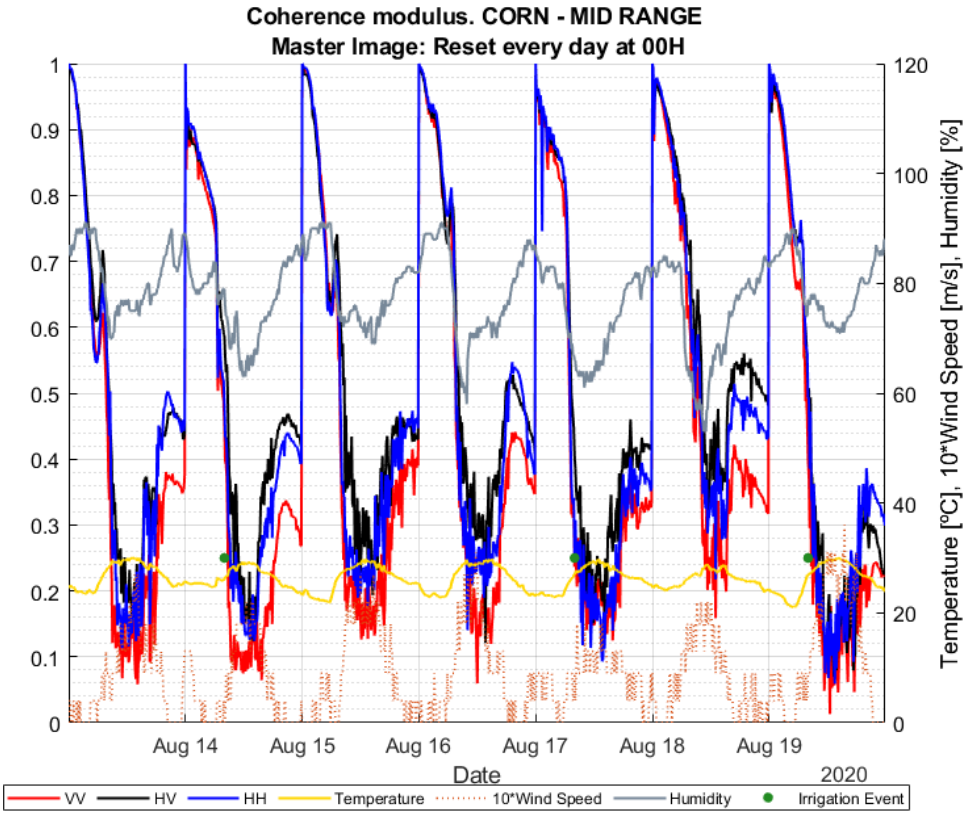

Figure 7.46 Module of the coherence. Plant height ~1 m. Master image reset every 24 h.

7.4.6.2 Multitemporal Coherence Matrix. Impact of time baseline length

Figure 7.47 shows the coherence between images with a temporal baseline of 10 minutes (k=1 diagonal matrix) of the whole corn crop campaign for HH, VV, HV and VH channels including rain intensity, irrigation time and crop height evolution. A similar behaviour to barley can be observed, where coherence presents very high values except for those rainfall events and irrigations. As vegetation grows, coherence fades appear associated with variations in the wind in the diurnal cycle. As seen also in barley, the fading of coherence is associated with an increase in wind speed that occurs during the day and at night, in the absence of wind, coherence returns to its high values. In Figure 7.48 an event of strong wind throughout September 25 can be observed, where a very important loss of coherence is appreciated during the whole day. A similar analysis is obtained using a temporal baseline of 1h and 4h as can be seen in the Figure 7.49, Figure 7.50, Figure 7.51 and Figure 7.52. A loss of coherence is observed as the temporal baseline increases.

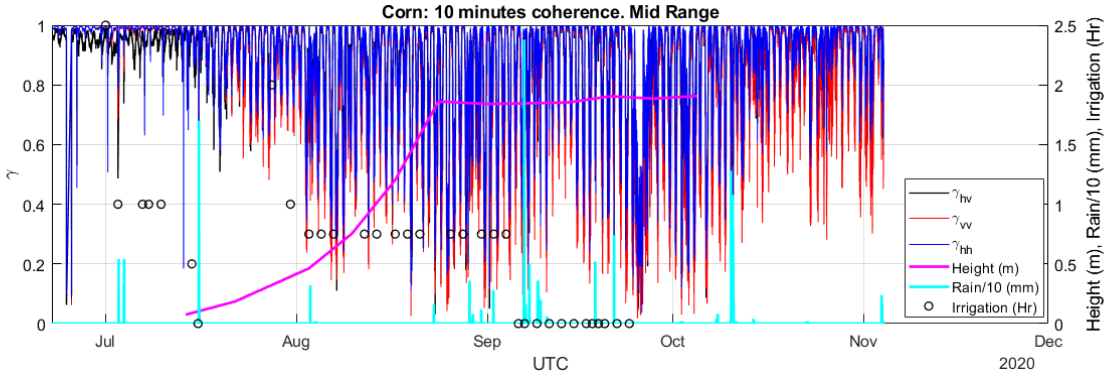

Figure 7.47 Time series of 10 minutes temporal baseline coherence of the whole corn crop campaign for HH, VV, HV and VH channels for Mid Range: incidence angles (59.1° to 63°) including rain intensity (cyan) and crop height evolution (magenta) and irrigation times (black circles).

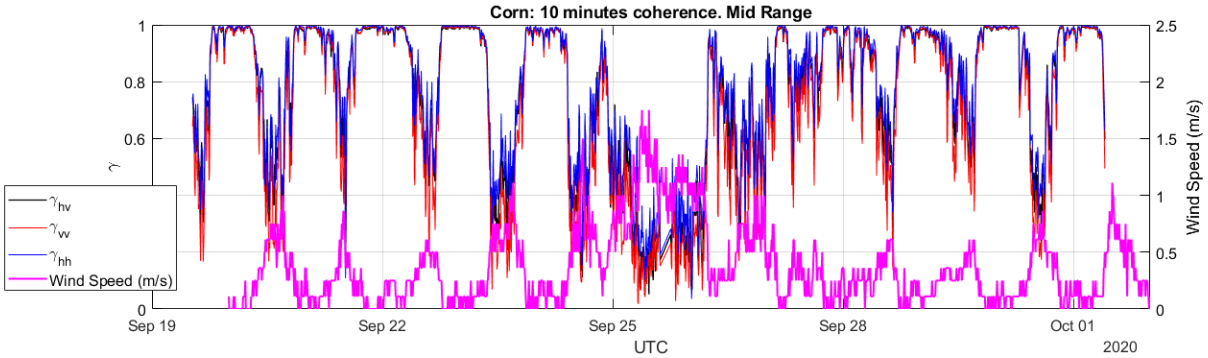

Figure 7.48 Time series of 10 minutes temporal baseline coherence of corn crop between September 20 and October 2 for HH, VV, HV and VH channels for Mid Range: incidence angles (59.1° to 63°) including wind speed (magenta).

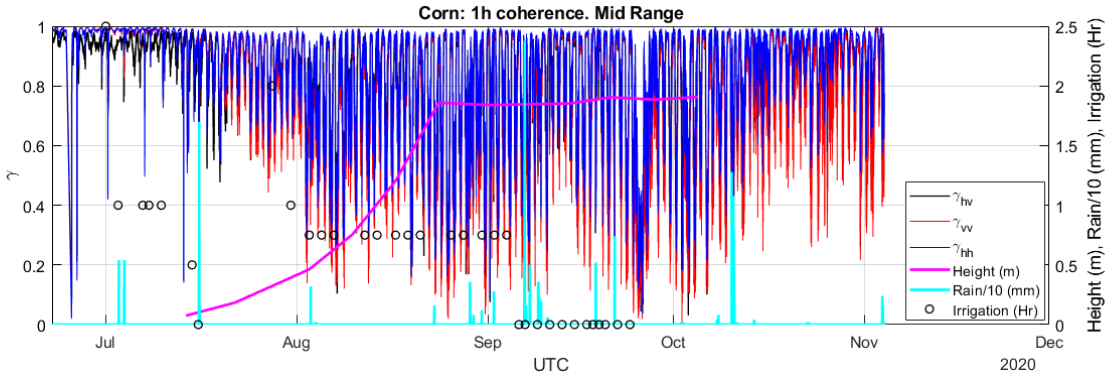

Figure 7.49 Time series of 1 hour temporal baseline coherence of the whole corn crop campaign for HH, VV, HV and VH channels for Mid Range: incidence angles (59.1°to 63°) including rain intensity (cyan) and crop height evolution (magenta) and irrigation times (black circles).

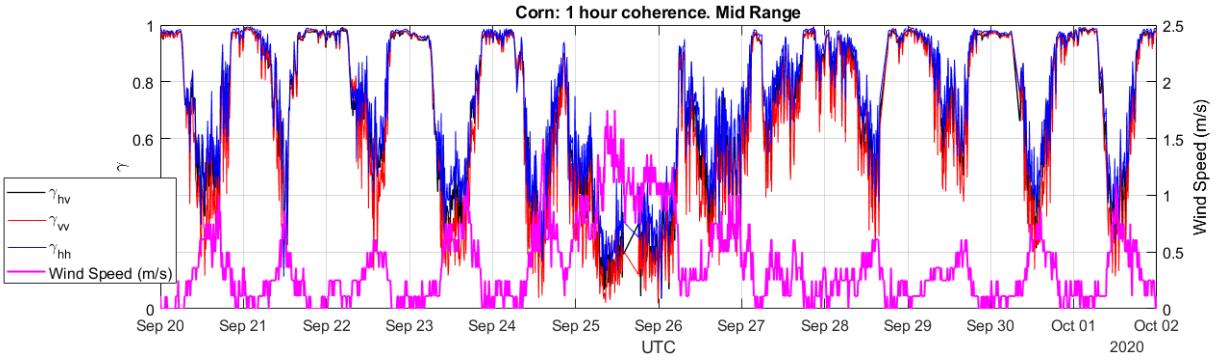

Figure 7.50 Time series of 1 hour temporal baseline coherence of corn crop between September 20 and October 2 for HH, VV, HV and VH channels for Mid Range: incidence angles (59.1°to 63°) including wind speed (magenta).

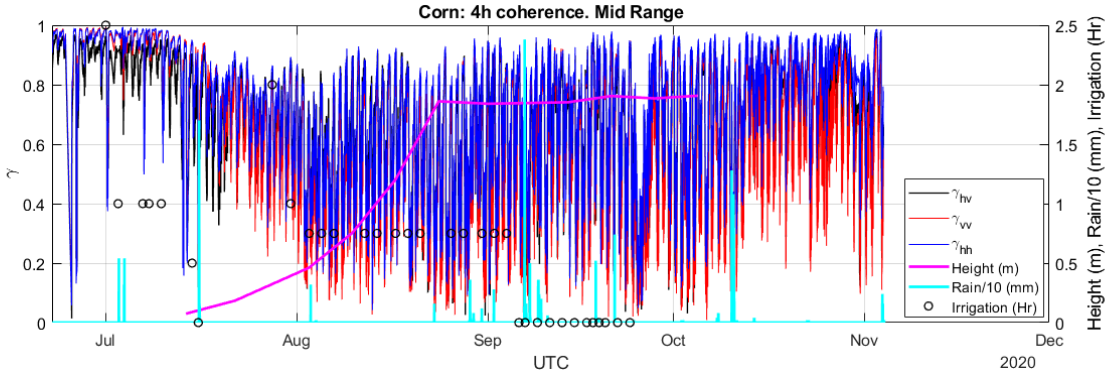

Figure 7.51 Time series of 4 hours temporal baseline coherence of the whole corn crop campaign for HH, VV, HV and VH channels for Mid Range: incidence angles (59.1°to 63°) including rain intensity (cyan) and crop height evolution (magenta) and irrigation times (black circles).

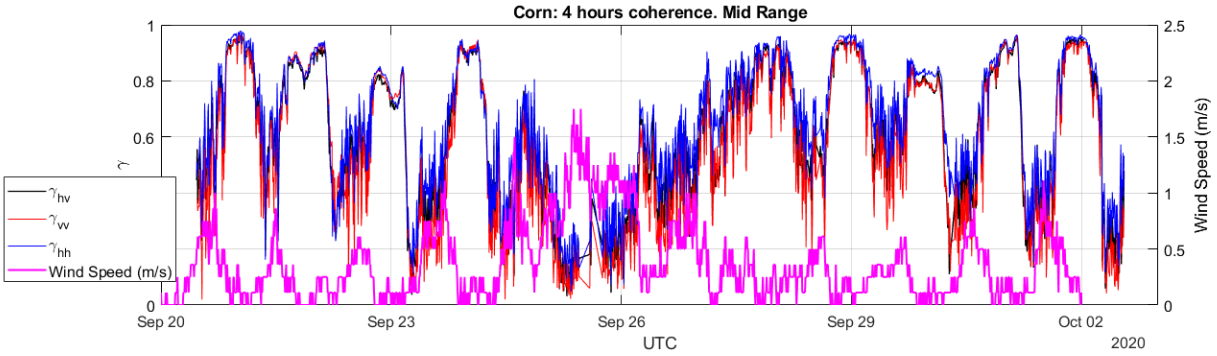

Figure 7.52 Time series of 4 hours temporal baseline coherence of corn crop between September 20 and October 2 for HH, VV, HV and VH channels for Mid Range: incidence angles (59.1° to 63°) including wind speed (magenta).

The coherence between images with a temporal baseline of 1 day of the whole corn crop campaign for HH, VV, HV and VV channels including rain intensity, irrigation, crop height evolution and LAI can be observed in Figure 7.53 and Figure 7.54. Owing to the rapid growth that corn plants experienced between July 14 and August 24, a significant loss of coherence can be seen in that time period with images obtained one day apart. Once the growth period of the plant has finished and the deterioration of the leaves has begun, a progressive increase in coherence is appreciated because the soil begins to contribute to the scattering (double bounce component). When the corn dries at the end of the measurement campaign a high level of coherence is reached. When the temporal baseline is increased to 3 or 6 days (Figure 7.55 and Figure 7.56 respectively) the start of the coherence increase is delayed. For a 6-day temporal baseline, coherence is high again only at the end of the campaign (Figure 7.56).

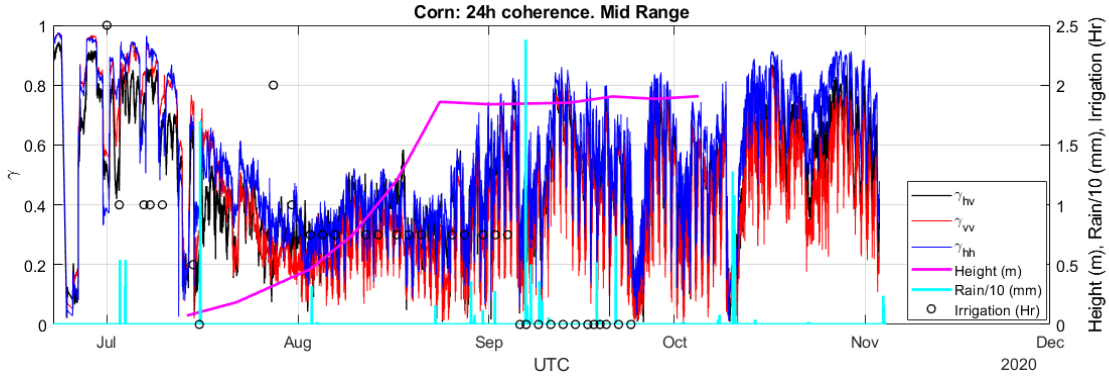

Figure 7.53 Time series of 24 hours temporal baseline coherence of the whole corn crop campaign for HH, VV, HV and VH channels for Mid Range: incidence angles (59.1° to 63°) including rain intensity (cyan) and crop height evolution (magenta) and irrigation times (black circles).

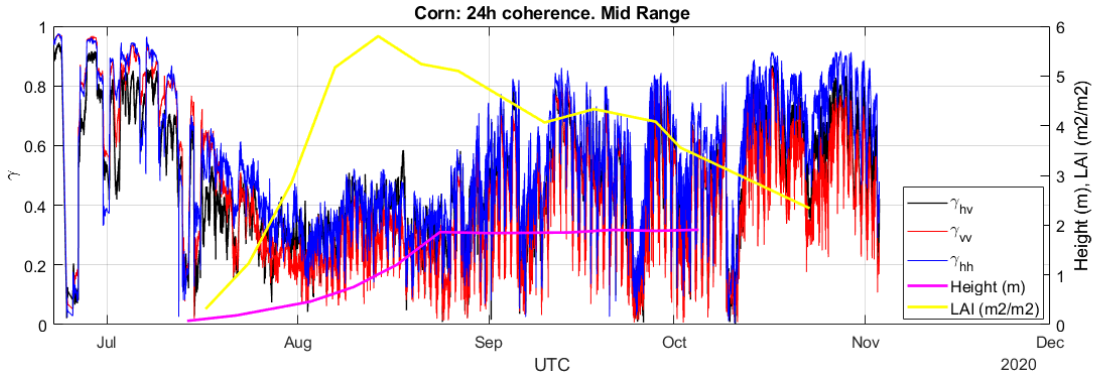

Figure 7.54 Time series of 24 hours temporal baseline coherence of the whole corn crop campaign for HH, VV, HV and VH channels for Mid Range: incidence angles (59.1°to 63°) including LAI (yellow) and crop height (magenta) evolution.

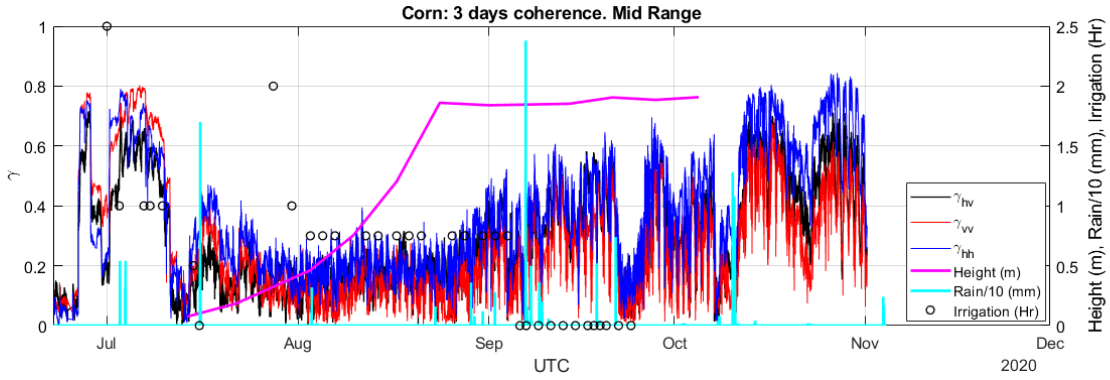

Figure 7.55 Time series of 3 days temporal baseline coherence of the whole corn crop campaign for HH, VV, HV and VH channels for Mid Range: incidence angles (59.1°to 63°) including rain intensity (cyan) and crop height evolution (magenta) and irrigation times (black circles).

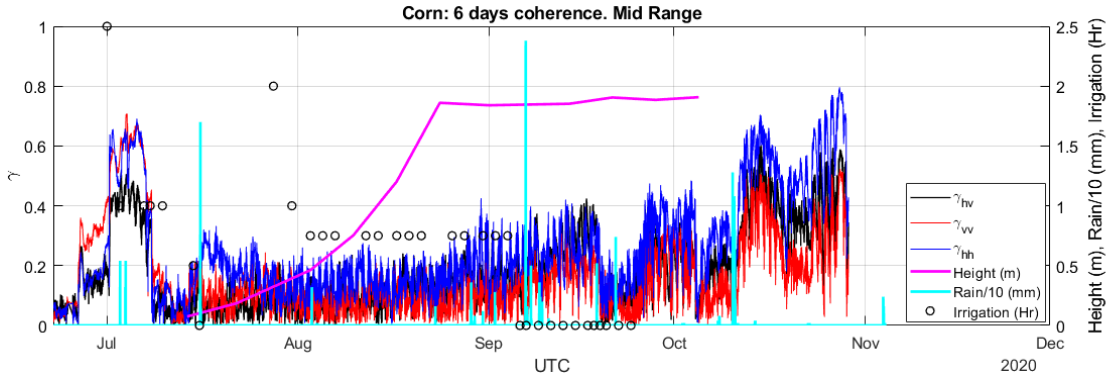

Figure 7.56 Time series of 6 days temporal baseline coherence of the whole corn crop campaign for HH, VV, HV and VH channels for Mid Range: incidence angles (59.1°to 63°) including rain intensity (cyan) and crop height evolution (magenta) and irrigation times (black circles).

7.4.6.3 Coherence loss caused by wind and rain

The coherence is affected by the changes of the atmosphere, especially wind and/or rain. The impact of wind on radar coherence has been evidenced in Sections 7.4.6.1 and 7.4.6.2. Complementarily, for the wind analysis, an event on 6 December has been chosen, where the wind speed was significantly above the average measurements.

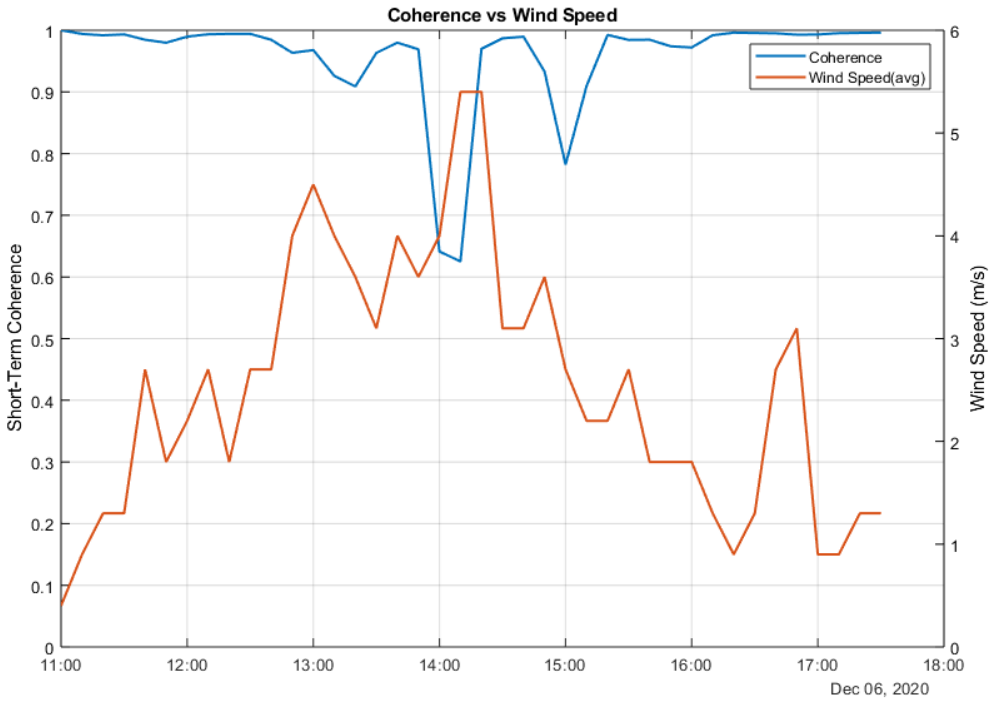

Figure 7.57 Wind speed impact on coherence in absence of vegetation

Figure 7.57 shows the short-term coherence evolution in a windy day, obtained by processing consecutive images with 10' acquisition interval. The average wind speed is also shown and a strong correlation opposite sign can be shown. Note that the coherence in this particular case is very high since the observed field was bare soil with vegetation rests resulting from harvesting the corn as shown in Figure 7.58.

Figure 7.58 Photograph of the HydroSoil field on 22 December after corn harvest.

The rain effect on the coherence has been evaluated in another event between 10 and 11 October (about 36 hours), resulting in a large volume of cumulated rain precipitation in this interval. In this case, the short-term coherence obtained from VV polarised images is inversely proportional to the amount of rain precipitated on the field (*Figure 7.59*). It is interesting to note the remarkable sensitivity of coherence with respect to rain, beginning to drop well in advance the first rain is measured by the pluviometer. The last remaining acquisitions once the rain stopped show that when the field starts to dry out, the short-term coherence recovers very quickly. Note that the coherence in the last wind and rain results has been computed with a 150x150 sliding window covering most of the field area (near, mid and far range).

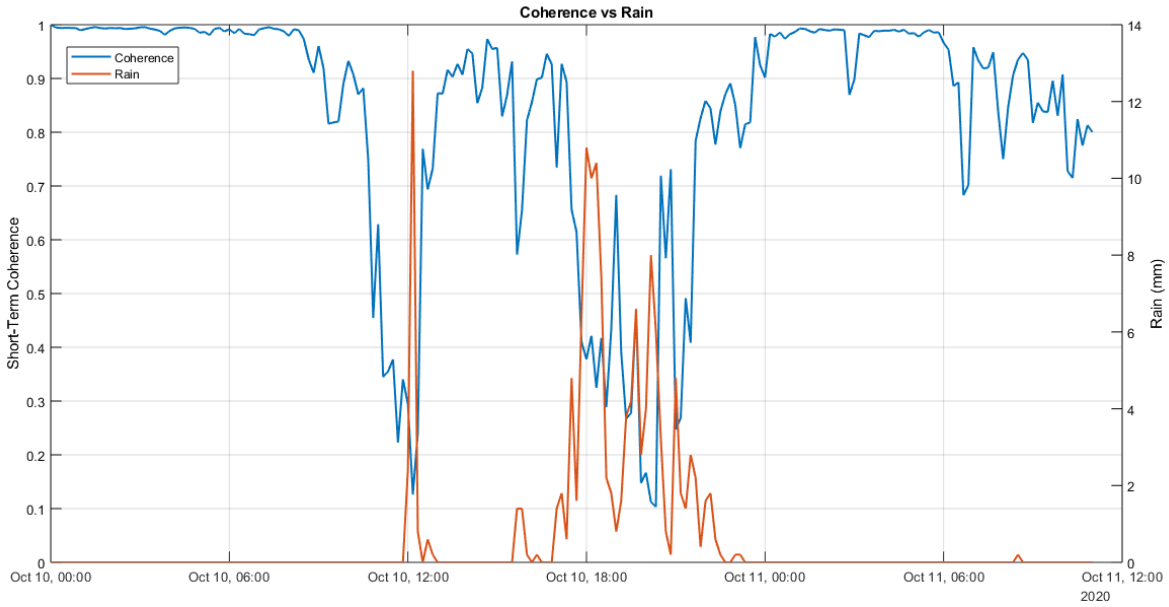

Figure 7.59 Short-term coherence versus rain intensity in 10-11 October (corn crop).

7.4.6.4 Corn crop phase changes

Once the module of the coherence has been studied, an attempt to see the impact of crop growth on the field phase evolution was performed. In of Figure 7.60, Figure 7.61 and Figure 7.62, some obtained results of the phase of the calibrated images are shown and commented. A spatial average value of the field phase change has been obtained as the argument of the complex coherence parameter as described in 6.4.6.3. Only the mid range zone of corn crop has been studied, which has the best compromise between number of looks and incidence angle.

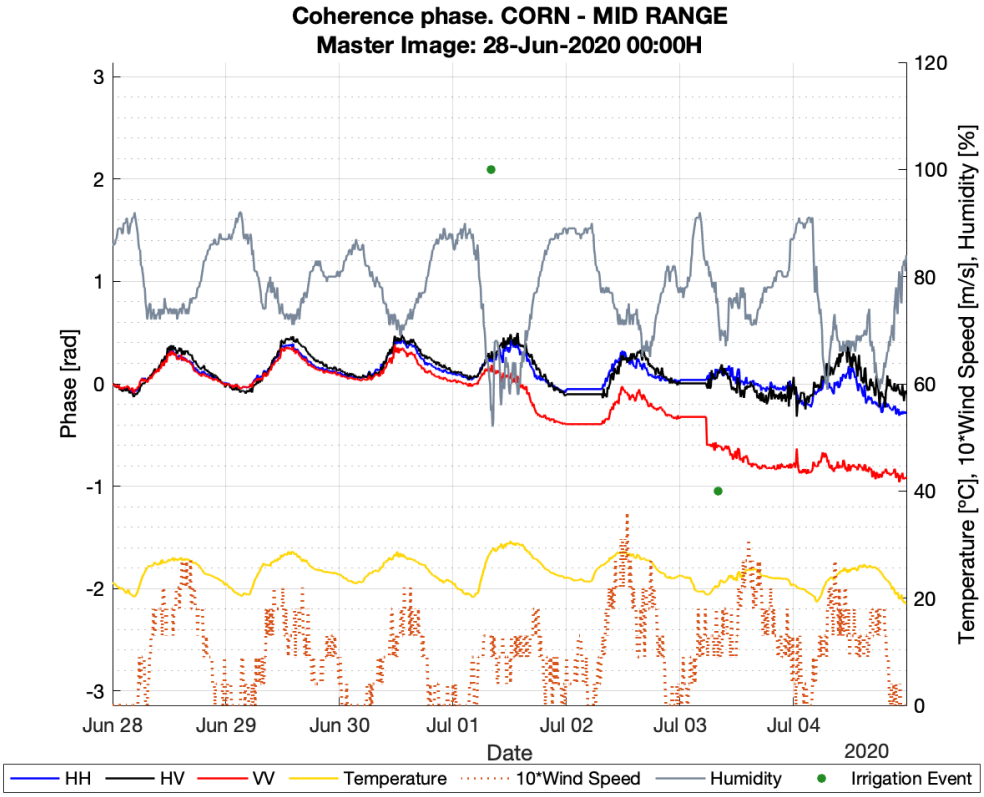

Figure 7.60 Phase of the Coherence. Bare Soil. The first image of the interval is the Master.

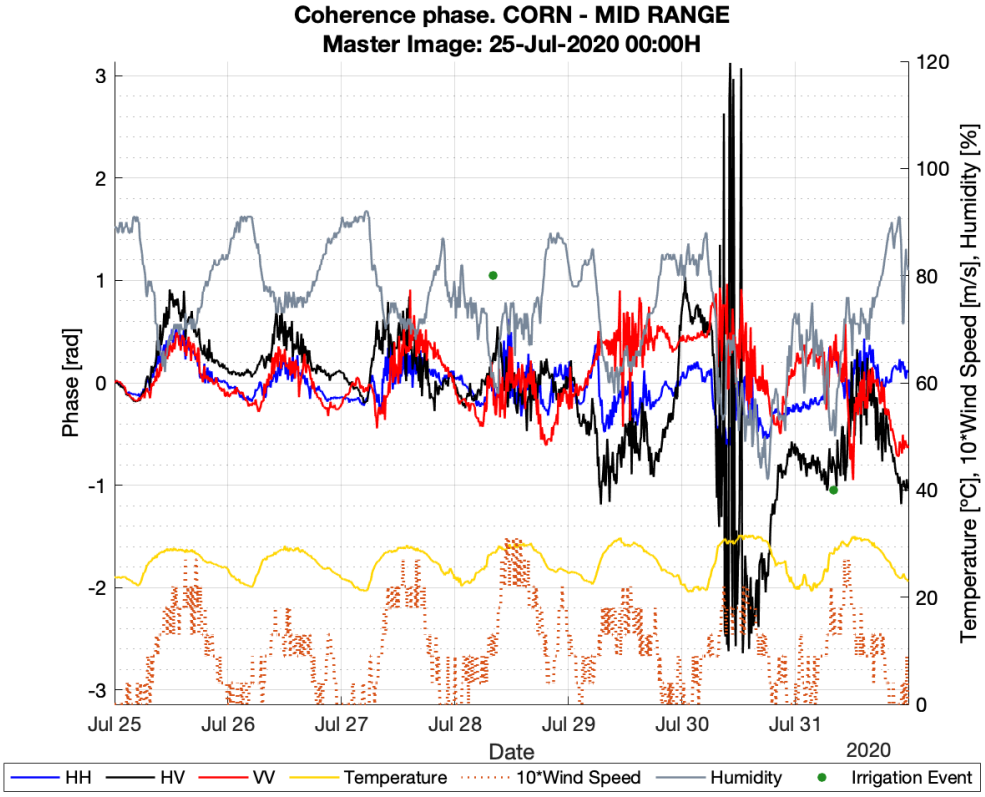

Figure 7.61 Phase of the Coherence. Plant height ~40 cm. The first image of the interval is the Master.

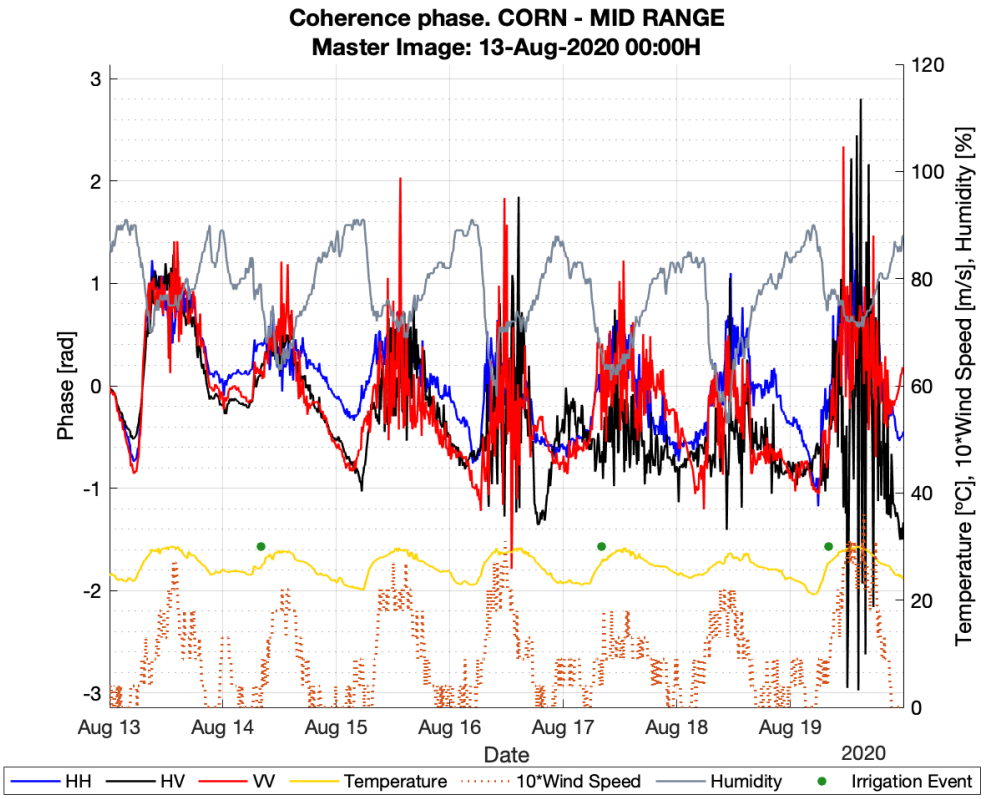

Figure 7.62 Phase of the Coherence. Plant height ~1 m. The first image of the interval is the Master.

In spite of the fast growth of corn in the intervals shown in Figure 7.61 and Figure 7.62, the phase evolution does not reflect the average range reduction between the canopy and radar caused by growth. The fact that plants development is located at the top which decorrelates the phase of a growing canopy, combined with the small radial projection of vertical motion given the large incidence angle of the radar observations could explain this result.

As expected, phase stability is depending on the image coherence which decays with the plants development from Figure 7.60 (Bare soil) to Figure 7.62 (1 m height). Except in the case of bare soil, the wind, usually maximum around noon UTC, has a strong impact on the phase stability as shown in Figure 7.61 and Figure 7.62 where the wind influence is higher.

As it was found in the case of barley (6.4.6.3), the images phase evolution is inversely related to the field air humidity changes. This change is associated to changes in the phase of the surface/volume backscattering coefficient of the scene since the impact of the atmospheric refraction changes is comparatively small.

This result indicates that the atmospheric humidity, possibly in combination with temperature evolution and wind, induces physical changes on soil and vegetation canopy responsible for the observed phase evolution.

7.4.6.5 Atmospheric phase changes

The phase changes introduced by the radar waves propagation through the atmosphere can be significant and need to be compensated in order to avoid errors in the analysis of radar measurements. These changes can be introduced by the changes in the humidity, temperature and atmospheric pressure. For this project, the ITU-R P.453-11 standard [5] has been used to compute

the refractive index of the atmosphere in the different acquisitions. The refractive index ***n*** enables to predict the impact of atmospheric phase changes on the image of the field with equation (7.1)

$$\emptyset(t) = -4\pi f_0 \frac{n(t)}{c} R \tag{7.1}$$

To see the difference between the predicted phase changes and the experimental ones, an event on the 2-3 August has been selected. For a better analysis, only the co-polar (VV) calibrators located at 36 and 80 meters are used to show the compensation of the atmosphere in the experimental results obtained by the GB-SAR (Figure 7.63, Figure 7.64). The plots show the phase differences calculated as obtained phase along time relative to the initial phase. Note that there is a specific moment around 5:30 H where a significant difference occurs between measured and theoretical (modelled) plots. The discrepancy is explained by the fact that 2 mm of rain started to drop for 20 minutes at 5:20 H causing a substantial change in the experimental phase.

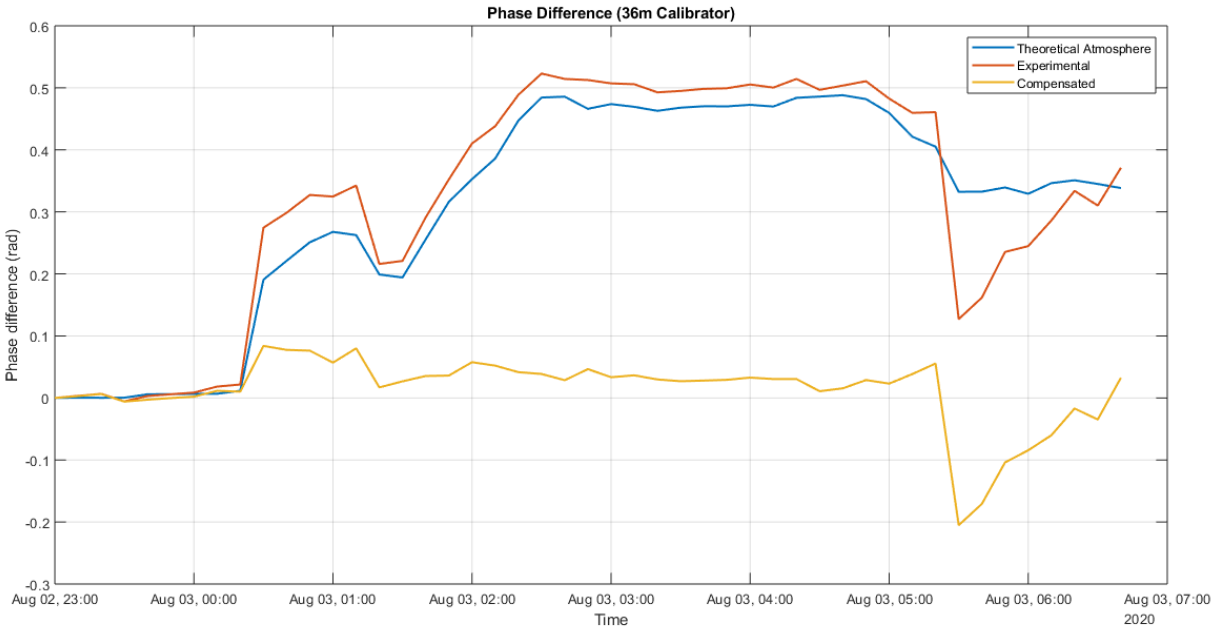

Figure 7.63 Measured, predicted and compensated 36 m radar reflector phase change.

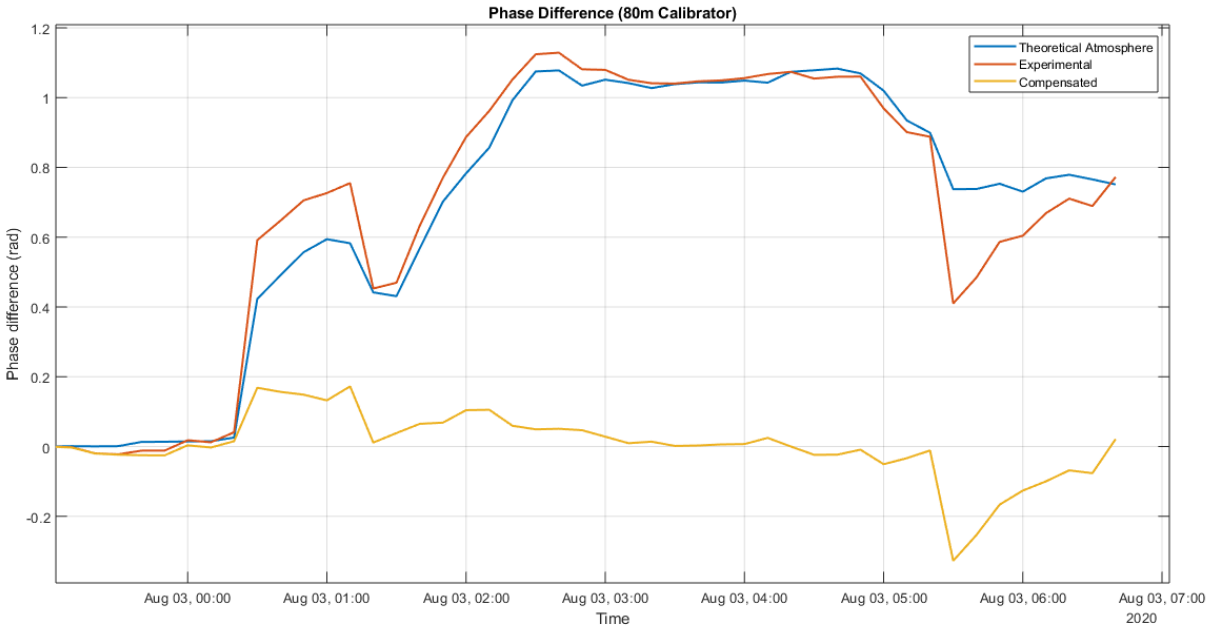

Figure 7.64 Measured, predicted and compensated 80 m radar reflector phase change.

The compensation in the whole SAR image can be better appreciated in the same event, by observing an interferogram before (Figure 7.65) and after phase compensation (Figure 7.66). Without compensation, a linear phase ramp appears along the image range dimension that can be well appreciated in stable areas (bare soil) of the scene drifting from neutral green to a positive phase yellow to light orange at 100 m range. After compensation, the stable areas show a flat zero-drift phase (except for the speckle noise), which is needed to observe small phase changes on the SAR image. These results show how relevant atmospheric phase changes can be, even at very short distances of observation, and the possibility of its compensation when the basic atmospheric parameters (pressure, humidity and temperature) are known. The presented results also show that the interferometric phase images of the observed surface, if the background is stable in the short term, are capable of mapping atmospheric changes which may be used in high resolution numerical meteorological models and prediction.

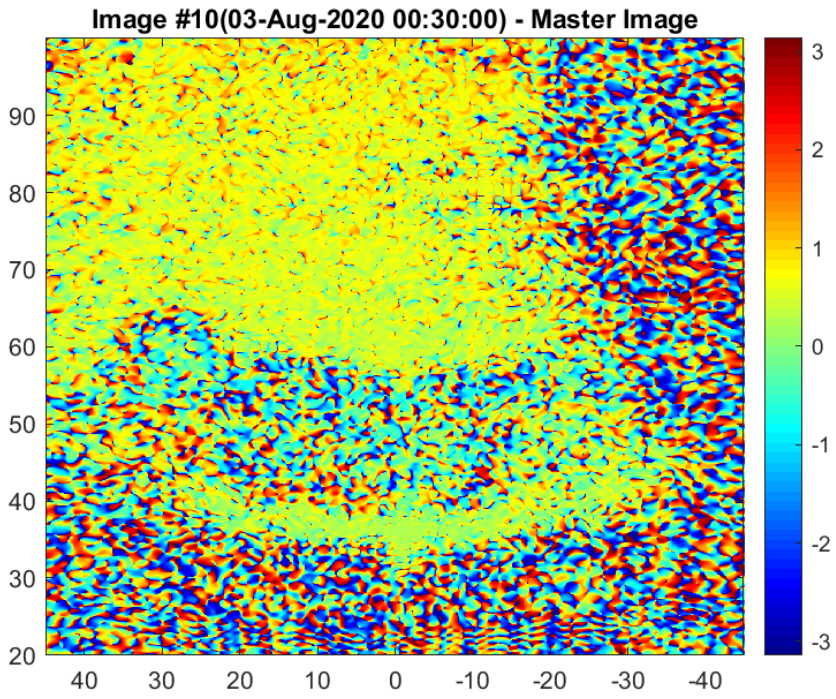

Figure 7.65 Interferogram using VV polarisation between 00:20 and 00:30 (UTC) SLC images showing a linear phase atmospheric artefact along range. Polar Coordinates.

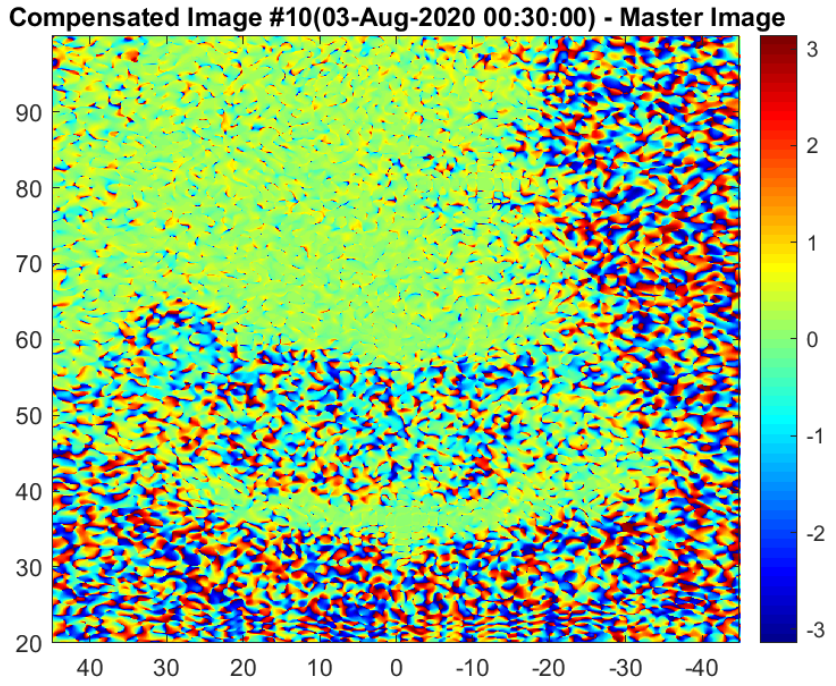

Figure 7.66 Interferogram between 00:20H and 00:30 (UTC) SLC images with atmospheric compensation where the linear phase artefact along range has been removed. Polar Coordinates.

7.4.7 Slow Aperture assessment

Slow Synthetic Apertures, as the ones generated by GeoSAR Systems, can be assessed by means of the combination of short raw-data segments of consecutive fast apertures (Figure 7.67).

Full-Pol SLC result of combining 2-1/2 h radar samples taken from 13:44 to 16:12 on 21 September 2020 is shown in Figure 7.68, and can be compared with fast aperture result of a fast SLC from one from the centre of the slow equivalent aperture time. The average wind speed in this interval was 0.85 m/s with peaks of 4 m/s.

The quality of these ultra-slow apertures can also be assessed by means of the Coherence between 2h or 4 hours UltraSlow SLC and the 1.5 sec Fast SLC centred in the period of the UltraSlow (Figure 7.69).

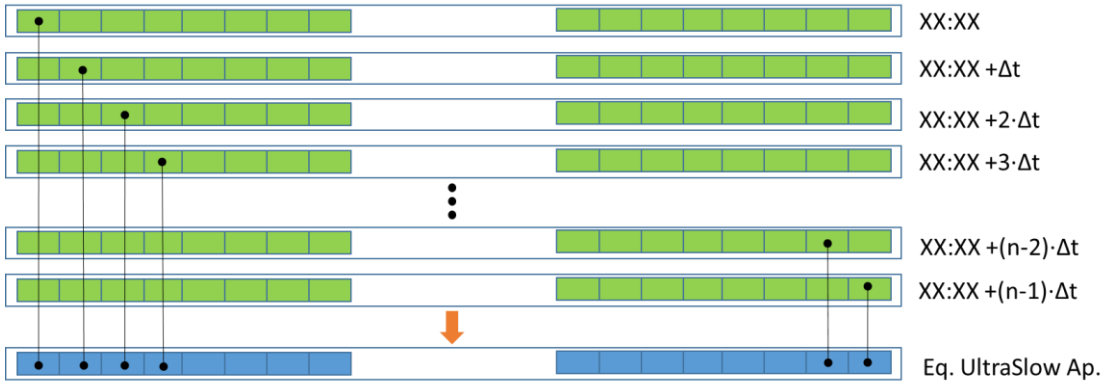

Figure 7.67 Different parts of the raw-data of consecutive fast apertures are combined in order to generate an equivalent Slow aperture, as the one generated by GeoSAR Systems.

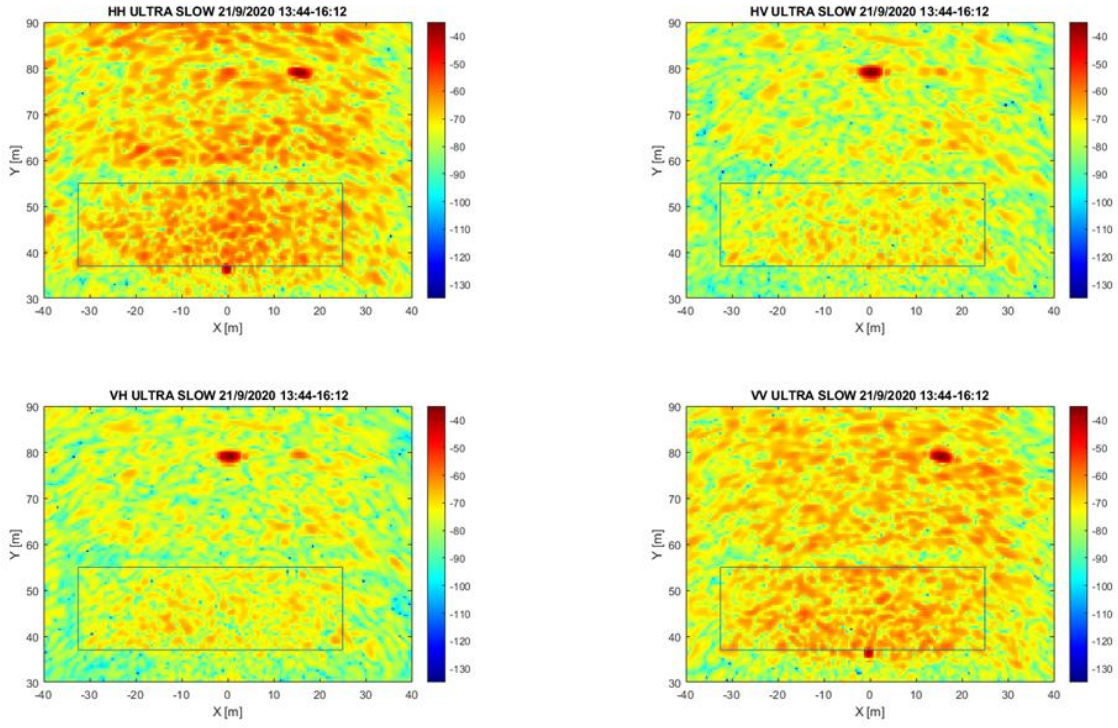

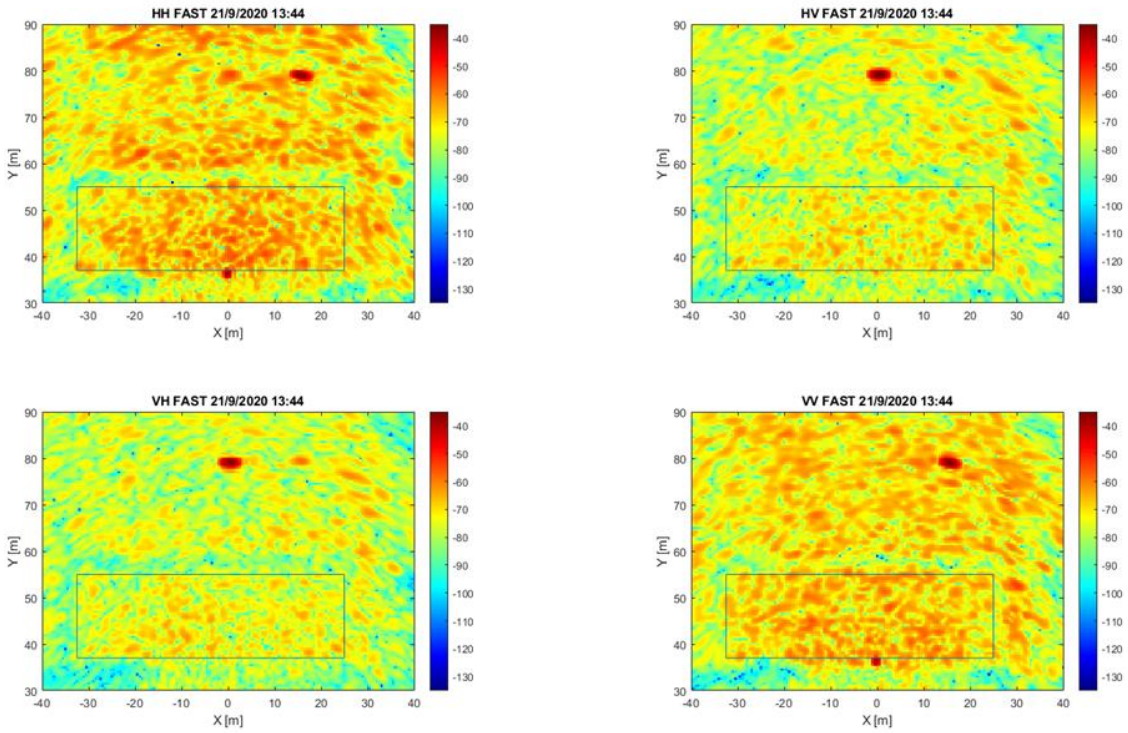

Figure 7.68 Comparison of SLC images from the System operated as ULTRA-SLOW and FAST-GBSAR modes. Cartesian coordinates.

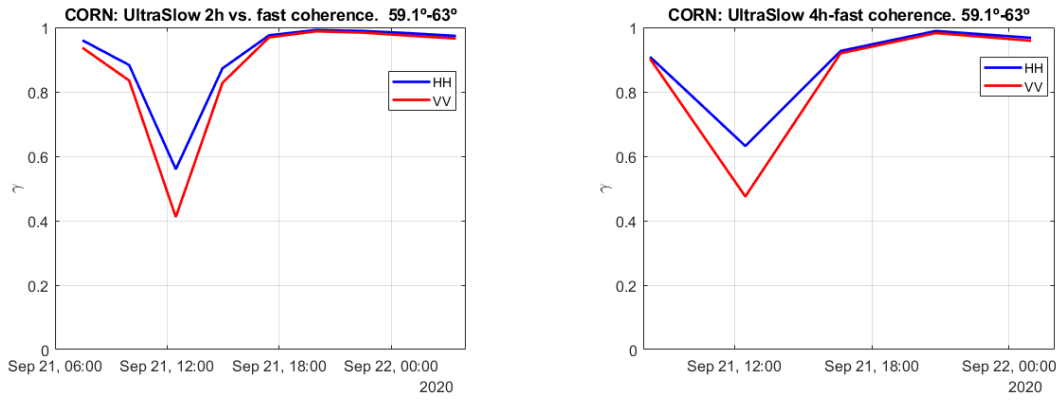

Figure 7.69 Mean Coherence evolution from the coherence map between a synthetic UltraSlow SLC (left is a 2 1/2h and right is 4h long equivalent aperture) and the Fast Mode SLC from the centre of the time period of the equivalent slow aperture.

7.4.8 Doppler spectrum of agriculture fields

Obtaining the intrinsic Doppler Spectrum of agriculture fields is interesting in order to model the scene motion impacts on SAR processing. This is particularly important in the case of long Synthetic Aperture integration time missions such as Geosynchronous SAR (GEOSAR) Hydroterra [1]. The Doppler spectrum has been measured as follows: The radar has been operated from a fixed position on the rail. Radar obtains a fast burst of backscattering measurements along a period of 6 seconds. The radar signals are range compressed and the time history evolution of the different range cells is converted to Spectral Power Density using a Fast Fourier Transform. The radar measurements were taken with HH polarisation when the corn crop was stable in height but for different wind conditions in September 2020. The Doppler spectrum of the range cells from Near Range to Far Range of the field is averaged.

Figure 7.70 shows the Doppler Spectrum obtained from different mean wind speeds. Notice that without synthetic aperture processing, the antenna beamwidth of the radar is not sufficiently narrow to fully reject the Doppler shifts corresponding to field adjacent areas such as the surrounding reeds zone at the right side of the field. These results must be interpreted with care since the instantaneous wind speed blowing in the 6 s measurement window is unknown and may differ from the average value registered by the anemometer with an integration time of 10 min.

An interference line in the Doppler spectrum around +/- 20 Hz was detected which was not present in the barley campaign and could not be detected in laboratory radar characterisation and post-campaigns maintenance. It might have been caused by an unknown external interference, which did not affect the SLC images generation since it is well below the radar scene average backscattering level.

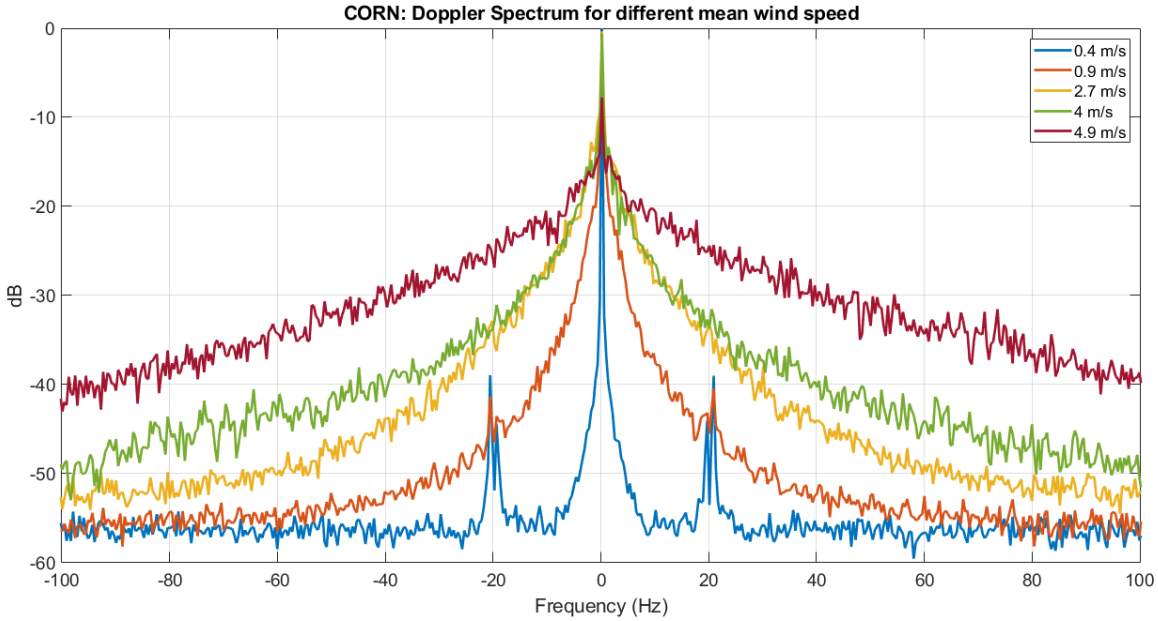

Figure 7.70 Different mean Doppler Spectra have been obtained for several mean wind speeds using HH polarisation. The measurements were carried out on September 2020 on fully-grown corn crop.

8 HYDROSOIL RADAR CALIBRATION ASSESSMENT

During the barley campaign, starting on March 2020, due to the restrictions imposed by the COVID-19 outbreak only a trihedral could be deployed for calibration purposes (Figure 8.1). On the corn campaign, which started at the end of June 2020, a trihedral, a vertical dihedral and a 45° tilted dihedral were deployed (Figure 8.2).

Figure 8.1 The triangular trihedral of 50 cm edge used for calibration in the barley campaign

Figure 8.2 A triangular trihedral with a 50 cm edge, a vertical dihedral and a 45° tilted dihedral, made of two 40x40 cm^2 metal plates, were deployed in the field in the corn campaign. The trihedral was relocated to a centred position in front of the field

The quality of the calibration strongly depends on the quality of the used calibrators. Cross-calibration tests based on the trihedral and dihedral reflectors have shown that their radar reflectivity is affected by the ground clutter sharing the reflector resolution cell.

Two of the reflectors can be used for calibrating the co-polar channels, this is the trihedral and the 90° tilt dihedral as, ideally, they should not present any cross-polar component.

The plots of the original data before any calibration show that the fast variations (daily cycle) have different levels depending on the polarization and the reflector, Figure 8.3 and Figure 8.4. For the corner, they are quite similar and around ±0.25 – ±0.3 dB. For the 90° dihedral the daily cycle ripple in VV is larger than in HH, around ±0.3 dB for the former and ±0.15 dB for the later. In addition to the ripple, in both reflectors a long-term magnitude drift with a linear behaviour can be identified.

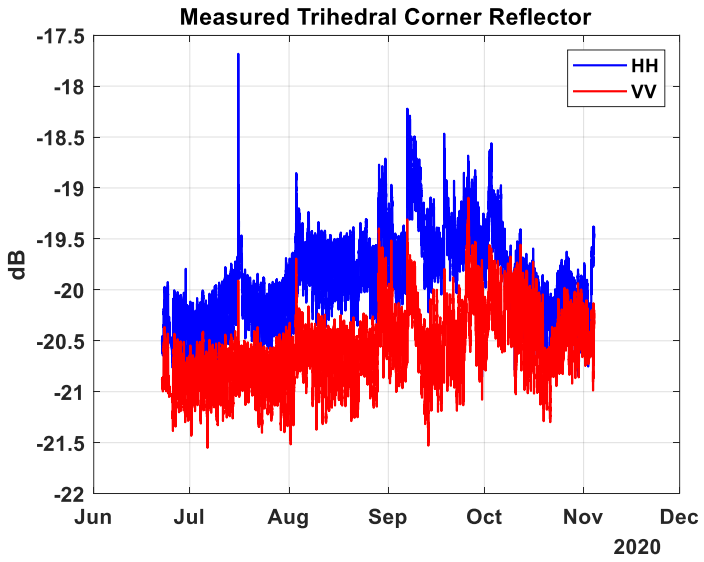

Figure 8.3 Measured uncalibrated co-polar channels for the trihedral deployed during the corn campaign.

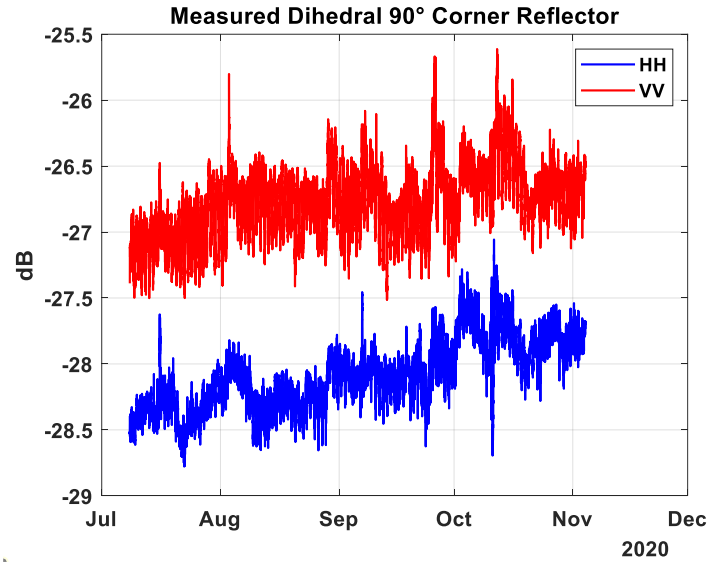

Figure 8.4 Measured uncalibrated co-polar channels for the 90° (vertical) dihedral deployed during the corn campaign.

On the contrary, the 45° dihedral produces strong cross-polar components and, ideally, null co-polar ones. Looking and the uncalibrated data shown in Figure 8.5, in addition to offset differences as it was stationed in two different places during the campaign, we can observe a similar behaviour.

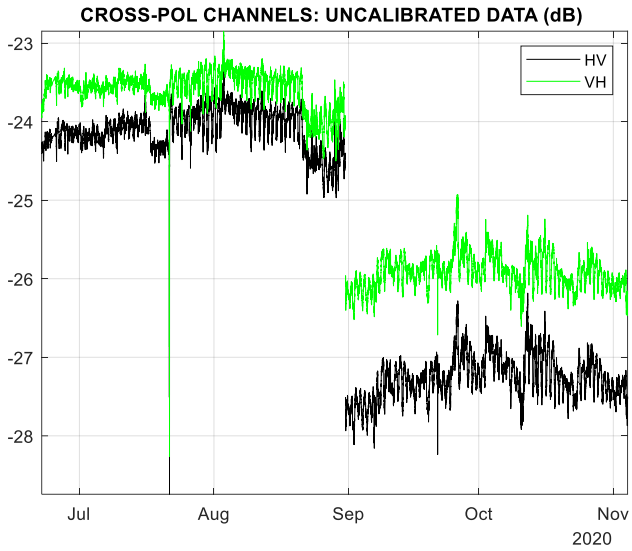

Figure 8.5 Measured uncalibrated cross-polar channels for the 45° dihedral deployed during the corn campaign.

After a first inspection of the calibration data set, the cause of the daily variations on the measured data was not evident. There are only two options: the ground clutter affecting the reflectors or the instrument circuitry.

Due to the lack of a common mode in the reflectors backscattering measurements, it was concluded that the response of the reflectors is affected by the surrounding clutter. For the co-polar channels this clutter can be different for each polarization, as the clutter contribution in HH does not have to be correlated with the one in VV. This behaviour can be seen in Figure 8.3 and Figure 8.4 where HH and VV uncalibrated plots show different time evolutions. On the contrary, in the HydroSoil quasi-monostatic observation the HV and VH backscattering are equal and therefore the clutter affecting the response of the 45° dihedral is expected to be identical for both channels, which is confirmed by the similar HV and VH uncalibrated backscattering evolution shown in Figure 8.5.

The effect of the surrounding clutter on the reflector response, both magnitude and phase, can be estimated according to the signal to clutter ratio. If the clutter is modelled as an interference with a certain modulus and changing phase, depending on the surface and atmospheric conditions, as shown in Figure 8.6, the response of the reflector shows an amplitude and phase variation according to the Table 8.1.

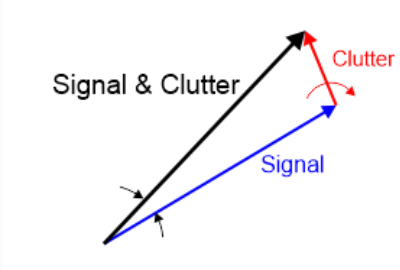

Figure 8.6 Graphical representation of the effect of the clutter on the detected signal.

Signal to clutter ratio (dB)	Modulus variation (dB)	Phase variation (°)
40	±0.086	±0.57
36	±0.138	±0.9
32	±0.22	±1.43
28	±0.34	±2.27
24	±0.55	±3.61
20	±0.9	±5.71

Table 8.1 Signal to Clutter ratio and its effect on Modulus and phase of the Calibrator response

If we have a look at the ratios in dB of the theoretically identical co-polar and cross-polar channels for the reflectors shown in Figure 8.7, we can see very different behaviours.

The 90° dihedral seems to have the larger daily ripple behaviour, followed by the trihedral. The 45° dihedral is the one that performs better. Making a zoom on the latter, we can visualize in Figure 8.8 that the short-term uncertainty is around ±0.1 dB.

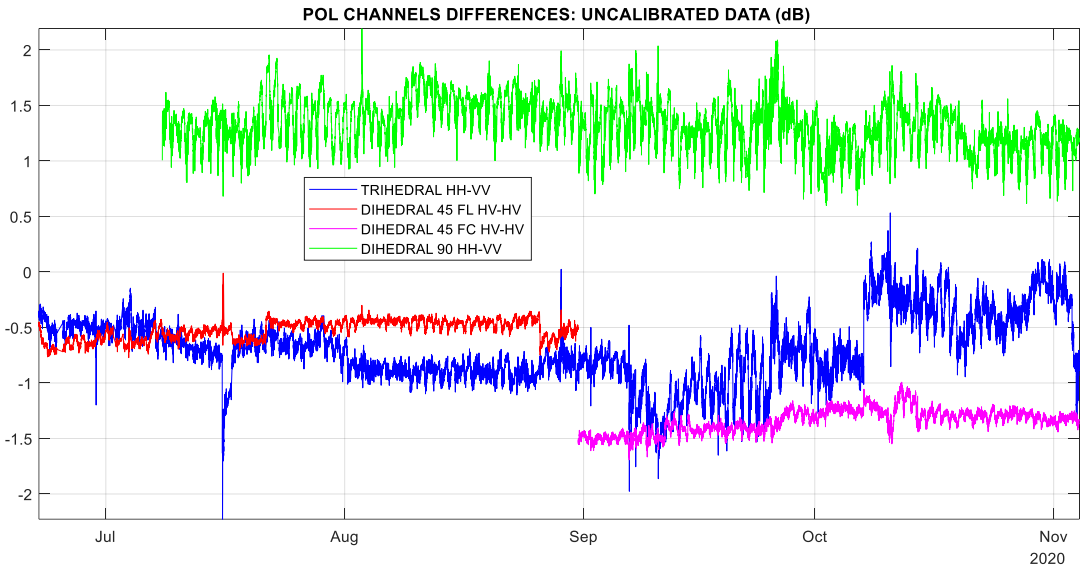

Figure 8.7 Differences of the measured uncalibrated co-polar and cross-polar channels for the trihedral, the 90° dihedral and the 45° dihedral deployed during the corn campaign. The latter was reallocated at the end of August that justifies the reflectivity difference.

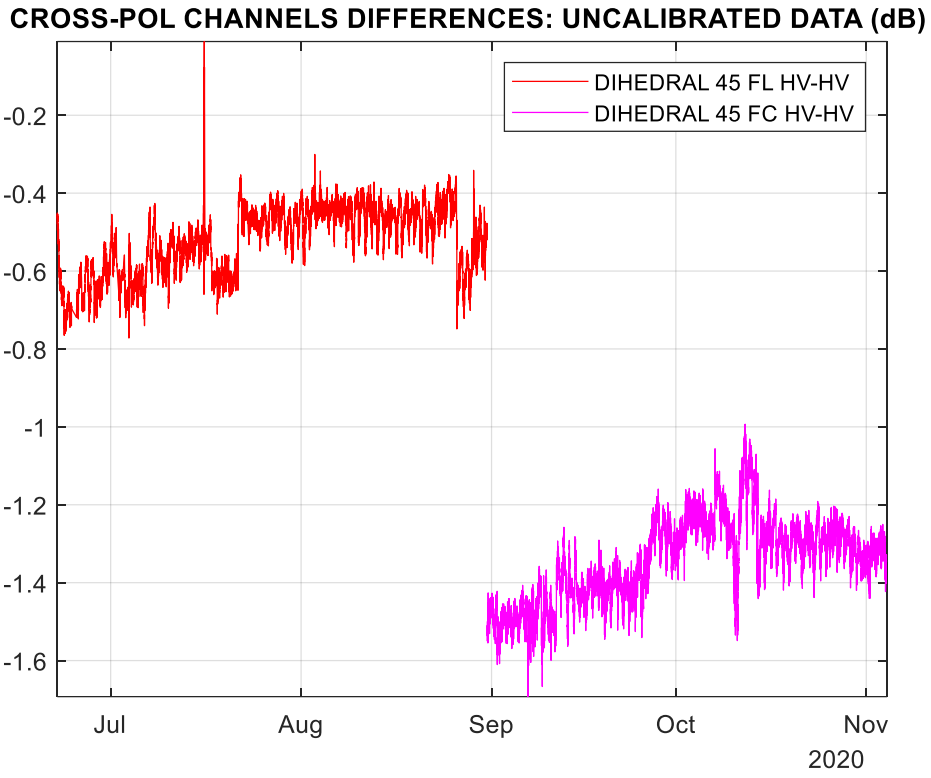

Figure 8.8 Differences of the measured uncalibrated cross-polar channels for the 45° dihedral deployed during the corn campaign.

The cross-pol channels are the case in which the two channels share the minimum circuitry of the instrument, as it can be seen in the error model presented before. As the clutter should be identical for both channels the differences can be associated to the instrument. The only way to justify such a good behaviour is the stability of the hardware. The behaviour of the different non-common elements associated to each channel, either in transmission or reception, should be similar. For instance, all amplifiers would reduce their gain with the temperature and what can be different is the rate. Summarizing, it is not possible that a noisy behaviour in the H channel transmission elements was compensated by a complementary noisy behaviour in the V receiver elements, and vice versa. The instrument presents a very good stability with just a long-term drift.

Similarly, the phase of the different polarimetric channels also presents a good stability. The phase of the uncalibrated response of the trihedral during the barley campaign, Figure 8.9, shows a slight linear trend of the temporal evolution of the phase, which could be explained by the settlement of the mast holding the trihedral.

For the corn campaign, more reflectors were deployed. The detailed analysis of their uncalibrated phases shows again its good stability. Some of the sudden changes in the phase could be caused by activities in the field and/or undesired interaction of personnel with the reflectors or strong atmospheric artefacts. Figure 8.10 shows the temporal evolution of the trihedral, the uncalibrated phase differences of the co-polar channels show a daily phase ripple ranging from ±1.25º to ±2.5º but we have to keep in mind the clutter affected differently HH and VV. A slope in the phase generated by a slow movement of the trihedral anchor can be observed in the figure. This movement was very slow and had no effect on the daily cycle variations.

The 45° dihedral, as the clutter affects identically both cross-polar channels, presents a better stability of the phase difference, as shown in Figure 8.11. The phase ripple is almost below ±0.5º.

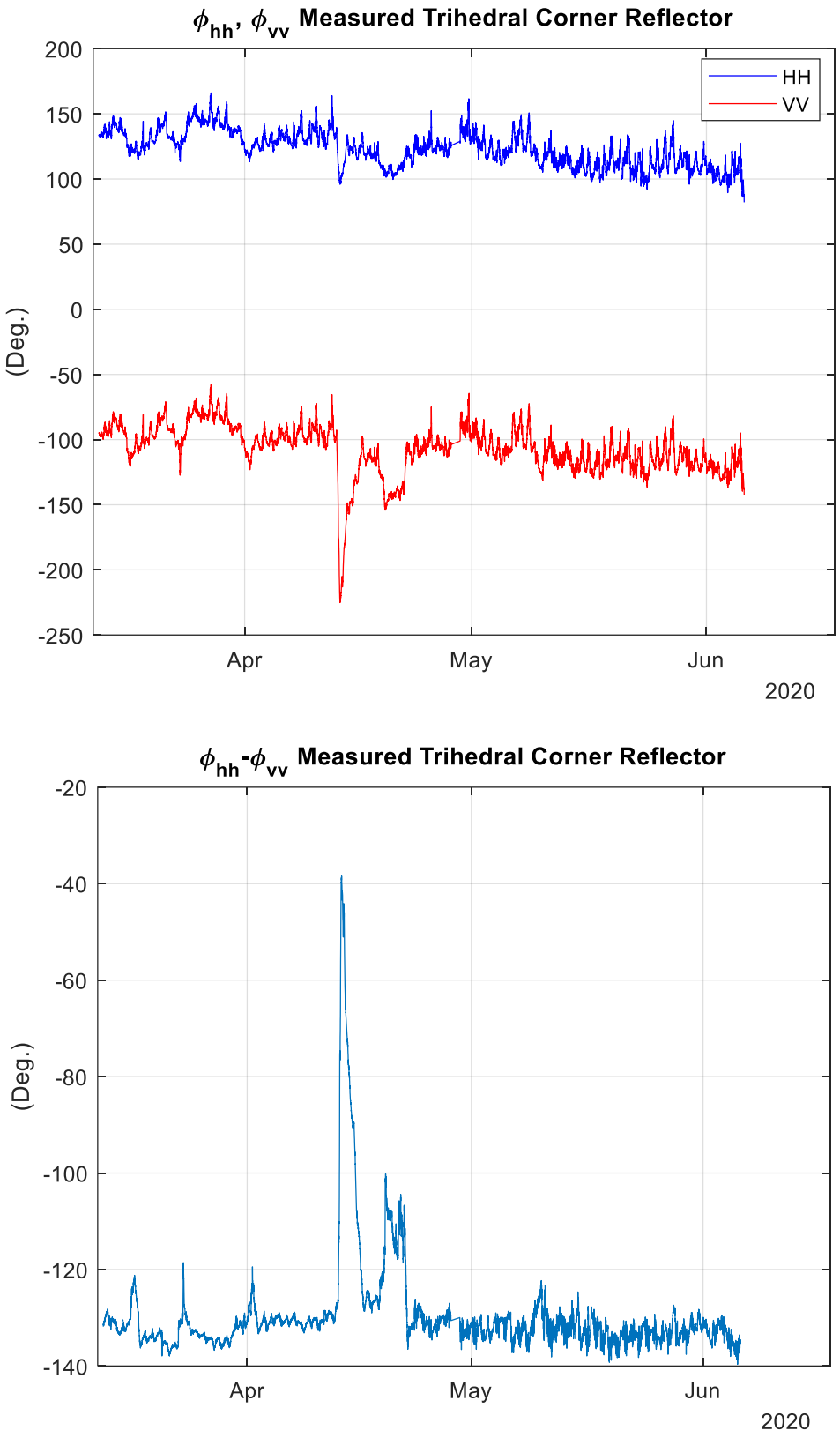

Figure 8.9 Uncalibrated temporal evolution of the phase of the HH and VV channels response of the trihedral (above) and its phase difference (below).

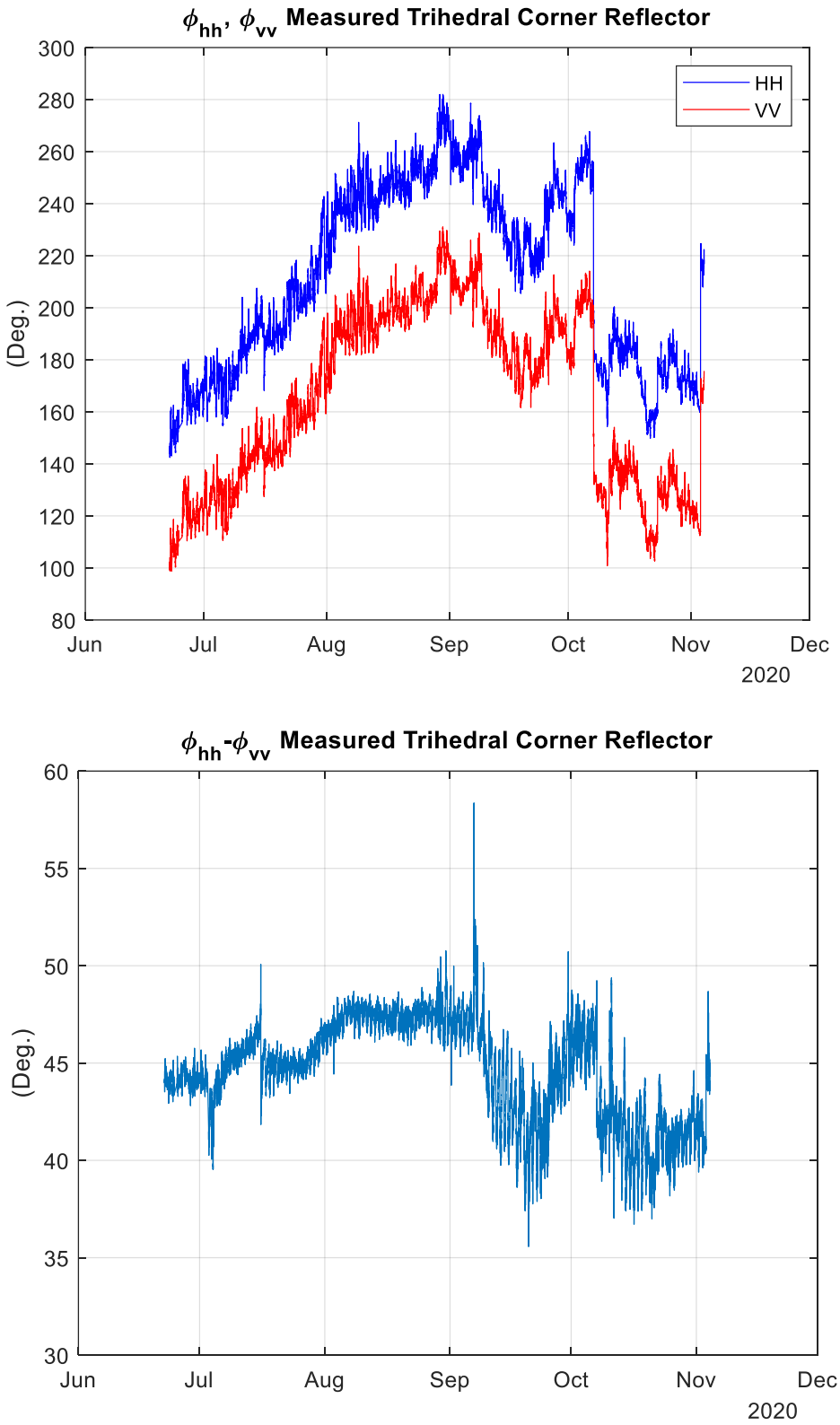

Figure 8.10 Uncalibrated temporal evolution of the phase of the HH and VV channels response of the trihedral (above) and its phase difference (below) during the corn campaign.

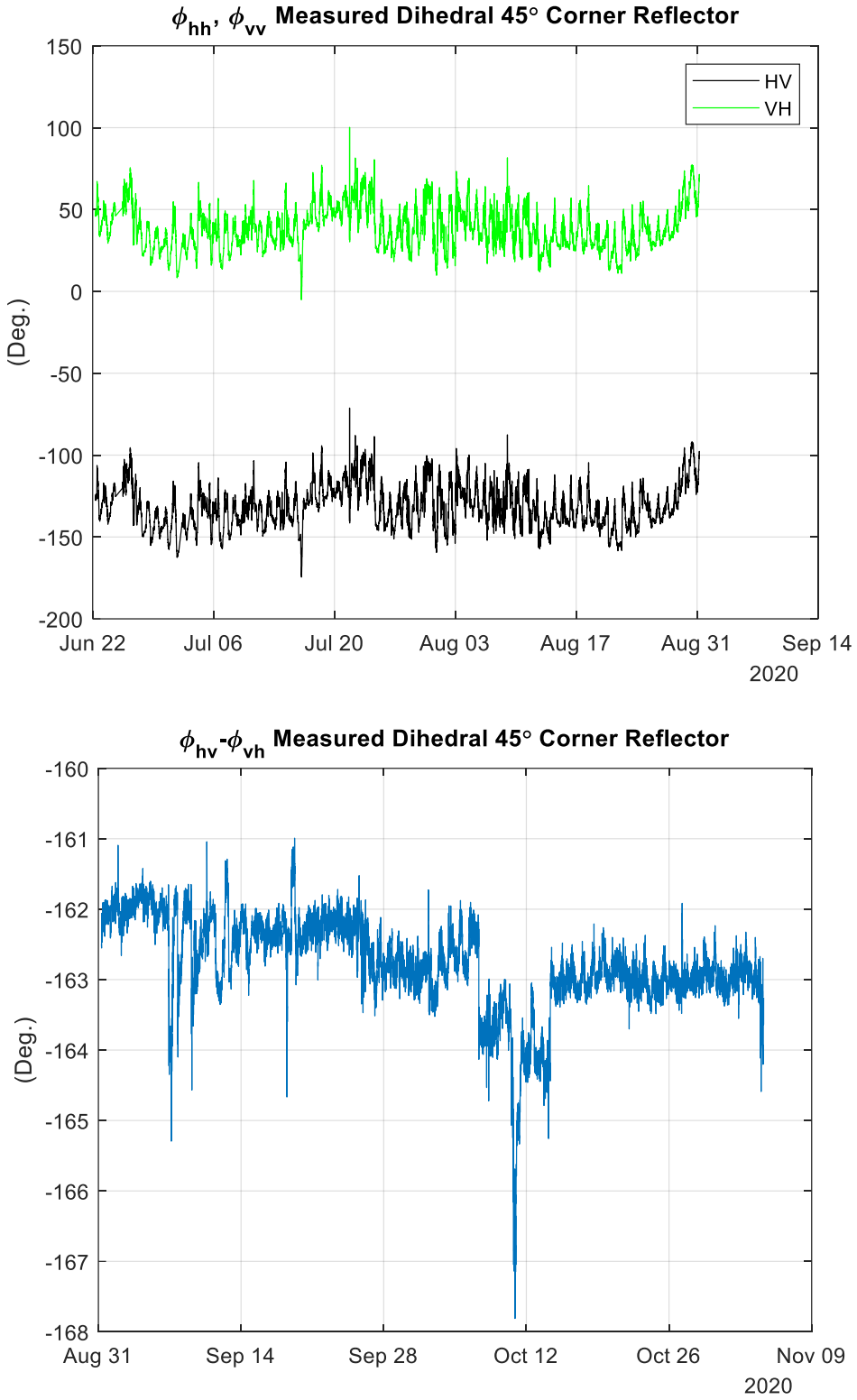

Figure 8.11 Uncalibrated temporal evolution of the phase of the HV and VH channels response of the 45° dihedral (above) and its phase difference (below) during the second part of the corn campaign.

Summarizing, the uncalibrated results demonstrate than the hardware presents a better short-term stability, as it has been mentioned in 5.4, in both amplitude and phase than the reflectors used to

calibrate the measurements. As a consequence, the calibration strategy is based on a mid/long-term instead of a short-term calibration of the radar instrument using the available reflectors allowing to reject daily cycle ripples by averaging. Thanks to intrinsic radar stability the calibration is maintained short term. The temperature drift is the main cause of gain fluctuations. Thus, radar stability is achieved by means of thermal stabilization of radar electronics at a temperature higher than the environment temperature in the worst hot conditions. This is evidenced in Figure 8.12 showing the radar gain evolution using a long coaxial cable connecting transmitter and receiver during the warm-up process after switching on the electronics. After thermal stabilisation the residual gain changes in this test are within 0.1 dB.

Considering the impact of external temperature changes, after analysing the temperature drift for a long period of time, the precision of radar backscattering measurements expressed as standard deviation, has been conservatively estimated to be below 0.4 dB in amplitude and below 3° in phase, excluding refraction atmospheric changes. The accuracy of backscattering measurements is also affected by the uncertainty of reflectors true average RCS, residual pointing errors and antenna radiation patterns compensation and is estimated to be better than 1 dB.

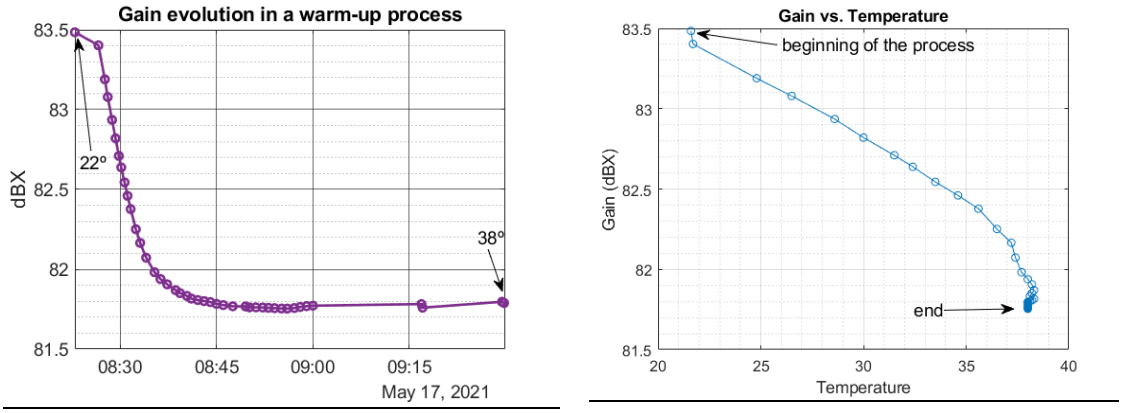

Figure 8.12. (Left) Time evolution of the Gain in a warm-up process of the radar. (Right) Gain vs. temperature

For future campaigns better attention has to be paid to the design and deployment of reflectors to be used as calibrators. Its RCS has to be large enough to reduce the impact of the surrounding clutter, to be under the defined calibration precision threshold. In addition, the foundations of the reflectors have to be designed and built with enough robustness to ensure its physical stability. Clutter can be minimized by increasing the radar spatial resolution and, if possible deploy the reflectors in low clutter areas.

9 HYDROSOIL DOCUMENTS, QUICK LOOKS AND DATASETS

The HydroSoil project information and data (documents, field measurement reports, ancillary data and SLC images) has been organized to provide an easy access to the documents and data (Figure 9.1).

GBSAR SLC data format is described in a readme.docx as well as all supplementary files.

Ancillary data are in *Excel* format, which includes headers with the definition and units of the different fields. Several readme.docx are included with instructions and comments.

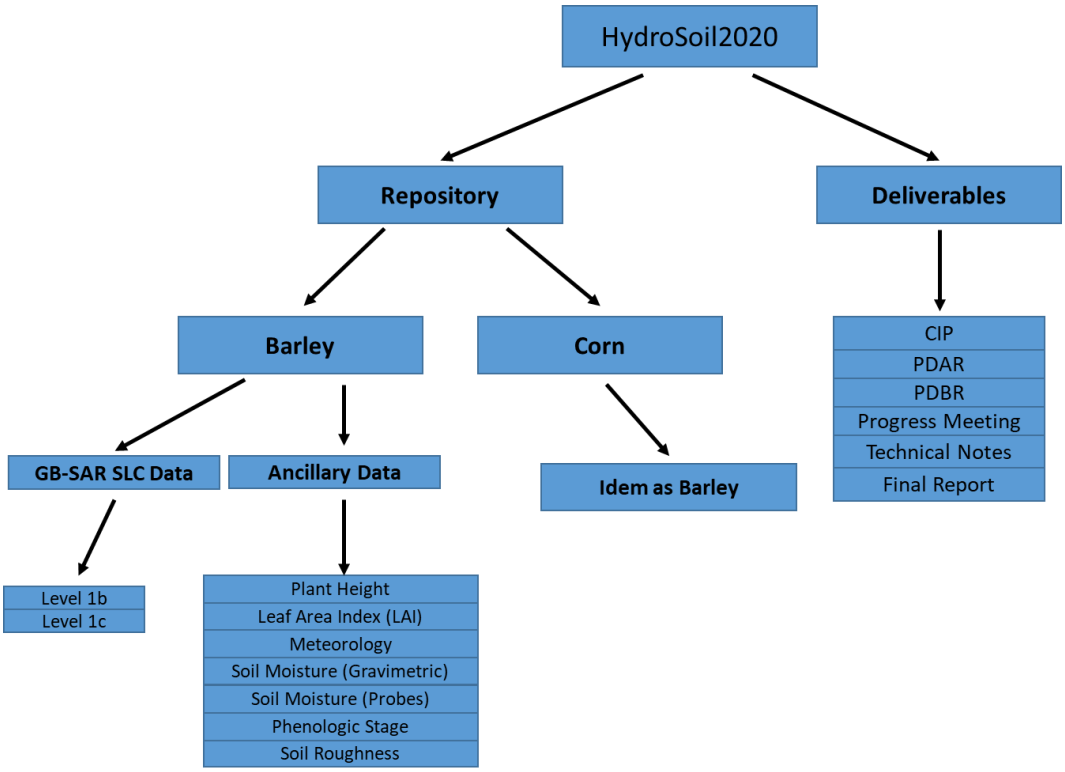

Figure 9.1 Structure of the HydroSoil2020 Cloud Drive

10 CONCLUSIONS AND FUTURE ACTIONS

After the barley and corn campaigns, multiple data inspection and processing activities have been carried out to validate HydroSoil data, to better understand the evolution of the field, the set of radar reflectors and the radar instrument itself. A preliminary assessment of the polarimetric radar backscattering of the observed crops at different time scales and its relationship with vegetation, water cycle and meteorological parameters has been carried out. The aspects of particular interest for Hydroterra Mission proposal, identified in the HydroSoil Statement of Work [SoW] have received special attention, which have been complemented with other aspects of interest in the preparation and improvement of the campaign products such as calibration and atmospheric compensation. Given the dimension of the acquired data set, with over 30,000 polarimetric images, plus a complete set of ancillary ground and meteorological data, only a preliminary processing has been possible so far, which will be continued in form of academic works and scientific publications.

The proposed short-term radar calibration, assuming stable radar reflectors, has been carefully revised, showing a better short-term radar stability compared to reflectors Radar Cross Section, which is affected by surrounding surface backscattering changes. For this reason, the calibration procedure is based both on the deployed trihedral and dihedral reflectors observations to compensate the medium to long term radar system drifts, in combination with the intrinsic excellent radar system stability that has been achieved with a constant internal temperature operation.

The backscattering evolution of barley and corn have shown distinctive characteristics, associated to very different crop volume and water content and some common aspects. In the barley case the impact of rain on soil moisture can be observed in the whole campaign, whereas in the case of corn with the development of the crop the impact of soil moisture on backscattering is soon lost but partially recovered and the end of the life cycle when the plants dry. Both crops have shown a relevant diurnal cycle that in the detailed study is attributed to dew water condensation/absorption/evaporation on crops and soil. In general, condensed water increases the backscattering coefficient with some differences depending on crop and polarisation, but opposite effects have been also found in a dry stage of corn which can be explained assuming a large extinction to scattering ratio.

The HH-VV correlation has been obtained for both barley and corn, showing an important co-polar decorrelation originated in the initial growth crop stages. Significant decorrelation is also caused by rain events in the case of barley which is not observed in the corn case after the plants begin to grow.

The impact of the diurnal plant water content cycle on radar backscattering has been studied for both crops in their late growth stage. In the barley case, the measured co-polar radar backscattering did not show significant correlation with sampled Plants Water Content (PWC). In the case of corn, there is a significant backscattering change between 6H and 8H (UTC), slightly advanced with respect to a PWC increase of the lower segment of the plant. However, the radar change might have been caused by air humidity changes.

The humidity changes in the atmosphere can introduce phase artefacts, up to one radian even at the HydroSoil short range of operation. The evaluation of atmospheric compensation on radar reflectors has shown very good results, confirming the interest of obtaining the atmospheric compensated Level 1c product.

The study of interferometric coherence evolution at different time scales has shown very interesting results, since strong correlations between the coherence decay and plant height / density have been found. For this reason, HydroSoil results could be used to optimise future mission configurations and better usage and interpretation of present missions' data in agriculture applications. Both

coherence decay rate and absolute level values can be exploited, considering the impact of external factors such as wind and rain (even extremely light) events. A general correlation matrix of coherence has been studied where the diagonals show the coherence time evolution for different time intervals of interest from short term GEOSAR imaging to LEOSAR (Sentinel-1).

The exploitation of the interferometric phase of the field has shown a very good correlation with atmospheric parameters but no significant correlation has been found with the crop growth, even when selecting high growth stages of both barley and corn in very stable atmospheric conditions. To obtain low noise phase averages the phase of the complex coherence has been evaluated in the whole mid-range area. As opposed to subsidence phenomena, a growing crop modifies significantly the geometry of the upper layer resulting in strong decorrelation of the process of interest. A strong correlation with crop phase evolution and atmospheric humidity and possibly also temperature changes has been shown, atmospheric refraction compensation reduced very slightly this correlation, indicating possible surface or volumetric changes in the scattering mechanisms induced by atmospheric parameters alterations.

Using HydroSoil data, virtual slow data acquisitions of a Hydroterra Geosynchronous SAR (GEOSAR) mission can be carried out. A Synthetic Aperture Radar acquisition of 4 hours data has been performed as an example, by taking small consecutive sub-apertures of multiple acquisitions along the 4 hours virtual data take. Once the sub-apertures have been combined to obtain the GEOSAR raw-data, the SLC images have been processed without relevant changes with respect to a conventional fast data-take. This result confirms the feasibility of obtaining GEOSAR images with moderate winds, the analysis can be extended to higher wind conditions.

In addition, some interesting evidences of man-made activity detection have been included, showing a precise location of the detected field activity (barley sowing) which produced a strong drop of coherence.

A first set of Doppler spectral densities has been computed from HydroSoil measurements, for several wind speeds. This data is relevant for clutter spectrum modelling and the study of clutter impact on SAR image focusing quality in long aperture missions.

Many lessons have been learned in the barley and corn HydroSoil campaigns, affecting different aspects such as the design of higher and stable RCS radar reflectors intended for calibration, the importance of designing an intrinsically stable radar using a thermostatic internal temperature control, complementing conventional soil moisture sensors with surface moisture sensors which is what radars can really sense at C-Band, synchronisation between wind anemometer and radar measurements, and other aspects that could be improved in future campaigns.